

# **Design of Tunable Beamforming Networks Using Metallic Ridge Gap Waveguide Technology**

**Mohamed Ahmed Nasr Mohamed Saif**

A Thesis  
in the Department  
of  
Electrical and Computer Engineering

Presented in Partial Fulfillment of the Requirements  
For the Degree of  
Doctor of Philosophy (Electrical and Computer Engineering) at  
Concordia University  
Montreal, Quebec, Canada

September 2019

© Mohamed Ahmed Nasr Mohamed Saif, 2019

**CONCORDIA UNIVERSITY**  
**SCHOOL OF GRADUATE STUDIES**

This is to certify that the thesis prepared

By: Mohamed Ahmed Nasr Mohamed Saif

Entitled: Design of Tunable Beamforming Networks using Metallic Ridge Gap Waveguide Technology

and submitted in partial fulfillment of the requirements for the degree of

Doctor Of Philosophy (Electrical and Computer Engineering)

complies with the regulations of the University and meets the accepted standards with respect to originality and quality.

Signed by the final examining committee:

\_\_\_\_\_ Chair  
Dr. Nematollaah Shiri

\_\_\_\_\_ External Examiner  
Dr. Raafat Mansour

\_\_\_\_\_ External to Program  
Dr. Amr Youssef

\_\_\_\_\_ Examiner  
Dr. Robert Paknys

\_\_\_\_\_ Examiner  
Dr. Abdel R. Sebak

\_\_\_\_\_ Thesis Supervisor  
Dr. Ahmed A. Kishk

Approved by \_\_\_\_\_  
Dr. Rastko Selmic, Graduate Program Director

November 11, 2019

\_\_\_\_\_  
Dr. Amir Asif, Dean  
Gina Cody School of Engineering & Computer Science

# Abstract

## **Design of Tunable Beamforming Networks using Metallic Ridge Gap Waveguide Technology**

**Mohamed Ahmed Nasr Mohamed Saif, Ph.D.**

**Concordia University, 2019**

Wireless communication is a leap of development in the history of humanity. For the past 100 years, a considerable effort has been spent to develop better standards, and technologies for a higher speed wireless communication with high system capacity for different applications. This requires the design of a high-frequency, point-to-multipoint antenna array system to achieve the mentioned goals. In addition, the reconfigurability of this antenna system is essential to change the system characteristics to achieve acceptable performance in different situations.

The main goal of this thesis is to design a reconfigurable beamforming network to work on the Ka-band for waveguide applications. Among different beamforming networks in the literature, the Butler matrix is chosen due to its higher efficiency and the smaller number of components required than other beamforming networks. The Butler matrix is designed using a dual-plane topology to avoid using crossovers. Ridge gap waveguide technology is chosen among different transmission lines to implement the Butler matrix for several reasons: It does not need dielectrics to operate, so its power handling capacity is defined by the gap height, and it has no dielectric losses. Its zero-field region represents the operating principle for some tunable devices introduced here and its contactless nature, which eases the assembly of waveguide parts at the millimeter-wave frequencies. The reconfigurability of the Butler matrix is implemented such that beamwidth, maximum gain, and beam direction may be all tuned for optimum system performance.

To that end, several components are designed to achieve the required target, and strict requirements are placed on several components to achieve an acceptable cascaded-system performance. These components include a ridge gap waveguide  $90^\circ$ -hybrid working over a more than 30% bandwidth, which can provide several coupling levels ranging from 3 dB to 33 dB and a return loss and isolation better than 30 dB. Another component is a wideband reconfigurable power splitter that

has a 40% bandwidth, a return loss better than 20 dB in the worst case and the ability to achieve all power splitting ratios including switching between the two guides. In addition, a wideband reconfigurable phase shifter is designed to have 33% bandwidth and phase shift tuning range from  $0^\circ$  to  $200^\circ$ . Two coaxial-to-ridge gap waveguide transitions are designed to work over a more than 100% bandwidth to facilitate testing different ridge gap waveguide components. Analysis of the asymmetric double ridge waveguide is introduced where its impedance is deduced and may be used to design a single to double ridge waveguide transition useful for the dual-plane Butler matrix introduced here. In addition, this concept is used to develop a wideband unequal power divider in the single ridge waveguide technology.

At the end, the whole system is assembled to show its performance in different tuning states. The ability of the system to produce radiation patterns of different characteristics is demonstrated. The presented Butler matrix design is a promising beamforming network for several applications like radar, base stations for mobile communications, and satellite applications.

# Acknowledgement

First and foremost, I offer my thanks and praise to God, the almighty, whose blessings and generosity made this work possible. I would also like to thank everyone who helped me during this journey.

I would like to express my gratitude to my supervisor, Dr. Ahmed A. Kishk, for his support and guidance during the course towards my Ph.D. at Concordia University.

Thanks are also due to the committee members: Dr. Abdel Razik Sebak, Dr. Robert Paknys and Dr. Amr Youssef for their time and the comments they provided during the course towards Ph.D., for serving in my examining committee and for helping to get the thesis in this shape. I would also like to thank the external examiner, Dr. Rafaat Mansour, for serving in the examining committee and for his useful comments.

I would also like to thank my friends and colleagues in the Department of Electrical and Computer Engineering for the good time we spent together, and for the useful discussions in research and life. I would like to thank my friends in Montreal for all the solidarity and support I received since I arrived.

Last, but not least, I would like to offer my love and appreciation to my family in Egypt and in Canada who prayed for me and who endured a lot. I would not have reached this far without their support, patience, and unconditional love.

*To my family*

# Contents

<b>List of Figures</b>	ix
<b>List of Tables</b>	xv
<b>List of Abbreviations</b>	xvii
<b>List of Symbols</b>	xviii
<b>Chapter 1: Introduction</b>	1
1.1 Motivation	1
1.2 Beamforming Networks	2
1.2.1 Comparison between different implementations	3
1.2.2 Analog beamformers	4
1.3 Fabrication Technology	7
1.3.1 Power capacity of transmission lines	7
1.3.2 Conventional waveguide	8
1.3.3 Ridge waveguide	9
1.3.4 Ridge gap waveguide technology	10
1.4 Objectives	11
1.5 Thesis Contributions and Organization	13
<b>Chapter 2: Literature Survey</b>	15
2.1 Butler Matrix	15
2.1.1 Printed circuit technologies	15
2.1.2 Metallic waveguide technologies	17
2.2 Waveguide Adapters	18
2.3 Power Splitters and Switches	20
2.4 Couplers	23
2.5 Reconfigurable Phase Shifters	25
<b>Chapter 3: Wideband Transitions for the Ridge Gap Waveguide</b>	27
3.1 Introduction	27
3.2 Wideband Inline Transition	27
3.2.1 Ridge gap waveguide design	27
3.2.2 Inline transition to the ridge gap waveguide	28
3.3 Wideband Vertical Transition	35
3.3.1 Ridge gap waveguide design	36
3.3.2 Vertical transition to the ridge gap waveguide	36
<b>Chapter 4: Wideband Single Ridge and RGW Power Splitters</b>	43
4.1 Introduction	43
4.2 Analysis of Asymmetric Double Ridge Waveguide	43
4.3 Wideband Ridge Waveguide Splitter	46
4.3.1 Design of unequal power splitter	46

4.3.2 Results	48
4.4 Wideband Reconfigurable Ridge Gap Waveguide Splitter	53
4.4.1 Design of the reconfigurable power divider	53
4.4.2 Parametric studies and results	55
<b>Chapter 5: Arbitrary-coupling RGW Quadrature Hybrid</b>	66
5.1 Introduction	66
5.2 Coupler Geometry and Theory of Operation	66
5.3 Results and Parametric Studies	72
<b>Chapter 6: Low-Error Reconfigurable Phase Shifter Using RGW</b>	76
6.1 Introduction	76
6.2 Analysis of Reflection-type Phase Shifter	76
6.3 Phase Shifter Design and Parametric Studies	78
<b>Chapter 7: Butler Matrix Assembly and Results</b>	85
7.1 Analysis of Proposed Butler Matrix	85
7.2 Basic Butler Matrix	86
7.3 Reconfigurable Part	88
7.4 Capabilities of the Tunable Butler Matrix	100
<b>Chapter 8: Summary and Future Research Directions</b>	106
8.1 Summary of Contributions	106
8.2 Future Work	107
<b>Appendix</b>	109
<b>References</b>	112

# List of Figures

<b>Figure 1.1</b>	General 4x4 beamforming network consists of 4 dividers, 4 combiners, and 12 phase shifters (from [8]).	5
<b>Figure 1.2</b>	Conventional 4x4 Butler matrix consists of 4 quadrature hybrid couplers and 2 phase shifters with 45° phase shift.	5
<b>Figure 1.3</b>	3-beam Blass matrix consists of 12 couplers, and delay-line phase shifters. Angle $\alpha_1$ controls first beam directions (from [8]).	6
<b>Figure 1.4</b>	5x8 Rotman lens depends on geometrical optics to achieve power splitting, combination, and phase shift (from [8]).	6
<b>Figure 1.5</b>	Rise of the temperature of several substrates versus frequency (from [9]).	8
<b>Figure 1.6</b>	Structure of the RGW: (a) Top and front view. (b) Stop-Go Characteristics of RGW allow propagation along the ridge and prevents it above the pins.	12
<b>Figure 3.1</b>	(a) 2D-dispersion diagram of a unit cell of <i>RGW A</i> using CST. (b) 1D-dispersion diagram of a single row of <i>RGW A</i> using CST.	29
<b>Figure 3.2</b>	(a) 2D-dispersion diagram of a unit cell of <i>RGW B</i> using CST. (b) 1D-dispersion diagram of a single row of <i>RGW B</i> using CST.	29
<b>Figure 3.3</b>	(a) Wave port used in [52]. (b) Wave port used in [13]. (c) Comparison of S-parameters for 2 ports while feeding <i>RGW B</i> obtained using ANSYS.	30
<b>Figure 3.4</b>	Transition geometry with all parameters: Top view, side section BB', front section CC', and an exploded isometric view. In the isometric view, the grey arrows indicate the transition parts movement directions.	31
<b>Figure 3.5</b>	(a) Single-sided S-parameters of the transition using ANSYS. (b) Comparison of S-parameters for back-to-back configuration of part 1 of the transition by measurement, and simulations.	32
<b>Figure 3.6</b>	Geometry of the fitting part with all parameters: (a) Side view. (b) Front section DD' matching transition dimensions. (c) Back section EE' that matches dimensions of <i>RGW A</i> .	33
<b>Figure 3.7</b>	Fitting part S-parameters (PEC) as obtained from ANSYS.	33

<b>Figure 3.8</b>	Photo of the manufactured components for the inline transition	34
<b>Figure 3.9</b>	(a) Comparison of S-parameters (measured VS simulated (ANSYS)) for transition feeding <i>RGW A</i> . (b) Comparison of the measured and simulated S-parameters for transition feeding <i>RGW B</i> .	34
<b>Figure 3.10</b>	Geometry of the first part of the transition showing the front section FF' and the side section GG' with two screws in the front section.	35
<b>Figure 3.11</b>	Parametric study on the effect of the height of the screws on S-parameters of the transition.	35
<b>Figure 3.12</b>	<i>RGW B</i> structure with 5-section Chebyshev matching transformer. (a) Top view. (b) Front cut at Section BB'.	36
<b>Figure 3.13</b>	The dispersion diagrams obtained from eigenmode analyses using CST Microwave studio. (a) 2D-dispersion diagram of a unit cell. (b) 1D-dispersion diagram of one row.	38
<b>Figure 3.14</b>	Transition structure after removing the cover plate. (a) Isometric. (b) Top view with inset. (c) Front cut AA' through the connector.	39
<b>Figure 3.15</b>	S-parameters of the vertical transition. (a) Single-sided S-parameters. (b) Comparison of the simulated double-sided S-parameters (ANSYS) of the transition with the measurement.	40
<b>Figure 3.16</b>	ADR transition design with the parameters shown. (a) Isometric view of the top part. (b) Top view of the top part. (c) ADR transition upside down.	40
<b>Figure 3.17</b>	Comparison of the measured and simulated (ANSYS) S-parameters for back-to-back configuration of the asymmetric double ridge transition.	41
<b>Figure 3.18</b>	A photo of the manufactured components.	42
<b>Figure 3.19</b>	Comparison of the measured and simulated (ANSYS) S-parameters for the single ridge transition feeding <i>RGW B</i> in back-to-back configuration.	42
<b>Figure 4.1</b>	Illustration of the reasoning behind the existence of zero tangential electric field plane (thick dashes) in ridge waveguide. (a) Double ridge waveguide. (b) Single ridge waveguide. (c) Asymmetric double ridge waveguide.	44
<b>Figure 4.2</b>	Comparison between the approximate and exact solutions obtained for the position of the zero- $E_t$ plane as represented by $b_A$ for different upper and lower ridges' heights. (a) $r_B = 1$ mm. (b) $r_B = 2$ mm. (c) $r_B = 3$ mm.	46
<b>Figure 4.3</b>	Splitter structure using double/single ridge waveguides. (a) Side view of the splitter with 3 ports $P1$ , $P2$ and $P3$ and inset showing steps $k_A$ and $k_B$ . (b) Front view at Section AA'.	47

<b>Figure 4.4</b>	Final design of the 6-dB splitter. (a) Top view of upper half with transformer stages numbered. (b) Front section BB'. (c) Front section CC'.	<b>49</b>
<b>Figure 4.5</b>	A photo of the manufactured splitters.	<b>50</b>
<b>Figure 4.6</b>	(a) Simulated and measured S-parameters of the 3-dB power splitter. (b) Simulated and measured S-parameters of the 6-dB power splitter. (c) Simulated and measured S-parameters of the 10-dB power splitter.	<b>51</b>
<b>Figure 4.7</b>	Parametric study on the effect of sheet thickness on the S-parameters of the wideband splitter using CST.	<b>53</b>
<b>Figure 4.8</b>	Geometry of the reconfigurable power splitter with all design parameters shown. (a) Isometric view. (b) Section AA'. (c) Section BB'.	<b>56</b>
<b>Figure 4.9</b>	1D-eigenmode analysis and its results for DRGW and RGW waveguides. (a) Eigenmode analysis setup in CST. (b) 1D-dispersion diagram of DRGW. (c) 1D-dispersion diagram of RGW.	<b>58</b>
<b>Figure 4.10</b>	S-parameters for the splitter in different states of 3, 6 and 60 dB splitting. (a) Magnitude of $S_{11}$ and $S_{31}$ in dB. (b) Phase difference between output arms.	<b>60</b>
<b>Figure 4.11</b>	Parametric study on the effect of varying $h_{ss}$ and $a_{ss}$ on the upper (dashed) and lower (solid) frequency limits of the DRGW side of the reconfigurable splitter.	<b>61</b>
<b>Figure 4.12</b>	Parametric study on the effect of the maximum sheet deflection on the upper (dashed) and lower (solid) frequency limits of the reconfigurable splitter for several values of $h_{ss}$ and $a_{ss}$ .	<b>61</b>
<b>Figure 4.13</b>	Parametric study on the upper (dashed) and lower (solid) frequency limits of the reconfigurable splitter for several values of $h_{ss}$ and $a_{ss}$ ( $h_{ss}=1$ mm shows zero bandwidth).	<b>62</b>
<b>Figure 4.14</b>	Maximum power handling capability of the splitter and the corresponding bandwidth for different ridge heights ( $h_r = h_{ss}$ ).	<b>63</b>
<b>Figure 4.15</b>	Parametric study on power division ratio and phase difference provided by different sheet deflections.	<b>63</b>
<b>Figure 4.16</b>	Photo of the measurement setup of the reconfigurable splitter with 3-dB power split ratio shown.	<b>64</b>

<b>Figure 4.17</b>	Comparison of the measured (red) and simulated (black) S-parameters for different cases of the reconfigurable splitter. (a) 3-dB case. (b) 8-dB splitter.	<b>65</b>
<b>Figure 5.1</b>	Directional coupler structure with all the parameters shown. (a) Isometric view. (b) Top view of one RGW and one sheet used to design the coupler. (c) Top view of the RGW with the matching transformers needed for interfacing (ANSYS).	<b>68</b>
<b>Figure 5.2</b>	Characteristic impedances and the propagation constants of the 3 guides required in the eigenmode analysis: (a) Characteristic impedance. (b) Propagation constant.	<b>69</b>
<b>Figure 5.3</b>	Comparison of coupling computed using (5.2) to full-wave analysis for 1-slot waveguide (15 dB coupler) and 2-slot waveguide (10 dB coupler)	<b>70</b>
<b>Figure 5.4</b>	(a) Characteristic impedance of the even (solid) and odd (dashed) modes of the 1 slot coupler for several ridge heights. (b) Comparison of the coupling level obtained using (5.2) and the full-wave results.	<b>71</b>
<b>Figure 5.5</b>	Simulated (black) and measured (red) S-parameters of the proposed coupler with different coupling levels fed by the vertical transition. (a) 3 dB. (b) 6 dB. (c) 10 dB (d) 15 dB. Results are obtained using ANSYS.	<b>73</b>
<b>Figure 5.6</b>	(a) Photo of the measurement setup of the 6 dB coupler. (b) Photo of the manufactured structure.	<b>74</b>
<b>Figure 5.7</b>	Effect of the sheet thickness on the coupler bandwidth obtained using ANSYS.	<b>75</b>
<b>Figure 5.8</b>	Effect of ridge height on the coupling level of the coupler obtained using ANSYS.	<b>75</b>
<b>Figure 6.1</b>	Schematic of the reflection type phase shifter.	<b>77</b>
<b>Figure 6.2</b>	Contour plot showing values of the reflection coefficient of the phase shifter of different phase and balance errors of the 90° hybrid.	<b>79</b>
<b>Figure 6.3</b>	Design geometry for the reconfigurable phase shifter. (a) Isometric view for one half of the phase shifter (b) Side cut of half the coupler (left), side cut of the coupler (middle) and front view of the coupler with dimensions. (c) Top view of the phase shifter.	<b>80</b>
<b>Figure 6.4</b>	S-parameters for the 4-port coupler without screws or short circuits.	<b>81</b>

<b>Figure 6.5</b>	Circuit model of a variable height screw inside a rectangular waveguide, according to [136].	<b>81</b>
<b>Figure 6.6</b>	(a) Simulation setup to show the effect of adding a fixed height cylinder on the flat phase variation due to variable height screw. (b) Simulation of the phase difference between the transmitted signal for different heights of the screw and the transmitted signal for zero-height screw for two cases: with fixed height cylinder (solid) and without fixed height cylinder (dashed).	<b>82</b>
<b>Figure 6.7</b>	Single-sided S-parameters of the RGW to rectangular waveguide transition generated using ANSYS.	<b>83</b>
<b>Figure 6.8</b>	Parametric study on the variation of the phase shift with different screw depths.	<b>83</b>
<b>Figure 6.9</b>	Simulated S-parameters of the reconfigurable phase shifter obtained using ANSYS (line) and verified using CST (dotted) (a) Magnitude in dB (b) Phase in degrees.	<b>84</b>
<b>Figure 7.1</b>	Topology of the reconfigurable Butler matrix	<b>85</b>
<b>Figure 7.2</b>	3D exploded view of the basic Butler matrix with the details of the bottom layer and the middle sheet shown.	<b>87</b>
<b>Figure 7.3</b>	S-parameters of the coupler.	<b>88</b>
<b>Figure 7.4</b>	Design of the 135° phase shifter working on the Ka-band showing different design parameters. (a) Phase shifter structure with transparent sheet and ridges of the upper half (upper pins and plate removed) (b) Closer look at the phase shifter dimensions.	<b>89</b>
<b>Figure 7.5</b>	S-parameters of the 135° phase shifter.	<b>90</b>
<b>Figure 7.6</b>	S-parameters of the basic Butler matrix (ANSYS line, CST dash-dot)	<b>91</b>
<b>Figure 7.7</b>	Design of the reconfigurable part of Butler matrix. (a) 3D exploded view showing bottom layer details looking from top with middle sheet exposed. (b) 3D exploded view showing top layer details looking from bottom.	<b>93</b>
<b>Figure 7.8</b>	Return loss at 1 input port of the reconfigurable part in 2 different cases.	<b>94</b>

<b>Figure 7.9</b>	Transmission coefficients in dB at different output ports for the two cases.	<b>95</b>
<b>Figure 7.10</b>	Transmission coefficients in degrees at different output ports for the two cases (a) equal power splitting at all ports (b) unequal splitting at 2 ports.	<b>96</b>
<b>Figure 7.11</b>	ADS schematic to show the assembly of full Butler matrix as building blocks.	<b>97</b>
<b>Figure 7.12</b>	S-parameters of the Butler matrix in the case of pattern 1 configuration (a) Return loss (b) Transmission S-parameters in dB.	<b>98</b>
<b>Figure 7.13</b>	S-parameters of the Butler matrix in the case of pattern 3 configuration. (a) Return loss (b) Transmission S-parameters in dB.	<b>99</b>
<b>Figure 7.14</b>	Schematic of the relative phase shift and power distribution for the 1×8 antenna array fed by Butler matrix.	<b>100</b>
<b>Figure 7.15</b>	Different array factors produced by different power ratios and phase shifts of the reconfigurable part feeding isotropic antennas (a) 0.4 λ element spacing (b) 0.5 λ element spacing (c) 0.6 λ element spacing.	<b>103</b>
<b>Figure 7.16</b>	Array factor of Butler matrix with equal power splitting and 25° progressive phase shift with different antenna spacing (maximum directivity 18 dB) (a) 0.4 λ element spacing (b) 0.5 λ element spacing (c) 0.6 λ element spacing.	<b>104</b>
<b>Figure 7.17</b>	Array factor of Butler matrix pattern 3 of Table 7.4 with different antenna spacing (maximum directivity 16.5 dB) (a) 0.4 λ element spacing (b) 0.5 λ element spacing (c) 0.6 λ element spacing.	<b>104</b>
<b>Figure 7.18</b>	Array factor of Butler matrix obtained using pattern 4 of Table 7.4 with different antenna spacing (maximum directivity 15 dB) (a) 0.4 λ element spacing (b) 0.5 λ element spacing (c) 0.6 λ element spacing.	<b>105</b>
<b>Figure 7.19</b>	Array factor of Butler matrix obtained using pattern 5 from Table 7.4 with different antenna spacing (maximum directivity 10 dB) (a) 0.4 λ element spacing (b) 0.5 λ element spacing (c) 0.6 λ element spacing.	<b>105</b>
<b>Figure A.1</b>	Asymmetric double ridge waveguide with all parameters shown.	<b>110</b>
<b>Figure A.2</b>	S-parameters for the 5-stage Chebyshev transformer designed using ADR waveguides based on the suggested formula. S-parameters are obtained using CST Microwave Studio.	<b>111</b>

# List of Tables

<b>Table 3.1</b>	Comparison between reported RGW transitions in the literature.	<b>28</b>
<b>Table 3.2</b>	Values of different parameters for the two RGWs according to Fig. 1.6 notation.	<b>29</b>
<b>Table 3.3</b>	Values of different parameters for the transition according to Fig. 3.4 notation.	<b>31</b>
<b>Table 3.4</b>	Values of different parameters for the fitting part according to Fig. 3.6 notation (next).	<b>32</b>
<b>Table 3.5</b>	Values of the parameters of Chebyshev transformers in Fig. 3.12.	<b>36</b>
<b>Table 4.1</b>	Values of different parameters for 3 different cases of the splitter, as shown in Fig. 4.3 (Sheet thickness=0.5 mm).	<b>48</b>
<b>Table 4.2</b>	Values of different parameters of 6-dB splitter following Fig. 4.4 notation (all in mm).	<b>50</b>
<b>Table 4.3</b>	Values of different parameters of 10-dB splitter following Fig. 4.4 notation (all in mm).	<b>50</b>
<b>Table 4.4</b>	Parametric study on the effect of increased gap height on the bandwidth of the wideband splitter.	<b>52</b>
<b>Table 4.5</b>	Values of different parameters of the reconfigurable power splitter following Fig. 4.8 notation.	<b>57</b>
<b>Table 4.6</b>	Comparison between different variable splitters in the literature.	<b>64</b>
<b>Table 5.1</b>	Values of the parameters of different couplers in Fig. 5.5 (next), following Fig. 5.1 notation.	<b>72</b>
<b>Table 5.2</b>	Comparison between different RGW couplers in the literature.	<b>74</b>
<b>Table 6.1</b>	Values of different components in Fig. 6.5 at different screw heights as in [136].	<b>81</b>
<b>Table 6.2</b>	Values of different parameters of reconfigurable phase shifter, according to Fig. 6.3 notation.	<b>83</b>
<b>Table 7.1</b>	Phases obtained at different nodes for single input excitation of the Butler matrix in Fig. 7.1.	<b>86</b>

<b>Table 7.2</b>	Parameters of the coupler working in the Ka-band (28 GHz to 38 GHz) (following Fig. 5.1 notation for slots and Fig. 1.6 notation for RGW).	<b>87</b>
<b>Table 7.3</b>	Parameters of the phase shifter in Fig. 7.4.	<b>90</b>
<b>Table 7.4</b>	Different splitting ratios and phase shifts at different antenna ports.	<b>101</b>
<b>Table 7.5</b>	Screw depths (in mm) needed to achieve sheet deflection and phase shift for values in Table 7.4.	<b>102</b>
<b>Table A.1</b>	Dimensions, and impedances for different cross-sections of the ADR 5 <sup>th</sup> order Chebyshev matching transformer.	<b>111</b>

# List of Abbreviations

<b>1D</b>	One-Dimensional
<b>2D</b>	Two-Dimensional
<b>4G</b>	Fourth generation technology
<b>5G</b>	Fifth generation technology
<b>ADC</b>	Analog to Digital Converter
<b>ADR</b>	Asymmetric Double Ridge
<b>AMC</b>	Artificial Magnetic Conductor
<b>APHC</b>	Average Power Handling Capability
<b>BW</b>	Bandwidth
<b>CPW</b>	Coplanar Waveguide
<b>DAC</b>	Digital to Analog Converter
<b>DOA</b>	Direction of Arrival
<b>DRGW</b>	Double Ridge Gap Waveguide
<b>GGW</b>	Groove Gap Waveguide
<b>IF</b>	Intermediate Frequency
<b>MBA</b>	Multiple Beam Antennas
<b>OMT</b>	Orthomode Transducer
<b>PCB</b>	Printed Circuit Board
<b>PPHC</b>	Peak Power Handling Capability
<b>RGW</b>	Ridge Gap Waveguide
<b>RF</b>	Radio Frequency
<b>SIW</b>	Substrate Integrated Waveguide
<b>SLL</b>	Sidelobe level
<b>SNR</b>	Signal to Noise Ratio
<b>TE</b>	Transverse-Electric
<b>TEM</b>	Transverse-Electromagnetic
<b>TM</b>	Transverse-Magnetic
<b>TTD</b>	True Time Delay
<b>UWB</b>	Ultra-wideband.
<b>WG</b>	Waveguide

# List of Symbols

$\Omega$	Ohm
<b>GHz</b>	Giga-Hertz ( $10^9$ Hertz)
$B$	Propagation constant
$A$	Wavelength
$\lambda_o$	Free space wavelength
$\lambda_c$	Cut-off Wavelength
$\lambda_g$	Guided Wavelength
$\epsilon_r$	Relative Permittivity
<b>dB</b>	Decibel
$\eta_o$	Free space impedance
$E$	Young's Modulus
<b>KN</b>	Kilo Newton

# Chapter 1

## Introduction

### 1.1 Motivation

The demands on wireless communications are currently higher than ever due to the increased use of wireless communications in our daily lives, which caused the emergence of new technologies that require higher capacity communications. High capacity communications require seeking the underutilized spectrum in the millimeter-wave band, which is a good candidate since it can carry hundreds of times more capacity than the currently utilized frequency bands. Some of the challenges in the millimeter wave spectrum are the inherent losses due to the path loss and the atmospheric attenuation [1]. These losses suggest utilizing antenna arrays to achieve high gain with wideband feeding network. Beamforming networks may be used as a feeding network, which communicates with several destinations using the same antenna array. Several applications that emerged in the market nowadays require high-speed wireless communications like 5G technologies [2] and satellite-based internet [3]. In the satellite-based internet, hundreds of satellites fly above the earth to connect people together using earth ground stations, and it is most useful in remote areas, where significant gaps in basic infrastructure make satellite services the most efficient means to connect. In order to maintain high-speed communications, the satellites should operate at millimeter-wave frequencies, and beyond, where antenna arrays driven by a beamforming network are a must to combat high propagation loss and to increase system capacity.

The most valuable advantage of wireless communications is user mobility, where the transmitter/receiver relative position is not a barrier to connectivity, which makes the environment dynamic. In such a dynamic environment, a reconfigurable beamforming network represents a convenient and efficient choice for several reasons:

- 1- In mobile communications, changing beamwidth (crossover level) may be used for the trade-off between the capacity, and the coverage distance of the mobile base station in different times of the day (covering a large number of users in the vicinity of the base station in rush hours, and covering a further localized user at other times of the day). In addition, using

tunable beamforming networks can allow capacity control by changing the number of orthogonal beams covering certain sectors of a mobile base station.

- 2- In mobile communications, changing each beam's direction and/or beamwidth is useful for allowing fewer power fluctuations (soft handover) during user motion between beams or reducing interference for users covered by two different beams. In addition, a widened spatial coverage may be sought using the reconfigurable beam direction.
- 3- In satellite communications, the tunable performance may be used to ensure the coverage of a constant spot on earth regardless of the satellite height above the earth at different positions in its orbit. The same applies to the field of airborne remote sensing.
- 4- In radar applications, the "zooming" capability provided by each beam allows more accurate positioning of aerial vehicles leading to higher efficiency.

Several other applications exist in real life for tunable beamforming network, which makes it attractive for implementation. The next two sections provide a background on beamforming networks and fabrication technologies.

## **1.2 Beamforming Networks**

Beamforming networks are used to provide the necessary amplitudes and phases for an antenna array to communicate with different destinations at the same time, which is needed for several applications like satellite and radar applications [4]. It is also used in radars to search for targets in different directions [5]. Some beamforming networks can achieve same-frequency multiple-beam steering simultaneously (feed Multiple Beam Antennas (MBA)), and others are single beam depending on the type of communication (point to point/multipoint). Beamformers may also be classified into static (switched beams), and dynamic (adaptive beams) types, where static beamformers provide fixed phases, and amplitudes at the antenna during transmission, and reception, while dynamic beamformers can change phases and amplitudes of received or transmitted antenna to change the amplitude, and phase at each element [6] to allow objects/users tracking.

### **1.2.1 Comparison between different implementations**

Beamforming may also be classified according to the technology of implementation into several categories, three of which are famous: Analog beamforming, digital beamforming, and optical beamforming. In analog beamforming, the beamforming is done either using matrices (where a combination of power splitters, combiners, and phase shifters is employed) or using lenses without going to the digital domain. In digital beamforming, the received signal from RF frontend is traditionally down-converted to IF or baseband frequency to be fed to an Analog to Digital Converter (ADC) such that the signal is discretized before being fed to a Digital Signal Processing (DSP) chip. The digital processor is capable of extracting different signals to different ports. During transmission, the baseband signal is fed into the digital processor to produce the required magnitude and phase, which is followed by a digital to analog converter (DAC), after which the signal is up-converted to the RF frequency to be transmitted to the RF frontend. Optical beamforming uses optics to realize the phase shifting and coupling, which requires a signal to be modulated using an optical source before implementing the phase delay using some delay line. After that, the signal is demodulated (detected) using an optical detector before being transmitted to the RF front-end [7].

Each beamforming system has its advantages and limitations. For example, in digital beamforming networks, the beamforming is handled in the digital domain, so phase shifting and amplitude tapering are handled by an algorithm. In addition, more sophisticated algorithms might be possible in the digital domain like adaptive beamforming, and direction of arrival (DOA) estimation. The limitation in the digital beamforming is in the conversion from analog to digital or digital to analog. The number of ADCs or DACs depends whether beamforming is fully digital, fully analog or hybrid with fully digital requiring highest number; hence needs more power to operate and more space in the network. Another limitation is the number of ports of the digital processing chip, which needs to be greater than or equal to the number of antennas in order to have the whole antenna array vector received at the processor to be able to perform DOA estimation or adaptive beamforming, which is not suitable for large antenna arrays needed for high frequencies. The need for an RF frontend around each antenna element is also a challenge in the fully digital beamforming networks in case of high frequencies.

In optical beamforming networks, the main advantage is the ability to employ true time delays (TTD) for a wideband phase shift, which is hard to implement in microwave/RF frequencies. The TTD is able to delay the signal in time in order to achieve a wideband phase shift, which may be desirable for wideband beamforming networks. On the other hand, optical beamforming requires modulating an optical source (e.g., Laser) by the RF signal before optical beamforming, where TTD and optical couplers are used, then demodulation or detection for the RF signal. This process involves losses in the conversion processes, which reduces the efficiency of this beamforming type.

In light of the previous discussion, the analog beamforming network requires the least power to operate since less number of ADCs and DACs than digital beamforming are used, which also means less digitizing losses. Also, the area required by the full RF frontend with ADCs to be placed around each antenna might not be easy to find at high frequencies (around 30 GHz), where antennas are supposed to be placed very close to each other. In addition, the number of digital processor ports, storage, and computational speed would put a limit on the array size needed at high-frequency communication. On the other hand, analog beamformers are less adaptive than digital beamformers. All these factors encourage the study of analog beamforming networks as a good candidate for millimeter wave applications.

### **1.2.2 Analog beamformers**

The analog beamforming networks in literature are numerous, and they are different in several aspects like the number of components used, whether they are of lossy nature, and the relation between input and output ports. A general schematic of beamforming networks is shown in Fig. 1.1. Typically a large number of phase shifters, combiners, and splitters are associated with analog beamforming networks; however, some networks use different feed topologies and components to reduce the number of components. Figure 1.2 shows a 4x4 Butler matrix, which needs 6 components to operate in its standard form. In the conventional Butler matrix, the number of output ports is typically  $2^m$  where  $m$  is an integer, and it is equal to a number of input ports. Other famous types of analog BFN are Rotman lens, and Blass matrix [8], which are shown in Figs 1.3, and 1.4, respectively. Rotman lens operates based on the principle of geometrical optics, where phase shifting and power splitting/combing are handled by the lens cavity without any devices; however dummy ports with absorbing loads have to be added to reduce the reflection of the power

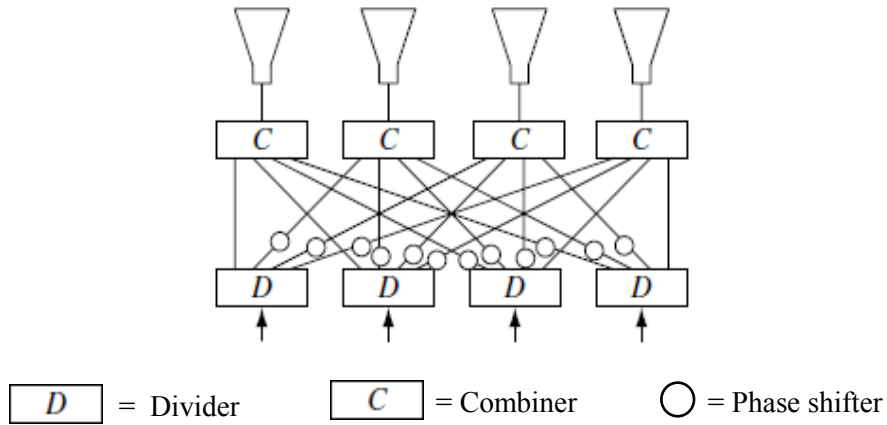


Fig. 1.1: General 4x4 beamforming network consists of 4 dividers, 4 combiners, and 12 phase shifters (from [8]).

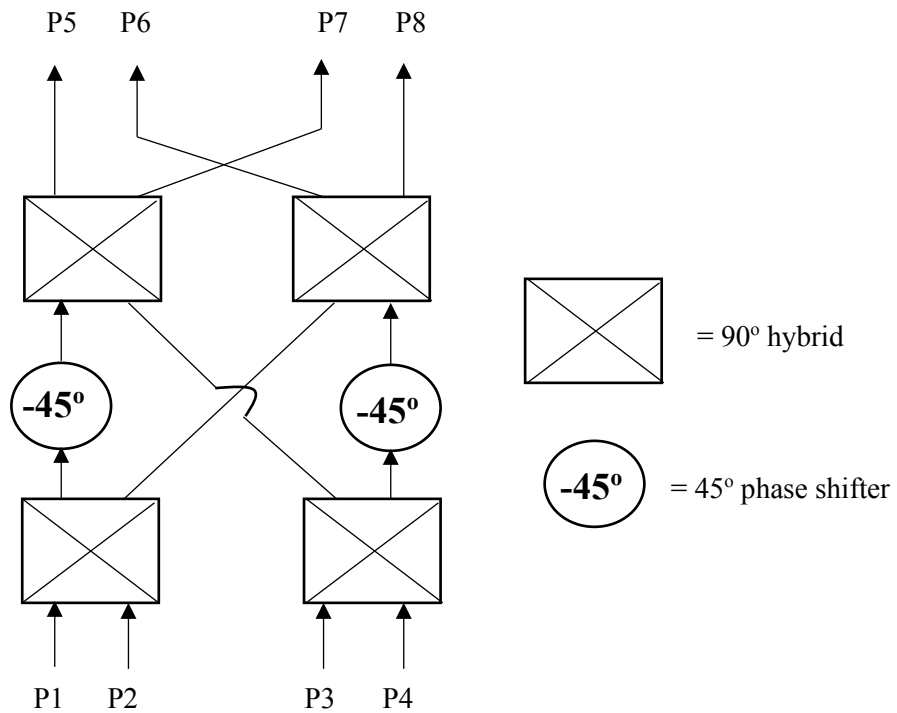


Fig. 1.2: Conventional 4x4 Butler matrix consists of 4 quadrature hybrid couplers and 2 phase shifters with 45° phase shift.

from the sides of the lens. In Blass matrix, coupler characteristics dictate some losses in the matched loads. In addition, the conventional Blass matrix requires a large number of couplers equal to the product of the number of input and output ports, and the same number of phase shifters, which is more than that needed by Butler matrix. The large number of components required in the Blass matrix is due to the fact of being a series-fed network, unlike Butler matrix.

The advantage of the conventional Blass and Nolen matrices over the conventional Butler matrix is in having no restriction on the number of input or output ports besides the ability to provide any amplitude distribution at the antennas. Also, crossovers are not needed in the Blass matrix, unlike the conventional Butler matrix. The next section presents a literature survey on different forms of the Butler matrix.

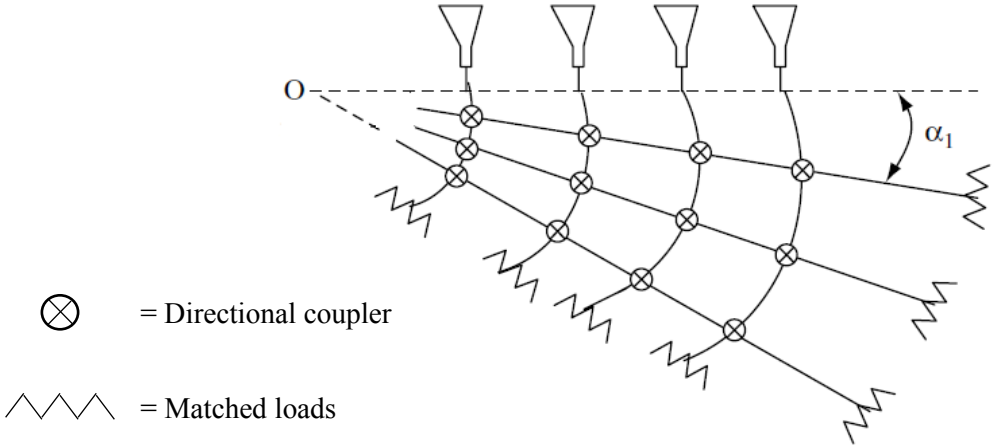


Fig. 1.3: 3-beam Blass matrix consists of 12 couplers, and delay-line phase shifters. Angle  $\alpha_1$  controls first beam directions (from [8]).

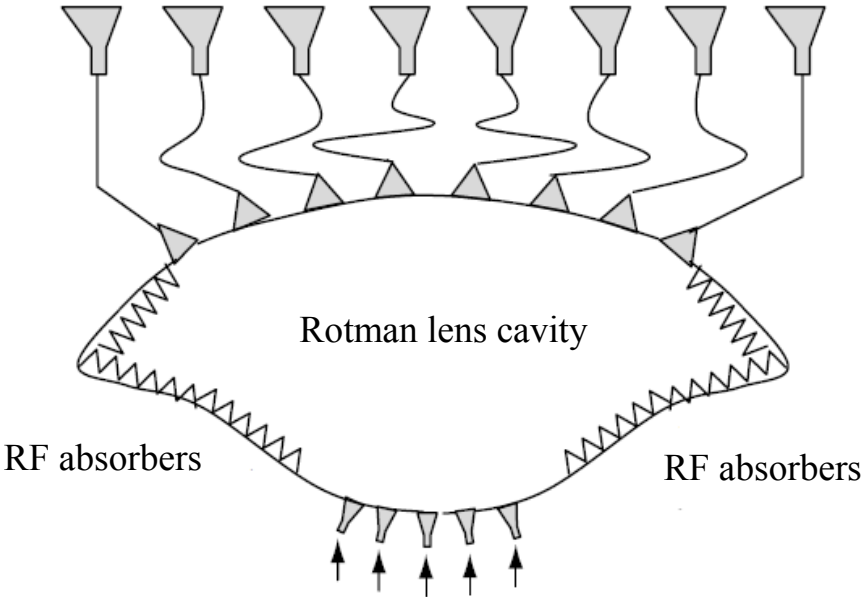


Fig. 1.4: 5x8 Rotman lens depends on geometrical optics to achieve power splitting, combination, and phase shift (from [8]).

## 1.3 Fabrication Technology

Waveguides have been used for decades as high-power transmission lines to design microwave systems for several applications, including military and satellite applications. On the other hand, printed circuit technology has been used for low profile applications, where high power requirement is not needed. Mechanical rigidity and high power handling capability of waveguides are the main advantages of waveguides over printed circuit technologies, which makes it suitable for harsh environments. An overview of the power handling capability of different transmission lines is introduced next.

### 1.3.1 Power capacity of transmission lines

The ability of a transmission line to carry high power is determined according to two factors:

- 1- **Peak power handling capability (PPHC)** which is determined by the breakdown voltage of the insulator inside the line. In the case of air, the breakdown electric field is known to be 3 KV/mm under normal pressure. Breakdown electric field for several dielectrics is found in [9] and is usually higher than that of air. The smallest distance between two conductors carrying different voltage,  $d$ , is what determines the maximum PPHC for a transmission line, which is computed as:

$$P_{PPHC} = \frac{V_{max}^2}{2 Z_o} = \frac{(E_{max} \cdot d)^2}{2 Z_o}$$

for a transmission line of characteristic impedance  $Z_o$ .

- 2- **Average Power Handling Capability (APHC)** which is determined by the ohmic losses and the resulting rise in temperature. For every insulator, there is a maximum temperature above which its electric and physical properties are altered; hence, the transmission line characteristics are not guaranteed. The APHC is usually lower for printed circuit technologies (like microstrip line, stripline and coplanar waveguide) than air-filled transmission lines. In [9], the rise in the temperature of several substrates is calculated and plotted versus frequency. The plot is shown in Fig. 1.5, where it is shown that the rise in temperature increases with the frequency, which means a lot of substrates are not suitable for high power operation at high frequencies. It is mentioned in [9] that the APHC is the main limitation on using dielectric substrates for high power applications since the APHC for most

of the substrates is limited to few Kilowatts at 10 GHz and inversely proportional with the frequency; hence, not a good candidate for high-frequency operation.

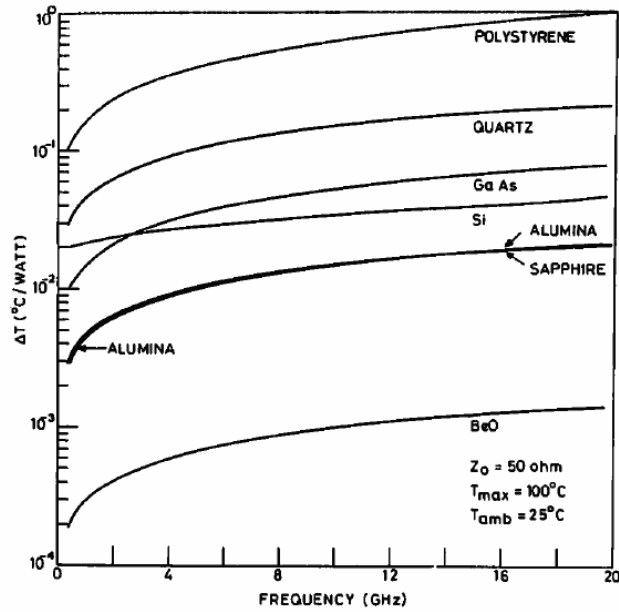


Fig. 1.5. Rise of the temperature of several substrates versus frequency (from [9]).

On the other hand, waveguides are considered transmission lines of high power capacity because they need no dielectric substrate to operate. An overview of the most common types of waveguides is presented next.

### 1.3.2 Conventional waveguide

The earliest type of transmission lines used to transmit signals, where a metallic pipe of the rectangular or circular cross-section is used to guide the power from one end of the guide to the other end [10]. The conventional waveguide supports Transverse-Electric (TE), and Transverse-Magnetic (TM) modes but not Transverse-Electromagnetic (TEM) mode. The waveguide only operates after a specific nonzero cutoff frequency, which is said to be the dominant mode cutoff frequency. The dominant mode represents the only mode that may exist alone in the waveguide; hence, the most usable one. The dominant mode of the standard rectangular waveguides is the  $\text{TE}_{10}$  mode, while that of standard circular waveguides is the  $\text{TE}_{11}$  mode.

The main factor that determines the power capacity of waveguides is the PPHC which is computed, for an air-filled rectangular waveguide of dimensions  $a \times b$ , as:

$$P_{PPHC} = \frac{(E_{max} \cdot b)^2}{2 Z_{PV}}$$

where  $b$  is the minimum dimension ( $b < a$ ) and  $E_{max}=3$  KV/mm.  $Z_{PV}$  is the impedance of a rectangular waveguide according to the power-voltage definition and it is computed as:

$$Z_{PV} = \frac{2b}{a} Z_w = \frac{2b}{a} \frac{k}{\beta} \eta_o$$

where  $\frac{k}{\beta}$  is the ratio of free space propagation constant to air-filled waveguide propagation constant. If it is assumed that PPHC is computed at a frequency much higher than dominant mode cutoff and that standard waveguides normally have  $a \approx 2b$ , then:

$$P_{PPHC} = \frac{(E_{max} \cdot b)^2}{2 \eta_o}$$

### 1.3.3 Ridge waveguide

Ridge waveguides have been used for decades in high power transmission due to its wider separation between dominant mode cutoff, and higher order mode cutoff, which means wider usable single-mode bandwidth [11]. It consists of a conventional rectangular or circular waveguide with one or more metal inserts. Other advantages of ridge waveguides are having a lower impedance than conventional waveguides, so it is easier to be matched to the coaxial line. The main drawback of the ridge waveguide is having a lower power handling capability than the conventional waveguides; this is because the height of the gap is the smallest dimension in the guide, and it is normally lower than the height of the rectangular waveguide for wideband operation. The PPHC, for the air-filled ridge waveguides, is computed as [11]:

$$P_{PPHC} = \frac{(E_{max} \cdot d)^2}{2 Z_{PV}}$$

$$Z_{PV} = \frac{\pi \eta_o d / \lambda_c}{\frac{4d}{\lambda_c} \ln(\operatorname{cosec}(\frac{\pi d}{2b})) + \cos^2(\theta_2) + 0.5 \theta_2 + 0.25 \sin(2\theta_2) + (\frac{d}{b}) \left( \frac{\cos(\theta_2)}{\sin(\theta_1)} \right)^2 (0.5 \theta_1 - 0.25 \sin(2\theta_1))}$$

$$\theta_1 = \frac{\pi(w - s)}{\lambda_c} , \quad \theta_2 = \frac{\pi(s)}{\lambda_c}$$

where  $d$  is the gap height,  $w$  is the guide width,  $s$  is the ridge width,  $b$  is the guide height, and  $Z_{PV}$  is the power-voltage impedance computed at a frequency much higher than dominant mode cutoff. Since  $d$  of the ridge waveguide is less than  $b$  of the rectangular waveguide of the same outer dimensions, it is expected for the ridge waveguide to have a lower power handling capability than that of the rectangular waveguide, a drawback that is compensated by the wider bandwidth of the ridge waveguide.

### 1.3.4 Ridge gap waveguide technology

Ridge gap waveguide (RGW) technology is recently invented [12] as a quasi-TEM, low-loss transmission line that doesn't need tight contact between its two parts during assembly. The structure of the RGW is shown in Fig. 1.6. Its lower part is a plate that has a ridge surrounded by a bed of nails on both sides, while the upper part is a texture-free plate. The bed of nails confines the electromagnetic waves to the ridge region by behaving as an Artificial Magnetic Conductor (AMC) at its top surface. The condition for the RGW to operate is to have the gap between the upper plate, and the top surface of the bed of nails less than a quarter wavelength at the highest frequency so that no wave can propagate above the pins, and the only propagation path is above the ridge.

Ridge gap waveguide has a similar dispersion, impedance and field characteristics as ridge waveguides [13]. This makes the power handling capability of ridge gap waveguide comparable to that of ridge waveguides.

RGW has received some interest recently as a high-frequency transmission line for millimeter wave applications for several reasons:

- 1- **Reduced losses:** RGW doesn't need a dielectric substrate to operate, and it has no radiation loss or surface waves, which means the only losses are conductor losses due to finite conductivity, which may be reduced by electroplating.
- 2- **Bandwidth:** RGW has been proved a wideband transmission line by different authors using different techniques like changing the shape of the unit cell [14], and decreasing the gap height above the bed of nails [15]. The bandwidth ratio can reach 3:1 in some cases.

- 3- **Easier to manufacture:** Most waveguides are manufactured in two parts that are soldered after that to provide tight contact between the parts. This tight contact is not necessary for the RGW since it depends on having a gap between the upper and lower plates, which makes it a good candidate for millimeter wave applications.
- 4- **Easier packaging:** Waveguides are normally manufactured as two pieces using (CNC machining or 3D printing), and after that, it is attached together using tightening screws. At high frequencies, the screws might not be tight enough for the waveguide to operate without leakage loss. Ridge gap waveguide needs no tight screws since the bed of nails stops the propagation at the side walls.
- 5- It has also been proved easy to integrate with single ridge waveguide, which means they can be used interchangeably in the same system.

For these reasons (in addition to others that will be clarified in this work), the RGW technology is employed to implement the analog beamforming networks in this work.

## 1.4 Objectives

In light of the previous discussion, it is evident that analog beamforming is the most suitable type for several applications needed nowadays. However, as mentioned, analog beamforming networks can achieve good performance only if suitable components can be designed to fulfill different requirements of the modern wireless communication systems. These requirements include high gain, good coverage, high data rate communications, and adapting to new factors in the environment.

In order to achieve these requirements, this thesis will focus on the following tasks:

- 1- High power transmission lines that can work at high frequencies with minimum losses should be employed to design reconfigurable wideband components. The ridge gap waveguide is chosen in this project as a high-frequency low-loss waveguide.
- 2- These components are integrated to form a Butler matrix to proof the ability of the components to provide reconfigurable beamwidth (beam crossover level), SLL, and beam direction.
- 3- This tunable Butler matrix can be used in several applications. One application is to provide tunable coverage for a sector of a mobile base station. This sector may be covered using a

tunable number of orthogonal beams, which leads to tunable coverage capacity. In addition, if covered by several beams, the gain and beamwidth of the beams can be tuned to provide an interference/coverage compromise similar to the compromise existing between different mobile station macrocells.

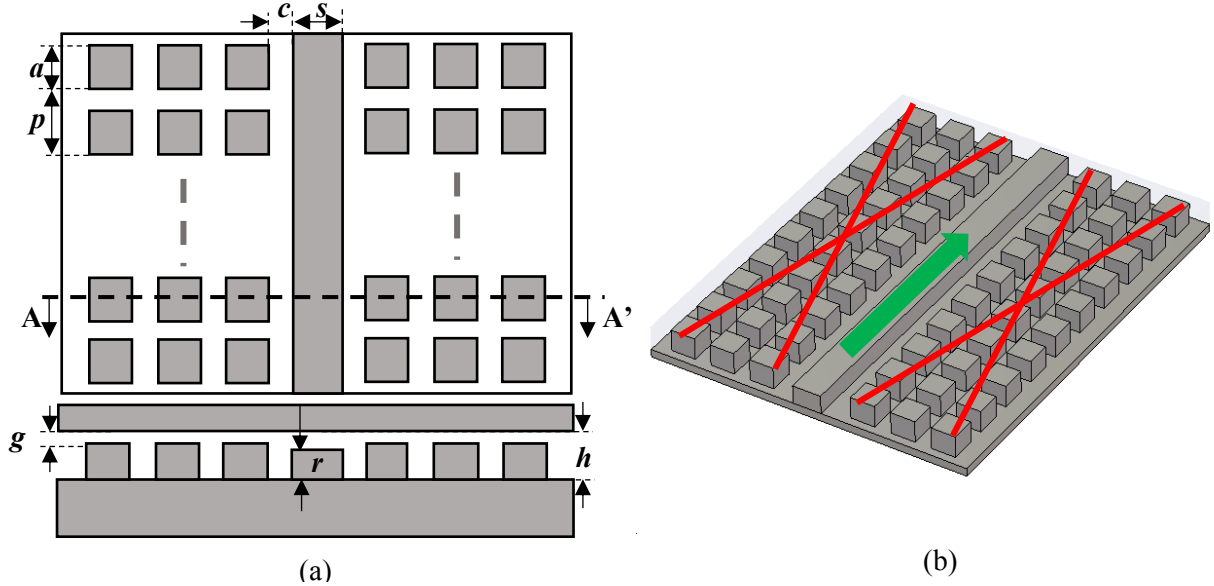


Fig. 1.6. Structure of the RGW: (a) Top and front view. (b) Stop-Go Characteristics of RGW allow propagation along the ridge and prevents it above the pins.

The schematic of the dual-plane Butler matrix will be given in Chapter 7. The first stage is supposed to provide basic Butler matrix functionality. It consists of 2 pairs of broad wall  $90^\circ$  hybrids. Two  $135^\circ$  phase shifters are introduced between the two pairs of hybrids. The output of the last pair of hybrids is swapped in order to obtain the required conventional Butler matrix.

The second stage starts by turning the single ridge waveguide cross-sections into double ridge waveguide. Then the double ridge waveguide is turned into a double ridge gap waveguide, which is used to split each output signal of the first stage into two portions of controllable power ratio, which provides control on amplitude distribution. After that, a reconfigurable phase shifter is cascaded to each of the 8 resulting outputs in order to have phase control.

One advantage of this Butler matrix is its ability to scan the beams on a wider angle than conventional Butler if we use the phase control. The additional progressive phase shift that may be added by the reconfigurable phase shifter of maximum phase shift  $\varphi_{max}$  may be calculated as:

$$\varphi_{extra} = \frac{\varphi_{max}}{N_{antennas} - 1}$$

Another advantage is the ability to taper the amplitudes of the array such that reconfigurable beamwidth and gain are possible, which could lower the interference, widen the coverage range or strengthen the signal. A study for the possible array factors from the proposed Butler matrix will be presented in Chapter 7.

## 1.5 Thesis Contributions and Organization

As mentioned before, the first step in this work is to design wideband RGW components (Transitions, Hybrids, power splitters, and phase shifters). The second step is to put the components together in order to form Butler matrices. Thesis contributions may be listed as follows:

- 1- Use of beamforming networks to provide tunable capacity and coverage for mobile base station sectors instead of the conventional use of beamforming networks in switching one signal between different directions by choice.
- 2- Two wideband coaxial to ridge gap waveguide transitions (inline and vertical) that cover more than 2.9 to 1 bandwidth ratio with return loss better than 10 dB back to back.
- 3- Hybrid coupler using ridge gap waveguide with arbitrary coupling level ranging from 3 to 33 dB working on 40% bandwidth.
- 4- Analysis of the asymmetric double ridge waveguide and calculation of its impedance, which may be used in a double ridge to single ridge waveguide transitions.
- 5- Design of wideband power splitter of arbitrary splitting ratio from 3 dB to 10 dB working on more than 100% bandwidth.
- 6- A real-time reconfigurable power splitter that works on 40 % bandwidth and can provide any power splitting ratio.
- 7- A reconfigurable phase shifter that works on 33% bandwidth and can provide a reconfigurable relative phase shift from 0° up to 200° with phase balance  $\pm 15^\circ$ .

This document is organized as follows: Chapter 2 presents a literature survey on different Butler matrices in the literature and literature surveys on different components needed to implement the tunable Butler matrix. Chapter 3 shows the design, and results of two different transitions from

the coaxial transmission line to RGW, one transition is a vertical transition, while the other is an inline transition. Chapter 4 shows the design of an arbitrary ratio power splitter with more than 100 % percentage bandwidth using single ridge waveguides, and a tunable power splitter of around 40% bandwidth using the ridge gap waveguide with its results. In addition, the asymmetric double ridge waveguide is explained and analyzed. Chapter 5 presents the design and results of a 90° hybrid coupler having an arbitrary power division ratio from 3 dB up to 33 dB, which would be very useful in Butler matrices. Chapter 6 presents different phase shifters used in the Butler matrix design. Chapter 7 presents the full Butler matrix that has the ability to produce different radiation patterns that were not possible using the conventional Butler matrix. Chapter 8 is a conclusion and future work.

# Chapter 2

## Literature Survey

In this chapter, a literature survey on different Butler matrix topologies in different technologies is presented with several examples on tunable beamforming networks. In addition, literature surveys on the different devices used in Butler matrix are presented for the sake of comparison with the components designed in this work to be used in the tunable Butler matrix.

### 2.1 Butler Matrix

In this section, a literature survey on Butler matrix topologies in printed and waveguide technologies is presented.

#### 2.1.1 Printed circuit technologies

Several Butler matrices have been proposed in the literature using microstrip, substrate integrated waveguide (SIW), and coplanar waveguide (CPW) technologies. In [16], a  $3 \times 3$  Butler matrix based on Substrate Integrated Waveguide (SIW) technology is designed using  $4.77/1.76$  dB quadrature hybrid coupler removing the  $2^m$  restriction on the number of input and output ports. In [17], [18] and [19], a double-layer structure is used to avoid using crossovers in  $4 \times 4$  and  $8 \times 8$  Butler matrices fabricated using microstrip technology. In [17], the transmission S-parameters are in the range of  $-7 \text{ dB} \pm 3 \text{ dB}$  with output ports phase shifts of  $45^\circ \pm 7^\circ$  and  $135^\circ \pm 6^\circ$  working on frequency range from 4 GHz to 10 GHz. In [18], the transmission S-parameters are in the range of  $-7.5 \text{ dB} \pm 1.5 \text{ dB}$  with phase error less than  $3.5^\circ$  from 18 GHz to 40 GHz. The return loss and isolation are better than 15 dB, while insertion loss is better than 3.2 dB over the entire bandwidth. In [19], a novel  $4 \times 4$  dual-layer Butler matrix is implemented using CPW technology to work around 5.8 GHz with transmission S-parameters around  $-7.5 \text{ dB}$  and return loss better than 25 dB over 6% bandwidth. In [20], a special arrangement of Butler matrix output ports is used to avoid using crossovers in a dual-band  $4 \times 4$  Butler matrix working at 5 and 8 GHz. In [21], a  $45^\circ$  crossover implemented using defected ground structure in microstrip technology is used to construct a  $4 \times 4$  Butler matrix without phase shifters to operate around 900 MHz resulting in a 14 % size reduction. In [22], an ultra-wideband  $4 \times 4$  Butler matrices is designed using multi-section coupled line couplers in microstrip technology working from 2 to 12 GHz. In [23], a miniaturized

Butler matrix based on hybrid slots is designed using microstrip technology to achieve 56% area reduction and 14 % bandwidth. In [24], a 9×9 Butler matrix is designed using 3×3 hybrid couplers in order to use it in the 2D Butler matrix. In [25], a 4×8 Butler matrix is designed by using a 4×4 Butler matrix followed by splitters and 180° fed-antennas to achieve lower sidelobe level than the conventional Butler matrix. In [26], an AMC-packaged Butler matrix is designed to work around 30 GHz, achieving a bandwidth of 14 % with a transmission amplitude balance of  $\pm 0.8$  dB around 7 dB.

Tuning has been included by several authors in the operation of the Butler matrix in order to provide more beams while maintaining a compact size. In [27], an extended 4×4 Butler matrix is implemented using microstrip technology to produce 16 switchable beams instead of 4 beams using a 2-bit phase shifter, which is cascaded after the Butler matrix to control the progressive phase shift. The two-bit phase shifter is synthesized using diodes, and the whole design is working around 2.4 GHz, and over 17% bandwidth. In [28], a tunable reflection-type phase shifter is cascaded to the outputs of an 8×8 Butler matrix to provide extra  $\pm 20^\circ$  at each output with over 50% bandwidth around 2.4 GHz. In [29], both Sidelobe Level (SLL) and beam directions of an 8×8 Butler matrix are reconfigured around 2.45 GHz. The SLL is reconfigured by using multiple port excitation (feeding two phase-shifted versions of the same signal into two input ports) to produce a cosine-tapered pattern. The beam direction is controlled using a switched line phase shifter circuitry at the output ports. In [30], a 4×4 Butler matrix with tunable couplers is designed to achieve variable SLL of -13.6, -20 and -30 dB. The variable coupling levels are achieved by changing the height of a 5×7 array of cylindrical rods in steps. In [31], reconfigurable couplers are used instead of traditional 3 dB couplers to extend the number of beams of a Butler matrix working over 30% bandwidth around 2.4 GHz. In [32], a beam switching/steering Butler matrix is designed to work from 1.6 GHz to 2.8 GHz using multilayer stripline technology. The amplitude and phase errors are  $\pm 2.2$  dB and  $\pm 20^\circ$ , respectively. The beam directions may be tuned in space using phase shifters added at the end of the Butler matrix, providing phase shifting range in excess of 120°. It is worth noting that most of the work done on tunable Butler matrix is done using printed technology around 2.4 GHz due to the availability of reconfiguration mechanisms (diodes) at this frequency band in printed technologies.

### 2.1.2 Metallic waveguide technologies

On the other hand, different Butler matrices are proposed using waveguides. In [33], a ridge waveguide  $4 \times 4$  Butler matrix was fabricated in 1 layer to work at 60 GHz, where a second layer is used for antenna coupling. An SLL control circuit is employed at the outputs of the Butler matrix to reduce SLL for all input signals. The matrix operates from 58.2 GHz to 62.5 GHz, where the return loss and isolation are better than 10 dB, and SLL is better than 26 dB in simulation (17.5 dB in measurement). In [34], an  $8 \times 8$  Butler matrix is implemented using planar waveguides to operate from 27 GHz to 30 GHz with return loss and isolation better than 25 dB. In [35], a  $4 \times 4$  Butler matrix is implemented using inverted microstrip gap waveguide technology, achieving better than 20 dB return loss and isolation over 8.5 % bandwidth around 57 GHz. In [36],  $4 \times 4$  Butler matrix design is designed on a single plane using GGW technology to work around 26 GHz. In [37], a post wall waveguide is used to realize  $8 \times 8$  Butler matrix on 1 plane with 50% size reduction, 0.4 dB amplitude error at each port and return loss better than 30 dB. In [38], a dual-plane waveguide Butler matrix is designed to work at 8.45 GHz.

Dynamic beamforming in waveguide technology is required for antenna arrays in practical applications like satellite systems. However, normally, several devices are integrated together and/or ferrites are used to achieve variable power division for full array control. In [39], a variable-coverage satellite required the design of a tunable beamforming network using variable power dividers. The variable power divider is formed of one magic tee, one  $90^\circ$ -hybrid and two variable phase shifters. In [40], two 3-dB  $90^\circ$  hybrids are connected using two variable phase shifters to produce variable power division. The variable phase shifters are made using other two  $90^\circ$ -hybrids with movable shorts at two terminals of them, producing 16% percentage bandwidth. In [41], a reconfigurable power divider is designed to work on Ku-band (10-12 GHz) using a waveguide rotating polarizer, field component collector and separator (implemented using OMT). Cascading several components together increases the size and losses of the power divider, which would favorably be made of only 1 device if possible. Using ferrites increases the cost and insertion loss of the overall system. On the other hand, antenna arrays in [39], [41] are capable of point to point communication at the same time, unlike [42], where Butler matrix can achieve point to multipoint satellite communication at the same time.

## 2.2 Waveguide Adapters

Several transitions were developed by authors to couple the power into the RGW. In [43], a waveguide to RGW transition (through coaxial probe) provides a 20 % bandwidth with a return loss better than 15 dB, where the coaxial probe opening is made through the ridge. In [44], a microstrip to RGW transition with 25.4% bandwidth, better than -15 dB matching level and better than 0.85 dB insertion loss is presented. An even better microstrip transition is presented in [45] with return loss better than 14.15 dB, and insertion loss better than 0.32 dB over 55% bandwidth; however, unlike [44], gap height must equal substrate thickness, so gap heights are determined according to the commercially available substrates' thicknesses. In [46], an inverted microstrip gap waveguide is fed by a rectangular waveguide through a planar probe transition to utilize the inverted microstrip for feeding a horn antenna array. This waveguide-to-inverted microstrip gap waveguide transition is done in two configurations, the best of which provides a bandwidth of 45 % with -15 dB matching level and 0.5 dB insertion loss. In [47], the non-contact effect of a printed circuit board (PCB) with conducting pins is explained in the case of soft substrates, and some solutions are suggested. In [48], a microstrip RGW to WG-15 waveguide is presented with -15 dB back to back matching level and low insertion loss in the frequency band from 57 GHz to 66 GHz.

In [49], a defected ground slot is used to feed an RGW using a microstrip line fed by inline coaxial cable. The bandwidth of 40 % with -15 dB matching level and 0.2 dB insertion loss is achieved. However, this transition needs space on top of RGW to be able to house the feeding microstrip line. In some situations, like feeding a waveguide broad wall coupler, such space might not be available. Therefore, several stairs will have to be placed between the coupler port and the transition, which deteriorates the matching level. Besides, 40% bandwidth does not cover all the possible RGW bandwidth. In [50], an F-band microstrip to RGW transition is designed with a return loss better than 15 dB and insertion loss of 1.3 dB over 25.3% bandwidth; however, PCB integration and fabrication tolerances degraded the performance. A Monte-Carlo analysis is performed to investigate the sensitivity of S-parameters at such high-frequency band to some parameters like unequal heights of PCB at the beginning and end of the guide. In [51], a transition between ridge gap waveguide and microstrip line is simulated using SIW as an intermediate step resulting in an insertion loss of 0.35 dB and a return loss better than 20 dB over the W-band (37.8

%). In [52], a vertical coaxial to RGW transition operating from 10 GHz to 23 GHz with a return loss better than 15 dB and an insertion loss better than 0.4 dB over the entire bandwidth, is presented.

On the other hand, single ridge waveguide transitions are numerous in literature. In [53], a coaxial to single ridge transition is designed using TEM to TE mode converter to achieve better than 1.32 VSWR and better than 1 dB insertion loss from 18 GHz to 40 GHz. In [54], several techniques to design a wideband coaxial to regular waveguide transition are proposed, most of which use ridge waveguides as a transitional stage between a coaxial line and waveguide with a bandwidth ratio reaching 3 to 1 in some tapered-ridge cases. In [55], a vertical coaxial to single ridge waveguide transition provides a voltage standing wave ratio (VSWR) better than 1.2 in the frequency band from 2 GHz to 5.6 GHz using a V-shaped back cavity. The coaxial inner conductor is coupled to waveguide through its top wall and connected to the ridge through a tapered matching post. In [56], an inline coaxial to single ridge waveguide transition achieves VSWR better than 1.28 in the frequency band from 7 GHz to 11 GHz, where a magnetic coupling loop is used to compensate for the effect of the steps in the ridge. In [57], a coaxial-to-double ridge waveguide transition is designed to operate between 8 GHz and 18 GHz with VSWR better than 1.6 over the whole band. In [58], a coaxial to double ridge waveguide transition is designed to work in RF cavities from 0.5 GHz to 2.5 GHz with VSWR better than 1.6 for the whole band.

In [59], a coaxial to double ridge waveguide transition is designed to operate from 0.7 GHz to 2.5 GHz with VSWR better than 2, where a tapered coaxial line is used to enhance the matching. In [60], an inline coaxial to double ridge waveguide transition is shown to work from 6 GHz to 18 GHz with a return loss better than 18 dB, insertion loss better than 0.3 dB and 30 mm total length. In [61], an inline coaxial to single ridge waveguide transition is used to feed a wideband filter using coaxial to stripline transition then stripline to ridge waveguide transition. The transition works from 3 GHz to 9 GHz with a return loss better than 20 dB over the whole band. In [62], a vertical coaxial to double ridge waveguide achieves better than 2:1 bandwidth with a return loss better than 15 dB. In [63], a vertical coaxial to single ridge waveguide transition is implemented to feed a broadband ridged horn antenna. The antenna works from 4 GHz to 40 GHz with -15 dB matching level with no information on the back to back behavior of the separate transition. In [64], a vertical coaxial to double ridge waveguide transition is designed to feed a

double ridge horn antenna. The transition uses a cylindrical element at the coaxial pin contact position to allow tuning and achieves return loss better than 10 dB (with antenna) from 6 GHz to 18 GHz. In [65], a vertical coaxial-to-double ridge waveguide transition with pyramidal back short is designed to feed a horn antenna from 8 to 18 GHz with VSWR less than 2 over the entire band. In [53], an inline coaxial-to-double ridge waveguide transition demonstrates VSWR better than 1.3 from 18 to 40 GHz. The same band is covered by [66] using a vertical coaxial transition, achieving better than 20 dB return loss. In [67], an inline coaxial to single ridge transition is used to feed a high pass filter with a return loss better than 15 dB from 4 GHz to 17 GHz with the help of coaxial cylinder and a modified impedance transformer. In [68], an inline coaxial to single ridge waveguide transition is used to feed a bandpass filter with the coaxial pin placed above the ridge. The transition achieves return loss better than 17 dB in the band from 3.1 to 10.6 GHz. In [69], a vertical coaxial to double ridge waveguide achieves VSWR better than 1.4 in the band from 8 GHz to 18 GHz. In [70], a coaxial to double ridge waveguide transition is employed to feed a horn antenna. This transition has a return loss better than 15 dB from 10 to 100 GHz in simulation; however, measurements show return loss better than 9 dB and return loss around 2 dB from 36 GHz to 100 GHz. In [71], an inline coaxial to double ridge waveguide is used to connect the output of a microstrip Rotman lens to a double ridge horn antenna. The transition has a return loss better than 15 dB from 6 GHz to 18 GHz.

In [72], an inline coaxial to a single ridge waveguide transition is designed to feed an RGW. A tuning capability is employed to tune the operating band of this transition. In [73], a vertical coaxial to single ridge waveguide transition is used to feed the RGW on 4:1 bandwidth and using several variations of the ridge waveguide cross-section (single ridge, symmetric and asymmetric double ridge waveguide). The structures and results of both transitions are presented in Chapter 3.

## **2.3 Power Splitters and Switches**

Power splitters are necessary microwave devices in several applications like antenna arrays and several microwave systems. It can be used in power amplifiers to amplify the signal using several amplifiers instead of one for graceful degradation of performance in case of component failure. In [74], an 8-way power splitter is designed using Ridge Substrate Integrated Waveguide (RSIW)

to have a return loss better than 10 dB and an average insertion loss of 0.7 dB from 5 GHz to 10 GHz. In [75], a 4-way power divider is designed using RSIW to have a return loss better than 10 dB and an insertion loss better than 1 dB from 4 GHz to 8 GHz. In [76], a 32-way power splitter is fabricated using ridged waveguides to have a return loss better than 10 dB on a 50% bandwidth. In [77], Ridge Gap Waveguide (RGW) and Groove Gap Waveguide (GGW) technologies are used interchangeably to create up to 16-way power splitting with a return loss better than 15 dB on the frequency band from 57 GHz to 66 GHz. In [78], a rectangular waveguide T-junction splitter is used to design the feeding network of a horn antenna array. The splitter works on the frequency band from 57.2 GHz to 58.8 GHz with a return loss better than 20 dB for different power splitting ratios. In [79], a microstrip to waveguide power splitter/combiner is designed to work from 26 GHz to 32 GHz and with a return loss better than 20 dB to be used in a 28 GHz receiver. In [80], a Y-junction dual-band power divider is designed using complementary resonators on entirely planar structures at 0.9 GHz and 1.8 GHz (50% bandwidth). In [81], a two-way multistage Wilkinson power divider is designed for use in the vector network analyzer. The divider is covering the frequency band from 8 GHz to 67 GHz achieving a return loss better than 10 dB and isolation better than 20 dB. In [82], a T-shaped transmission line has been used to design two Wilkinson power dividers working at 1 GHz and 2 GHz with the aim of harmonic suppression, achieving a bandwidth of 40% and 20%, respectively. In [83], a multiway multisection resistive divider is designed to work on a 100% bandwidth by using delay lines to connect 2-way dividers. In [84], a 10-way conical line power combiner is designed using a circuit model to work on 46 % bandwidth in the X-band achieving a return loss better than 18 dB.

On the other hand, tunable power dividers were presented in the literature in printed and waveguide technologies. In [85], a reconfigurable power divider working at 1 GHz is designed using printed circuit technology. Power split ratio and in/out of phase control is done using varactor diodes. In [86], a T-type impedance transformer loaded with a variable capacitor is used to provide a real-time tunable power division ratio for an orthogonal power divider from 2:1 to 4:1 in a band from 1.98 GHz to 2.02 GHz. A varactor diode is used to provide voltage-controlled capacitance. In [87], three pin diodes are used to achieve power division ratio higher than 1:5 up to 1:0 transmission mode over 4.6% bandwidth around 5 GHz. The 1:0 transmission mode shows an insertion loss of 1.6 dB due to the losses in the diodes. In [88], a 1x4 power divider works between 2.3 GHz to 2.6 GHz to provide from 1:1 to 1:4 division ratios. Transmission losses are

between 1.2 dB to 1.9 dB. In [89], a reconfigurable three-way power divider is designed at 2 GHz. The divider can work in 1-way, 2-way, and 3-way modes with insertion losses of 0.2 dB, 3.2 dB, and 4.87 dB, respectively. In [90], a power divider of 4 different states (1:0, 0:1, 1:j, 1:-j) is designed and fabricated using 6 switches to work at 2.5 GHz with 30% bandwidth. In [91], a reconfigurable function circuit working as a switch or a power divider is designed using SIW and HMSIW to work from 4.6 GHz to 5.3 GHz. As shown, in printed circuit technology, the tuning is usually done using varactors or pin diodes, which are lossy, or expensive at high frequencies.

In waveguide technology, it is less convenient to use diodes for tuning, since this requires transitions from waveguide to the substrate, where the diode will be used, and vice versa. The average power handling capability will be limited due to substrate properties, and losses will increase due to the use of dielectric. That's why authors used different techniques to design variable power splitters like in [40], where a variable power divider is designed for Ku-band satellites using 2 hybrids and 2 reconfigurable phase shifters. The reconfigurable phase shifters are reflection type, where 2 hybrids have each of their ports terminated by a movable short circuit used to control the phase shift. The final prototype has 0.15 dB insertion loss and 25 dB isolation working from 10.95 GHz to 12.75 GHz for Eutel satellite applications. A similar variable power divider is used in [39] to feed horn clusters to be used in a variable-coverage satellite antenna system. In this case, 2 phase shifters are placed between a Magic-Tee (difference port terminated by a load) and 3-dB hybrid. Insertion losses are 0.3 dB per divider, but feeding 19 horns requires a hierarchy connection of this power divider, which ends up in 1.5 dB loss per path with 10% frequency bandwidth. In this type of variable power dividers, 4 couplers are used in order to achieve variable power splitting, which requires a lot of space. Another example of variable power dividers is in [41], where a reconfigurable power divider is designed to work on Ku-band (10-12 GHz) using a waveguide polarizer and two Ortho-Mode Transducers (OMT), where the rotating polarizer decides the splitting ratio. In [92], a ferrite variable power divider is designed based on 2 magnets on top and bottom of a Y-junction loaded with magnetic pucks and magnetic returns in the middle of the junction, where the magnetic bias direction controls the power split ratio. Ferrites are known for being expensive and lossy. A review of waveguide power splitters is shown in [93], where a mechanical type of power splitters, which uses a rotating vane is used to split the power between two horizontal waveguides. The means to achieve tight contact between the vane

and the upper and lower waveguide walls are not mentioned, which could cause a problem at high frequencies. Also, the results of this mechanical splitter are not shown in [93].

On the other hand, switches are important devices for reconfiguration of RF and antenna systems. Examples of waveguide switches in literature are numerous. In [94], a MEMS capacitive-contact waveguide switch working from 500-750 GHz is designed to provide isolation better than 20 dB and insertion loss better than 2.3 dB in the block/unblock states. The return loss approaches or equals 10 dB in the unblocked state. In [95], monolithic RF switch is done using waveguide wafers of reduced height (50  $\mu\text{m}$ ) working from 60 GHz to 75 GHz with 0.2 dB ON-state IL and better than 22 dB isolation in the OFF-state; however, the waveguide S-parameters without the MEMS switches show very high IL. The most important figures of merit for a switch are: insertion and return losses of the switch in the ON state and the isolation in the OFF state.

In [96], a power splitter is designed using ridge waveguides to provide an arbitrary power split ratio. In [97], a novel reconfigurable power splitter using ridge gap waveguide technology is invented. The designs and results of both splitters are presented in Chapter 4.

## 2.4 Couplers

Directional couplers have been used in microwave engineering for more than 50 years due to their importance in several systems and applications like power measurement, radar systems and beamforming networks [8]. Couplers may be categorized using several criteria like geometrical structure, application, and coupling levels. For example, couplers may be divided, according to their coupling level, into tight-coupling couplers (Coupling  $> 10$  dB) and loose coupling couplers (Coupling  $< 10$  dB). Examples of the tight coupling level couplers in literature are the  $90^\circ$  and  $180^\circ$  hybrid couplers, which are conventionally 3 dB couplers with a phase difference between the output ports equal to  $90^\circ$  or  $180^\circ$ , respectively [10]. An example of loose coupling level couplers is the Bethe hole coupler, which is designed using a hole in the common wall between two parallel or crossed waveguides according to the small aperture diffraction theory [98]. Increasing the bandwidth of Bethe hole coupler requires a large number of holes. For example, in [99], a large number of holes is used to design broad wall ridge waveguide couplers. The suggested couplers achieve directivity higher than 40 dB with 2.4:1 bandwidth or directivity higher than 35 dB with 3.6:1 bandwidth. The number of holes needed theoretically to achieve

such performance is 101 holes. The operating bandwidth is from 10.9 to 26.5 GHz with 11 ( $\pm 1$ ) dB coupling and 38 dB directivity using 83 holes within a length of 275 mm, which is so long for some applications. Several authors tried to balance the size and bandwidth requirements in order to design practical broad wall couplers. In ridge waveguides, a crossed double ridge waveguide (DRG) coupler in [100] achieves a bandwidth of 3 octaves, with 50 dB coupling level, better than 15 dB return loss (RL) and better than 15 dB directivity using one cross-shaped slot. In [101], a 4-port 3 dB splitter achieves better than 20 dB return loss and 24 dB isolation over 3.5 GHz in K-band. In [102], three types of holes (square, triangular and circular) are compared for best bandwidth performance to show that square hole can achieve wideband with 40 ( $\pm 2$ ) dB coupling level over the band from 2 to 4 GHz by increasing the number of holes to twelve, where distance between holes is in the order of half guided-wavelength. In [103], a procedure to design a single ridge branch-line 3 dB couplers is provided and used to design a coupler with RL and isolation better than 25 dB from 2.9 to 5.5 GHz. In [104], a single ridge branch line coupler (of 5 branches) is designed to achieve 3 dB coupling over 46% bandwidth with  $\pm 0.4$  dB variation and RL and isolation better than 25 dB. In [105], an 8-hole Bethe coupler with tapered aperture radii over a length of 40 mm is designed to achieve a flat coupling of 30 dB and good directivity (28 to 50 dB) on the Ku-band.

On the other hand, several directional couplers were designed based on RGW in literature. In [106], a Groove Gap Waveguide (GGW) broad wall coupler is designed to provide an adjustable coupling coefficient using a replaceable corrugated metallic sheet of length 50 mm. Coupling is done by means of 17 inclined slots in the sidewalls whose inclination angle determines the coupling level. This design provides 9 dB and 18.5 dB coupler from 30 to 40 GHz with RL better than 17 dB on the first half of the band (and better than 12 dB on the second half) and isolation better than 25 dB. In [107], an RGW hybrid 3 dB coupler of length 13 mm is designed to work from 13.5 to 16.5 GHz with isolation and RL better than 14 dB.

In [108], a ridge gap waveguide coupler is realized using ridges' proximity to achieve strong 3 dB coupling around 35 GHz (32-38 GHz) with a return loss better than 10 dB and isolation better than 15 dB. In [109], a groove gap waveguide 3 dB coupler of length 32 mm is designed to work from 13 to 15 GHz with return loss and isolation better than 20 dB and phase difference equal to ( $90^\circ \pm 0.5^\circ$ ) between the through and coupled ports. In [110], a rat-race coupler is designed using

RGW technology to work from 15.25 to 17.75 GHz with RL better than 15 dB, and  $180^\circ \pm 5^\circ$  phase difference between the coupled and through ports. In [111], a broad-wall 6-aperture 3 dB hybrid coupler is developed using printed RGW, achieving better than 15 dB return loss and better than 17 dB isolation between output ports between 57 GHz and 64 GHz. The length of the coupler is two free-space wavelengths. The bandwidth of the narrow-slot broad wall couplers, in general, is directly proportional to the number of slots; hence, the size. Furthermore, some couplers need many small slots in order to achieve high coupling levels, which increases the size and manufacturing complexity of the structure. In addition, the same plane couplers like those in [107], and [108] are not advantageous for use with beamforming networks due to the increased size and the need for crossovers.

Multimode couplers are couplers dependent on the existence of more than 1 mode in a coupling region. The theory of operation for this coupler is based on the existence of two modes in the coupling region of the coupler. The two modes are antisymmetric at the isolation port to achieve high isolation, and symmetric at the coupling port. This theory has been used in several papers before. In [112], Riblet hybrid employs  $TE_{10}$  and  $TE_{20}$  modes in the multimode region, where a part of the sidewall is removed. In [113],  $TE_{10}$  mode, and ( $TE_{11}/TM_{11}$ ) mode are used in a rectangular waveguide broad wall coupler. In [114], [115], and [116], a combination of  $TE_{10}$  waveguide mode, and TEM mode is used to design a broad wall coupler. The multimode coupler concept is used in Chapter 5 to design a  $90^\circ$  hybrid using RGW technology.

## 2.5 Reconfigurable Phase Shifters

The phase shifter is an important component of several microwave systems like beamforming networks and antenna arrays [10]. It is used to adjust the phase of each antenna element and consequently change the direction of the beams. Phase shifters may be classified into fixed and reconfigurable phase shifters. In fixed phase shifters, only one type of phase shift is achievable per device, although with a different set of parameters, an arbitrary phase shift value might be achieved. On the other hand, reconfigurable phase shifters can provide flexible operation of a microwave system to satisfy variable requirements of practical applications. That's why it received considerable interest from different authors. In [117], a reconfigurable Negative Reflect Index (NRI) phase shifter is proposed based on a series capacitor and shunt inductors. The continuous phase shift is done using two groups of pin diodes, and a varactor. In [118], a

digital/analog hybrid phase shifter is used to provide antenna array scanning at 9 GHz. Analog phase control is introduced by the biasing magnetic field, while digital phase control is introduced using PIN diodes.

In [119], a multistage digital type MEMS phase shifter is proposed achieving 2.1 dB insertion loss and better than 15 dB return loss per 45° phase shifting block over a wide frequency band. Several other examples of phase shifters include using liquid crystals in waveguides at high frequency [120] working on the W-band and using MEMS high impedance surface as a reflector in a reflection type phase shifter [121] to work from 70 GHz to 95 GHz. In [122], an SIW reflection-type phase shifter is designed using hybrid junction, and variable reflective loads (voltage-tuned capacitance) to work from 11.3 GHz to 11.8 GHz with 360° phase shifting range. In [123], a dielectric phase shifter is designed for a steerable 60 GHz antenna in coplanar waveguide technology to achieve a relative phase shifting range of 210°. In [124], depth-controlled corrugations are used to provide a reconfigurable phase shift up to 230° while maintaining return loss better than 40 dB.

In [125], two examples of mechanically tunable phase shifters are introduced for high power applications, where no dielectrics are introduced. In one example, a metallic fin is inserted vertically in a waveguide in order to introduce the phase shift. The phase shift value depends on the length of the inserted fin, and can reach the value of 360° for a total length of 20 cm. In the second example, a short-slot hybrid is used to create a reflection type phase shifter with the tunable load realized using a movable short circuit. However, in both phase shifters, the frequency, and phase error information is not given. In [126], a reflection type phase shifter is realized using a short slot hybrid in rectangular waveguide technology. Two ports of the hybrid are short-circuited, and two tunable screws are employed to change the reflection phase of the short circuit. The reconfigurable phase shifter may provide up to 180° phase shift from 18 GHz to 22 GHz. The return loss is better than 20 dB, and the phase error is 70° over the whole band. According to the previous works, power handling capability, phase balance, phase tuning range are considered as the figures of merit for the reconfigurable phase shifter. In addition, the phase shifter should transfer the power between the two ports with minimum losses. In Chapter 6, a reflection-type phase shifter is introduced to provide a tunable phase shift up to 200° on the frequency band from 28 GHz to 39 GHz with a phase error of  $\pm 15^\circ$ .

## Chapter 3

# Wideband Transitions for the Ridge Gap Waveguide

### 3.1 Introduction

Designing an RGW transition has received a lot of attention in the recent years due to the fact of RGW being a non-standard transmission line, and due to the lack of transitions between RGW, and standard transmission lines like coaxial lines, rectangular waveguides, and microstrip lines. In [13], the single ridge waveguide is proved to have similar dispersion diagram and characteristic impedance to those of ridge gap waveguide. It is also shown that a single ridge waveguide may be used to feed the ridge gap waveguide directly, which means transitions between single ridge waveguides, and coaxial lines may be used to feed the ridge gap waveguide. In this chapter, two coaxial to single ridge waveguides are designed to feed RGW with bandwidth ratios better than 2.9:1. A comparison of the different RGW transitions in the literature is shown in Table 3.1. The structure of each transition and its results are presented next.

### 3.2 Wideband Inline Transition

In this section, an inline coaxial-to-ridge waveguide transition is designed, manufactured and measured to feed RGW. The transition is tested for two different RGWs. The design and results of the inline transition are presented next.

#### 3.2.1 Ridge gap waveguide design

The first step in the design of any RGW device is determining the parameters for a specific band of operation. This process is done in two steps: Determining the stop band of the bed of nails by 2D eigenmode simulation of one unit cell, and determining the single mode bandwidth of RGW by 1D eigenmode simulation of a single row of RGW. In this work, a wideband transition covering the band from 11.5 to 33 GHz is designed. As a result, two RGWs are designed to test the transition on all its band. *RGW A* operates from 12.5 to 27 GHz, while *RGW B* operates from 20 to 30 GHz. The parameters of each RGW is shown in Table 3.2 following the notation of Fig. 1.6. Fig. 3.1(a) presents results of 2D periodic analysis of a unit cell for *RGW A* as obtained from CST Microwave Studio showing a stop band from 11.5 GHz to 30 GHz, while Fig. 3.1(b)

Table 3.1: Comparison between reported RGW transitions in the literature

Reference	Transition		Matching	
	From	To	Band	RL
[45]	Microstrip	RGW	55 %	14.5 dB
[48]	WR15	Microstrip RGW	57-66 GHz	15 dB
[49]	Microstrip	RGW	40%	15 dB
[50]	Microstrip	RGW	25.3 %	15 dB
[52]	Coaxial	RGW	10-23 GHz	15 dB
[72] (Inline)	Coaxial	RGW	11.5-33 GHz	15 dB
[73] (Vertical)	Coaxial	RGW	12.8-43 GHz	15 dB

shows 1D periodic analysis results for one row of  $RGW A$ , where single-mode bandwidth is from 12.5 GHz to 27 GHz. Results were verified using ANSYS. Similar analyses are performed for  $RGW B$  and the results in Fig. 3.2 show that the stop band of the unit cell is from 20 to 40 GHz, while the single-mode bandwidth is from 20 to 30 GHz. The shift between the 2D and 1D-dispersion diagrams is due to the existence of the ridge in the  $1D$  simulation, which makes the bed of nails infinite in only 1 direction, unlike the 2D-dispersion diagram. After designing the band of the RGW, the S-parameters of the RGW are tested by using a wave port. The position and size of the wave port are studied by different publications. In [52], the port used to feed the RGW is the one in Fig. 3.3(a), which takes port height as  $2.5 \text{ gap height}$ , and port width as  $2.5 \text{ pin width}$ . The port suggested by [13] is the port of the equivalent single ridge waveguide, which ends transversely at the edge of the first pin with a height equal to the total RGW height, as shown in Fig. 3.3(b). A comparison of the S-parameters for the two ports while feeding  $RGW B$  is provided in Fig. 3.3(c). It is shown that the wave port suggested here achieves better matching level on most of the band than the one in [52], which makes it the best for the transition. The port in Fig. 3.3(b) appears to capture some of the power missed by the one in Fig. 3.3(a) (the power beside the ridge).

### 3.2.2 Inline transition to the ridge gap waveguide

The transition geometry is shown in Fig. 3.4, as inspired by [127] and [128]. The input port is a  $50 \Omega$  coaxial connector whose inner pin is in contact with a rectangular coaxial. The rectangular coaxial is attached to a single ridge waveguide. The capacitance between the chamfers at the rectangular coaxial corners and the waveguide wall is reduced. Matching is enhanced by a groove of depth  $h_g$  below the coaxial pin as in [128]. The values of different parameters are in Table 3.3.

Table 3.2: Values of different parameters for the two RGWs according to Fig. 1.6 notation.

<i>RGW A</i>		<i>RGW B</i>	
Parameter	Value	Parameter	Value
$s_a$	3.5 mm	$s_b$	3.5 mm
$c_a$	3.1 mm	$c_b$	3.1 mm
$a_a$	3 mm	$a_b$	2.3 mm
$p_a$	5 mm	$p_b$	4.5 mm
$h_a$	4 mm	$h_b$	3 mm
$g_a$	0.3 mm	$g_b$	0.7 mm
$r_a$	3 mm	$r_b$	2.3 mm

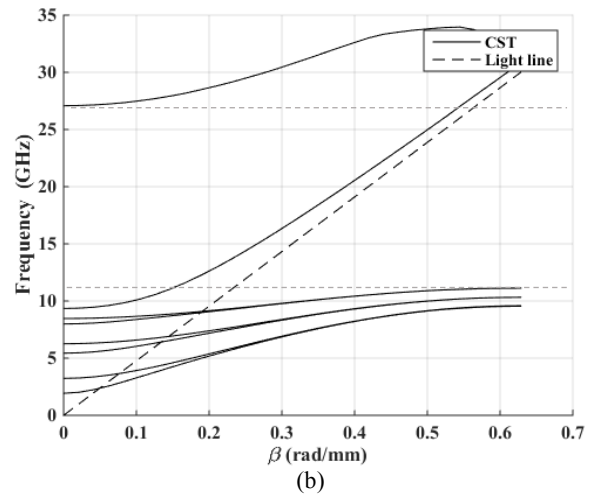
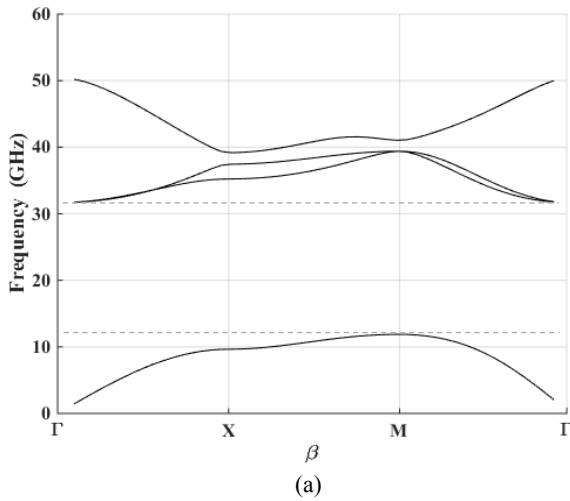


Fig. 3.1. (a) 2D-dispersion diagram of a unit cell of *RGW A* using CST. (b) 1D-dispersion diagram of a single row of *RGW A* using CST.

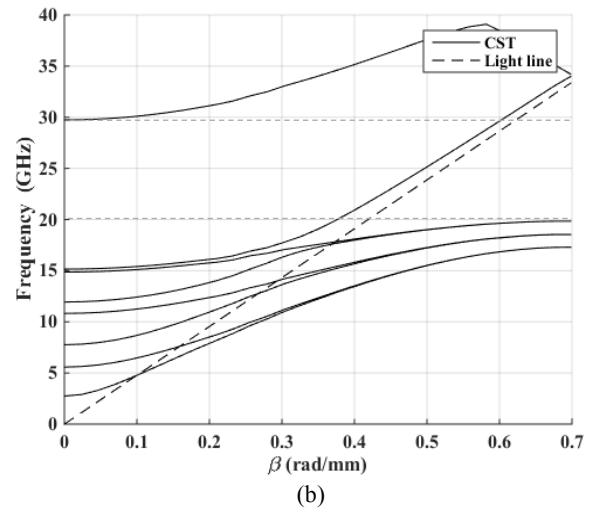
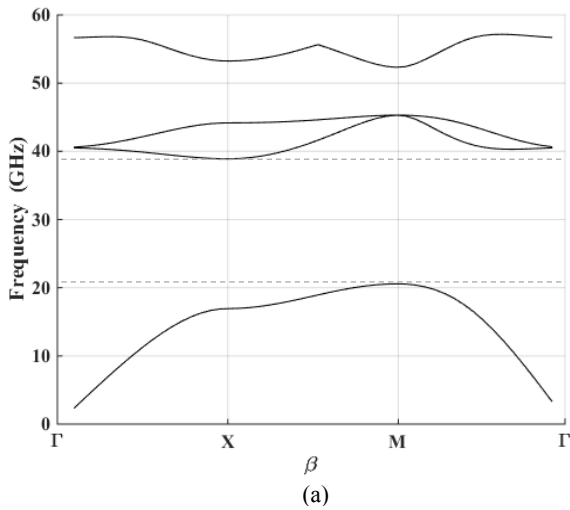


Fig. 3.2. (a) 2D-dispersion diagram of a unit cell of *RGW B* using CST. (b) 1D-dispersion diagram of a single row of *RGW B* using CST.

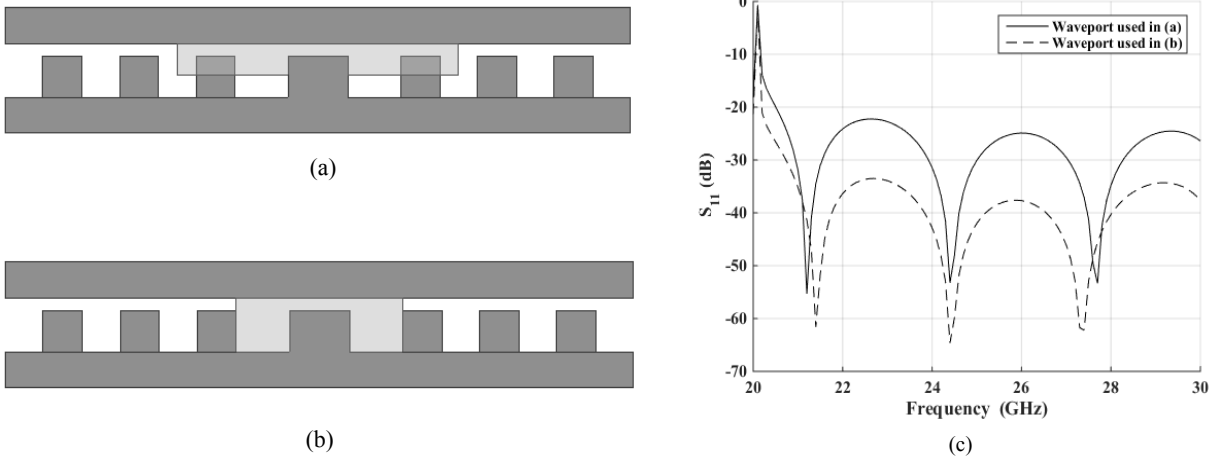


Fig. 3.3. (a) Wave port used in [52]. (b) Wave port used in [13]. (c) Comparison of S-parameters for 2 ports while feeding *RGWB* obtained using ANSYS.

In [127], several guidelines are considered while designing the structure to control the band of operation. The distance between the waveguide back wall, and the start of the rectangular coaxial,  $B$ , is recommended to be  $0.1\lambda$  to  $0.01\lambda$  according to the required capacitance. The distance between the back wall of the waveguide, and the ridge,  $D$ , is recommended to be  $0.25\lambda$  to control inductance since this groove acts as a short-circuited stub to equalize capacitive effects in order to enhance the matching. The width of the ridge,  $S$ , is recommended to be 0.25 to 0.33 of broad wall width, while the gap between the rectangular coaxial and the top wall  $H$  is chosen to provide a proper impedance matching with the  $50 \Omega$  coaxial line. In [128], the mode conversion is explained as a two-step process: Matching the low coaxial cable impedance with the high double ridge waveguide impedance, and conversion of the coaxial TEM mode to the TE mode of the double ridge waveguide. Such a step is performed by employing a mode converter between the coaxial cable, and the double ridge waveguide. A groove is added below the coaxial pin, and the rectangular coaxial part in order to allow the electric field intensity to increase between the upper ridge and the coaxial line, and decrease the field at the bottom.

The single, and double-sided S-parameters of the transition alone are obtained using ANSYS, then the simulation results are compared to the measurement of the back-to-back configuration of the transition, as shown in Fig. 3.5. The simulation, and measurements of the back-to-back configuration show return loss better than 15 dB from 11.5 GHz to 33 GHz. The simulated

insertion loss is 0.2 dB on average, and the measured one is 0.8 dB on average. The difference in insertion loss is attributed to connector losses.

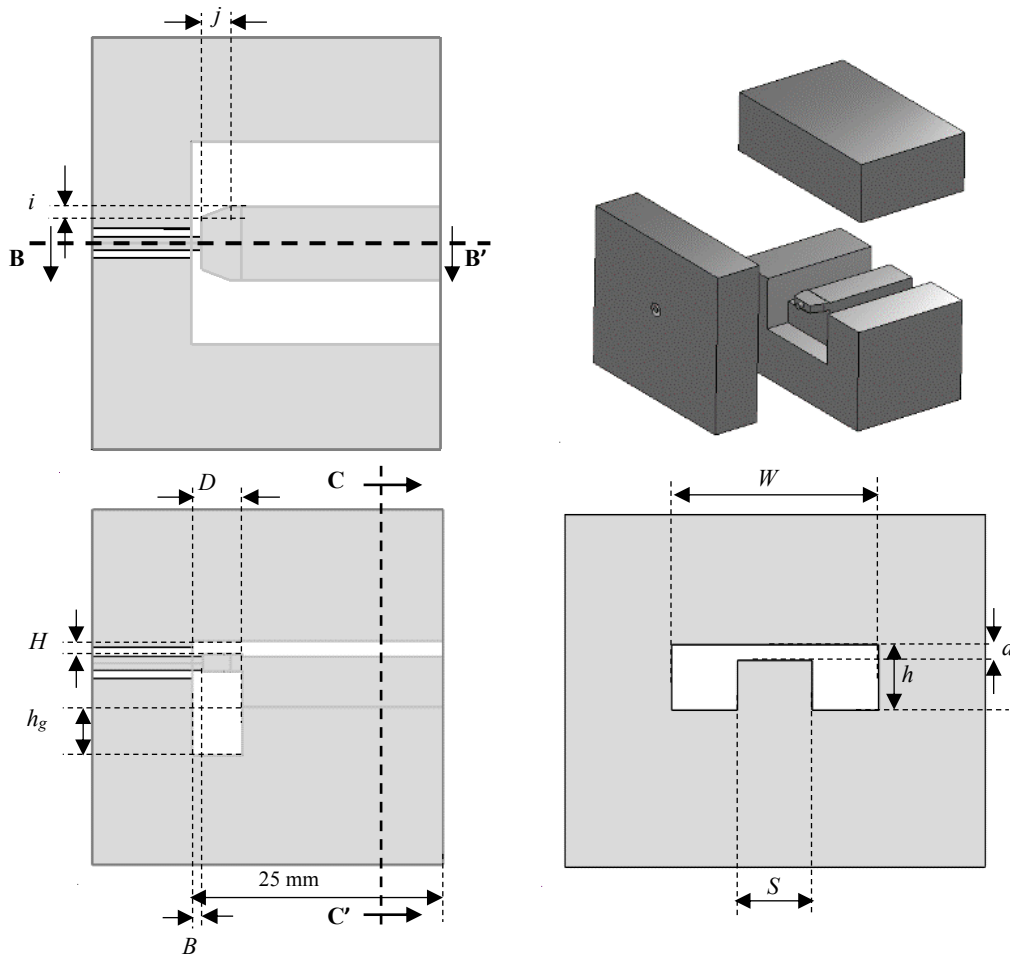


Fig. 3.4. Transition geometry with all parameters: Top view, side section BB', front section CC', and an exploded isometric view. In the isometric view, the grey arrows indicate the transition parts movement directions.

Table 3.3: Values of different parameters for the transition according to Fig. 3.4 notation.

Parameter	$W$	$S$	$h$	$d$	$D$	$B$	$H$	$h_g$	$i$	$j$
Value (mm)	9.7	3.5	3	0.7	2.5	0.5	0.6	2.2	0.5	1.4

Since the transition has a very wide bandwidth, two RGWs, of different cross-sections, may be used to test it. As a result, a fitting section will be used to match one RGW (*RGW A*) to the transition, while other RGW will be of the same cross-section as the transition. The geometry of

the fitting section, the single-sided S-parameters and the dimensions are shown in Fig. 3.6, Fig. 3.7, and Table 3.4, respectively.

The ability of the inline transition to feed the RGW is tested by simulation and measurement. The photo of the manufactured components along with the transition is shown in Fig. 3.8. The comparison of results is shown in Fig. 3.9. It is shown that feeding *RGW A* through a fitting section could achieve a return loss better than 15 dB in simulation (14 dB in measurement), and insertion loss around 1.1 dB in the measurement (0.4 dB in simulation) from 12 GHz to 25 GHz. Feeding *RGW B* directly with the transition demonstrates a simulated return loss better than 19 dB in the band from 20 to 30 GHz, while measurements show return loss better than 15 dB for the same band. The simulated insertion loss is 0.2 dB compared to 0.8 dB in measurement.

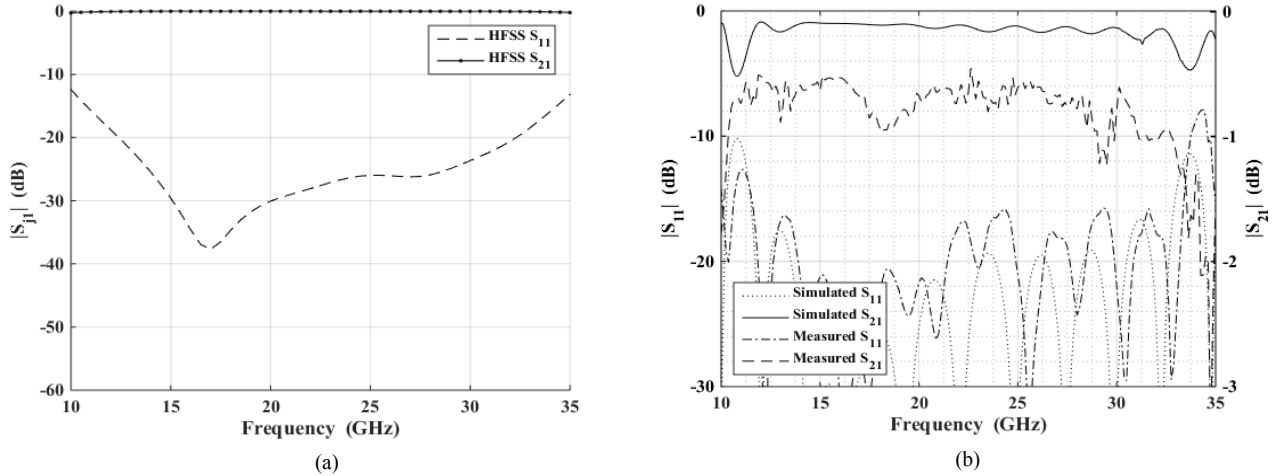


Fig. 3.5. (a) Single-sided S-parameters of the transition using ANSYS. (b) Comparison of S-parameters for back-to-back configuration of part 1 of the transition by measurement, and simulations.

Table 3.4: Values of different parameters for the fitting part according to Fig. 3.6 notation (next).

Parameter	$r_1$	$r_2$	$h_1$	$h_2$	$l_{start}$	$l_{stair}$	$l_b$	$l_{ex}$	$h_{stair}$
Value (mm)	2.3	3	3	4	2.2	1.4	6.4	23	0.1

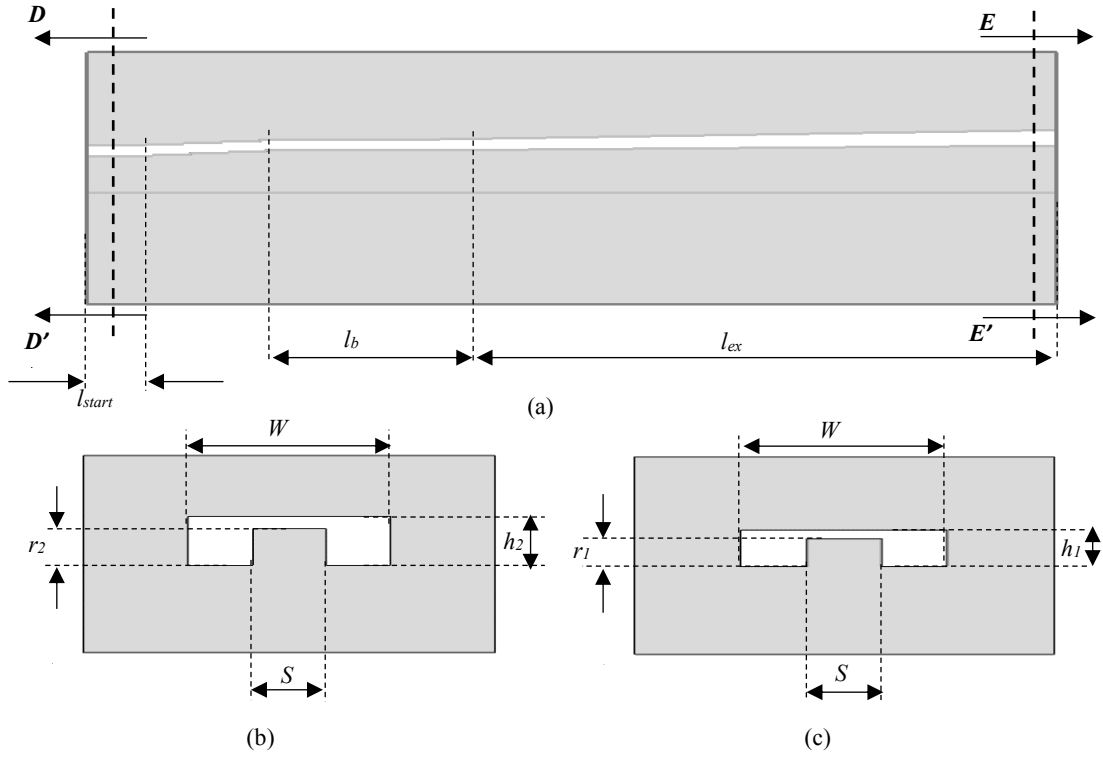


Fig. 3.6. Geometry of the fitting part with all parameters: (a) Side view. (b) Front section DD' matching transition dimensions. (c) Back section EE' that matches dimensions of *RGWA*.

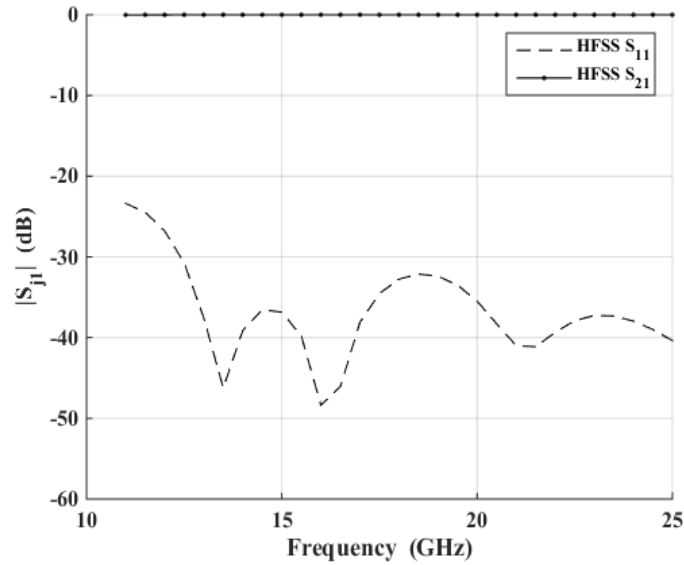


Fig. 3.7. Fitting part S-parameters (PEC) as obtained from ANSYS.

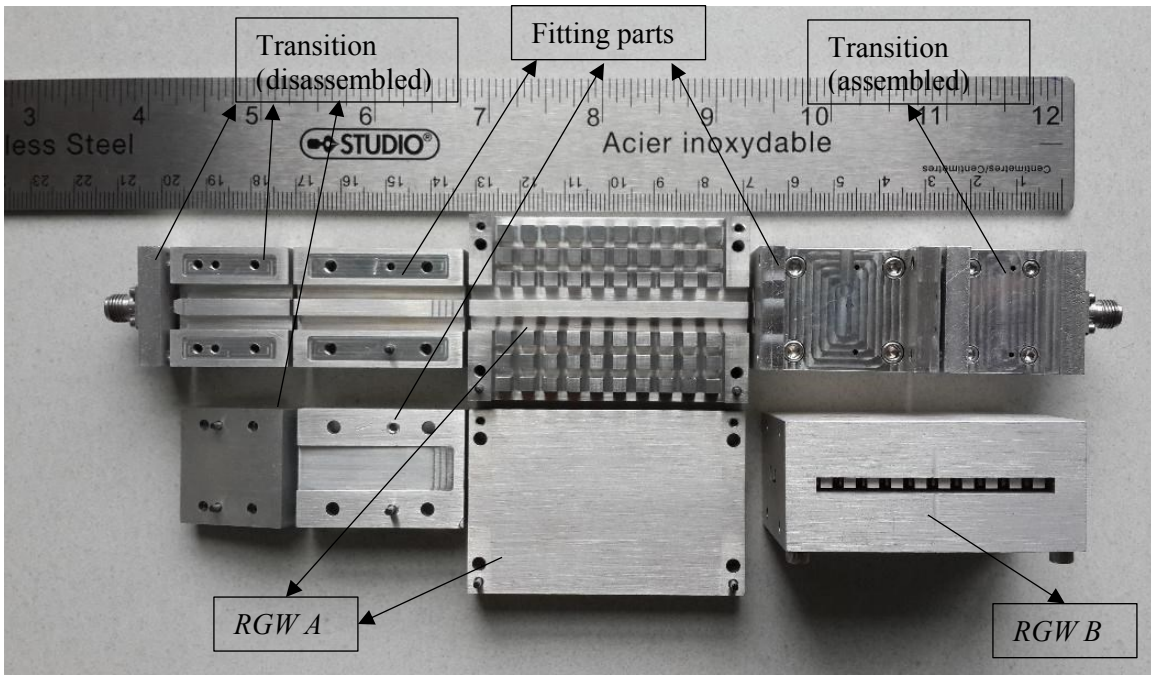


Fig. 3.8. Photo of the manufactured components for the inline transition.

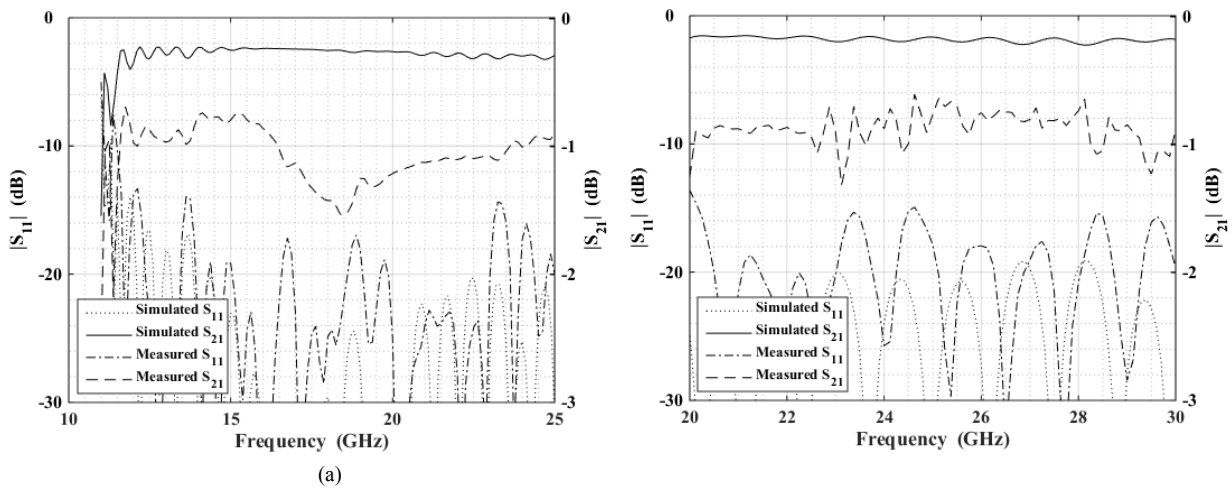


Fig. 3.9. (a) Comparison of S-parameters (measured VS simulated (ANSYS)) for transition feeding *RGW A*. (b) Comparison of the measured and simulated S-parameters for transition feeding *RGW B*.

Another part of the innovation in this transition is its tuning capability. By adding two screws in the groove below the coaxial pin, it is possible to tune the matching band of the transition to reach 40 GHz, which is the highest frequency available from the coaxial connector. Fig. 3.10 shows the first part of the transition after adding the two screws. The diameter of each screw is 0.889 mm,

and the distance between the axes of the screws is  $x_{sc}$ . Both screws have the same height  $h_{sc}$  whose value controls the matched band.

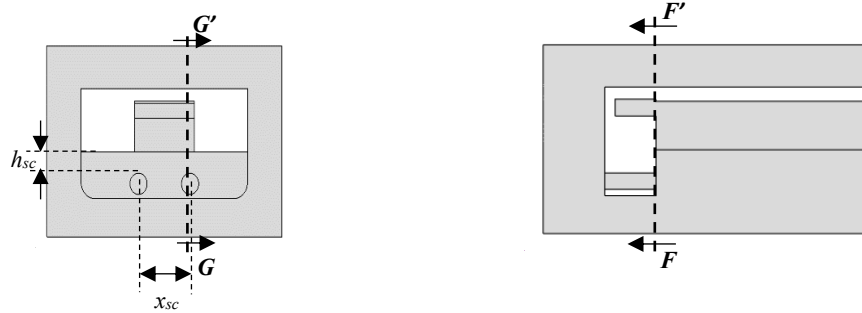


Fig. 3.10. Geometry of the first part of the transition showing the front section FF' and the side section GG' with two screws in the front section.

A parametric study is done to show the effect of the screws' height on the bandwidth of the transition. The results in Fig. 3.11 show that the matching band changes from (13 GHz to 38 GHz) to be (15 GHz to 41 GHz) when  $h_s$  changes from 1 mm to 0.25 mm.

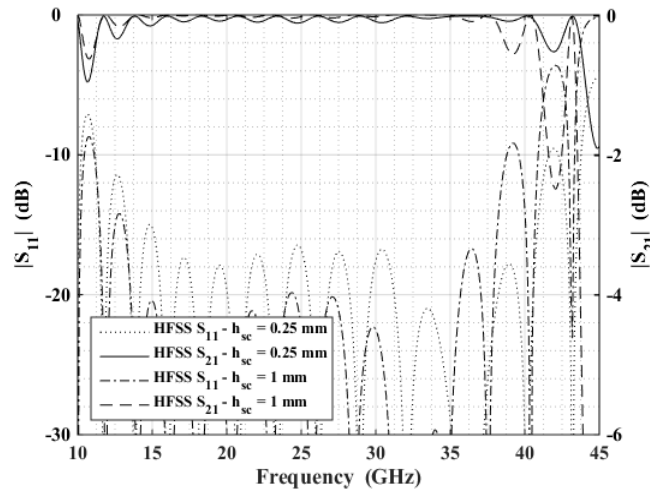


Fig. 3.11. Parametric study on the effect of the height of the screws on S-parameters of the transition.

### 3.3 Wideband Vertical Transition

In this section, the vertical transition used to feed all the microwave devices in this thesis is designed. This transition has the advantage of being convenient for feeding dual plane structures like Butler matrix proposed in this thesis since the coaxial feeding comes through the ridge.

### 3.3.1 Ridge gap waveguide design

The RGW used to test the transition is shown in Fig. 3.12, where a 5-section Chebyshev matching transformer is used to feed the RGW. The values of transformer parameters are shown in Table 3.5. As mentioned before, the RGW band is designed in two steps: Determining the stop band of the bed of nails using 2D-dispersion diagram and determining the unimodal band of the single row using 1D-dispersion diagram. Here, the RGW is designed to work from 13 GHz to 28.7 GHz by having the dimensions:  $a=3$  mm,  $p=5$  mm,  $s=3.5$  mm,  $c=3.1$  mm,  $h=3.3$  mm,  $r=2.2$  mm, and  $g=0.3$  mm following Fig. 1.6 notation. The 2D-dispersion diagram and 1D-dispersion diagram are both obtained using CST Microwave Studio and shown in Fig. 3.13. It is shown that the waveguide is working on the required band. The same port used in the inline transition is used here to feed the single ridge waveguide.

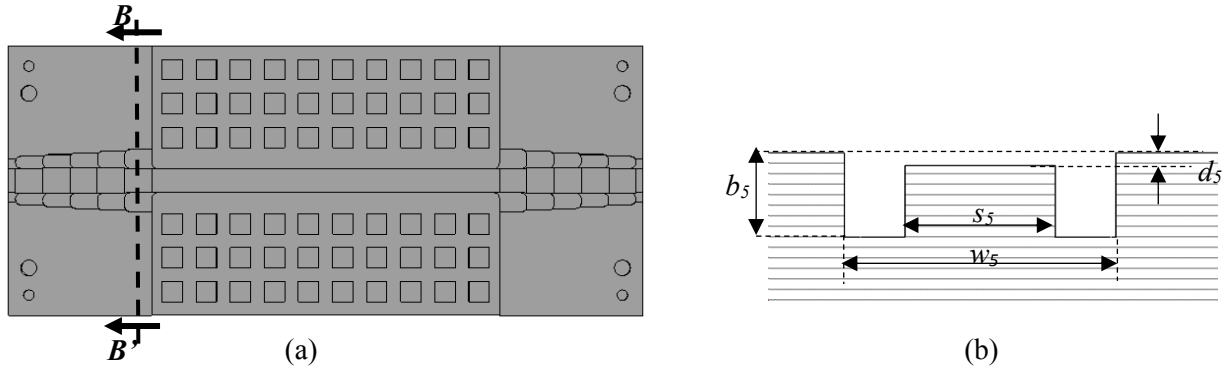


Fig. 3.12. RGW structure with 5-section Chebyshev matching transformer. (a) Top view. (b) Front cut at Section BB'.

Table 3.5: Values of the parameters of Chebyshev transformers in Fig. 3.12.

$i$	1	2	3	4	5
$w_i$ (mm)	7.2	7.7	8.2	8.7	9.2
$b_i$ (mm)	2.3	2.5	2.7	2.9	3.1
$s_i$ (mm)	3.6	3.7	3.7	5	3.55
$d_i$ (mm)	0.4	0.5	0.6	0.8	1

### 3.3.2 Vertical transition to the ridge gap waveguide

The transition geometry is shown in Fig. 3.14. A single ridge waveguide is fed by a 50- $\Omega$  coaxial transmission line through the ridge with a coaxial pin resting on the flat top cover of the transition.

The transition is designed to work on a wideband to feed reduced height ridge waveguides as well as RGW. In order to match the impedance of the waveguide to 50-Ω standard coaxial line, design equations for both coaxial line, and ridge waveguide impedances are utilized. The impedance of the coaxial transmission line is calculated using [10]:

$$Z_{\text{coaxial}} = \frac{60}{\sqrt{\epsilon_r}} \ln\left(\frac{r_{\text{out}}}{r_{\text{in}}}\right) \quad (3.1)$$

where  $\epsilon_r$  is the relative permittivity of the dielectric filling,  $r_{\text{out}}$  is the outer radius, and  $r_{\text{in}}$  is the inner radius of the coaxial cable. On the other hand, the ridge waveguide is a non-TEM line, and it doesn't have one definition for its impedance, as mentioned in [11]. One of the impedance definitions in a waveguide is the power-voltage definition:

$$Z_{pv}(f) = Z_{pv}(\infty) \left(\frac{\lambda_g}{\lambda_o}\right)$$

$$Z_{pv}(\infty) = \frac{\pi \eta_o \left(\frac{d}{\lambda_c}\right)}{X1 + X2} \quad (3.2)$$

$$X1 = \frac{4d}{\lambda_c} \ln\left(\text{cosec}\left(\frac{\pi d}{2b}\right)\right) \cos^2(\theta_2) + \frac{\theta_2}{2} + \frac{\sin(2\theta_2)}{4}, \quad X2 = \left(\frac{d}{b}\right) \left(\frac{\cos(\theta_2)}{\sin(\theta_1)}\right)^2 \left[\frac{\theta_1}{2} - \frac{\sin(2\theta_2)}{4}\right].$$

$$\theta_1 = \frac{\pi(w-s)}{\lambda_c}, \quad \theta_2 = \frac{\pi(s)}{\lambda_c}$$

Equation (3.2) states that the impedance of a ridge waveguide is maximum at the cutoff frequency of the guide, then decays fast to reach the stable value of  $Z_{pv}(\infty)$ . As a result, the coaxial impedance should match  $Z_{pv}(\infty)$ . The coaxial hole in the ridge is designed to be of conical shape (from  $r_1 = 0.43$  mm to  $r_6 = 0.31$  mm) which is realized using 5 radial steps of 0.02 mm each, and height of 0.5 mm except first, and last step ( $h_1=0.1$  mm, and  $h_6=0.1$  mm). All radial steps' radii, and heights are obtained by optimization in order to have impedance matching between the coaxial connector of pin radius  $r_0 = 0.19$  mm, and the reduced height ridge waveguide at the gap of the ridge waveguide.

The ridge waveguide is designed to have gap height  $d = 0.3$  mm, ridge width,  $s = 3.5$  mm, guide height  $b = 2$  mm, and guide width  $w=6.4$  mm such that the single ridge impedance at infinity

according to (3.2) will equal  $28.7 \Omega$ . In order to match this impedance with the coaxial line, the outer radius of the coaxial line at the top of the ridge is set to  $r_6 = 0.31 \text{ mm}$  so that the coaxial line impedance is approximately equal to  $29.37 \Omega$ .

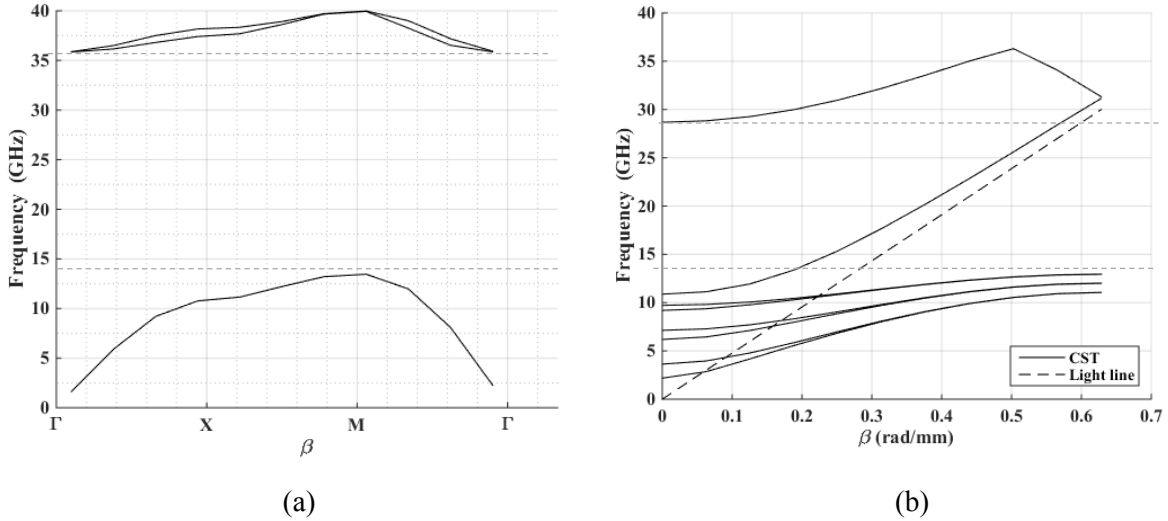


Fig. 3.13. The dispersion diagrams obtained from eigenmode analyses using CST Microwave studio. (a) 2D-dispersion diagram of a unit cell. (b) 1D-dispersion diagram of one row.

The coaxial pin has a rectangular waveguide acting as a wideband back short from one side, and a single ridge waveguide from the other side, where the lower dominant mode cutoff of the single ridge waveguide has been used to implement a wideband back short of length  $LB = 4 \text{ mm}$  in the transition. The capacitance between the sidewalls and the ridge is reduced by tapering the connection between the coaxial outer conductor, and the ridge as in [72]. The single-sided transition is simulated using ANSYS, and results are shown in Fig. 3.15(a). It shows that the transition is matched from 12.8 GHz to 42 GHz with a return loss better than 20 dB over the entire band. The transition has been manufactured and measured in a back-to-back configuration.

Fig 3.15(b) shows a comparison between the simulated and measured results for the double-sided transition, where both the measured and simulated return loss are better than 14 dB from 12.8 to 41 GHz. This transition can be used to feed RGW or single ridge waveguide directly and can be used to feed a double ridge waveguide by adding a matching section. However, it might be advantageous to feed a double ridge waveguide without the matching section. The same concept of impedance match has been used to create a coaxial-to-double ridged waveguide transition in order to eliminate the need for the matching section.

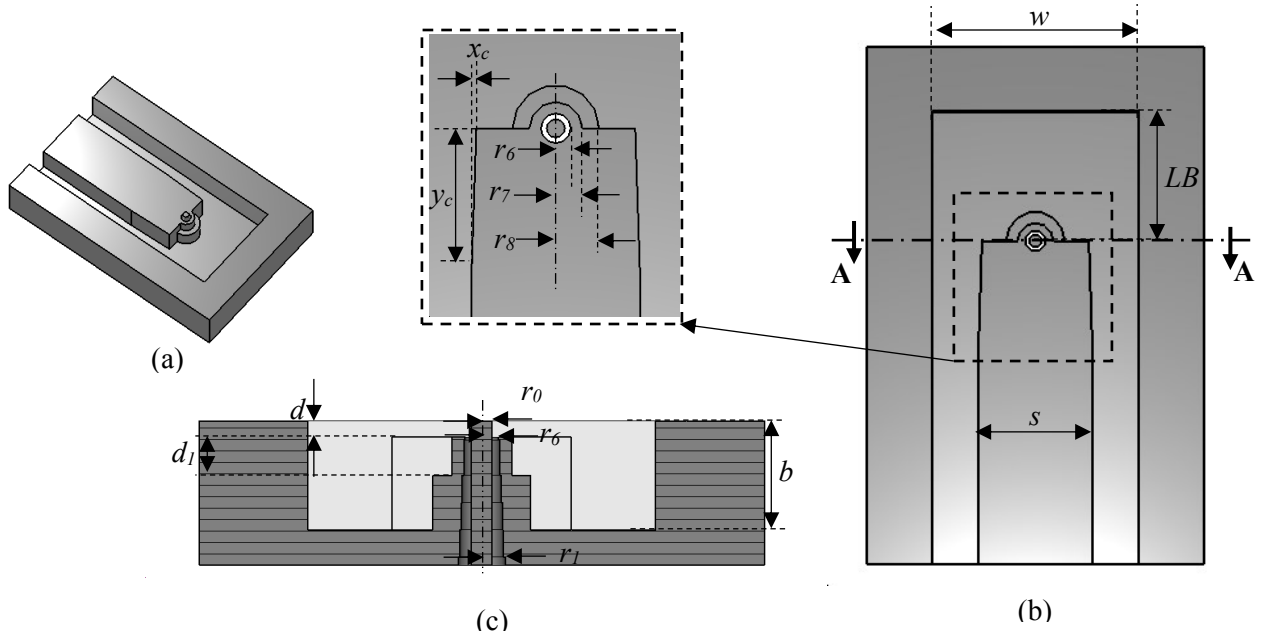


Fig. 3.14. Transition structure after removing the cover plate. (a) Isometric. (b) Top view with inset. (c) Front cut AA' through the connector.

The suggested shape of the double ridged transition is shown in Fig. 3.16, where the upper plate in Fig. 3.14 is replaced with a ridged section of ridge height  $r_u$ . The asymmetric double ridge waveguides have been addressed by a few papers in the literature, unlike the standard double ridge waveguide and single ridge waveguide. In [129], an integral eigenvalue equation is solved numerically using a Ritz-Galerkin method, and solution results are used to obtain the characteristic impedance and the cutoff space of the asymmetric double ridge waveguide. In [130], the dominant mode cutoff frequency is obtained by employing the equivalent single ridge waveguide parameters that are obtained numerically by trial and error, then plotted on a design curve while the characteristic impedance is not calculated.

The methods used in [129] and [130] lack physical insight. In [130], the reason behind dividing the asymmetric double ridge waveguide into two single ridge waveguides is not clear. In addition, trial and error are needed to reach the required cutoff. Also, in [129], a computational approach is followed to obtain the characteristic impedance and cutoff space. In both cases, design tables and curves are provided, which limits the applicability of asymmetric ridge waveguides.

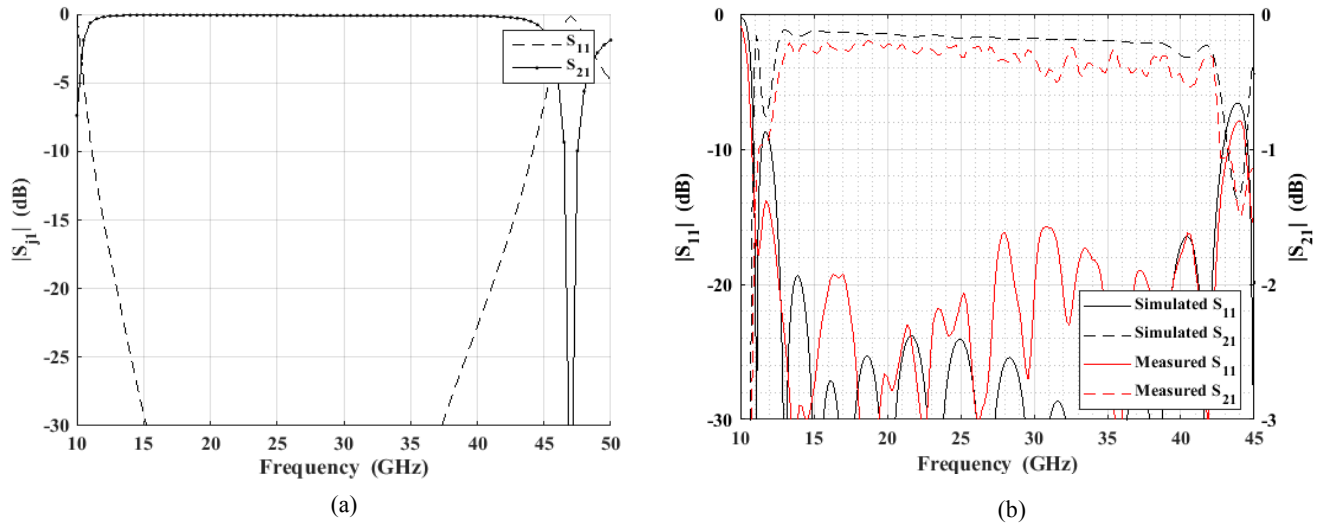


Fig. 3.15. S-parameters of the vertical transition. (a) Single-sided S-parameters. (b) Comparison of the simulated double-sided S-parameters (ANSYS) of the transition with the measurement.

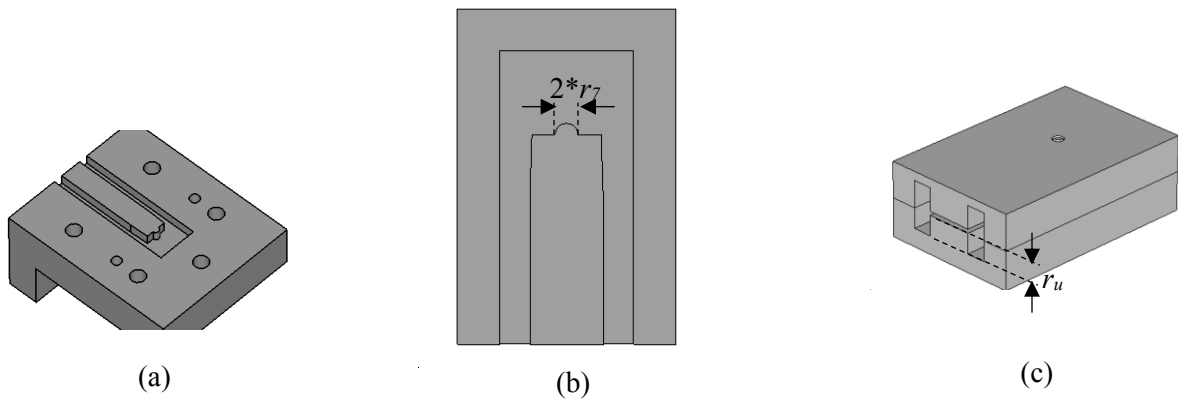


Fig. 3.16. ADR transition design with the parameters shown. (a) Isometric view of the top part. (b) Top view of the top part. (c) ADR transition upside down.

Several design equations are developed for the conventional ridge waveguides in several publications [131], [132], and [133]. Similar formulas will be useful if developed for the asymmetric double ridge waveguide. The derivation of the characteristic impedances of asymmetric double ridge waveguide is presented in [134]. Here, the obtained power-voltage definition of the asymmetric double ridge waveguide is used to design the asymmetric double ridge waveguide impedance to match the coaxial connector impedance. The asymmetric double ridge waveguide transition is designed, fabricated, and measured. Fig. 3.17 shows a comparison of the simulated and measured S-parameters, and they are in good agreement.

The ability of the single ridge waveguide transition to feed the RGW is tested by measurement. A photo of the manufactured components is shown in Fig. 3.18. The comparison between the measured and simulated results is shown in Fig. 3.19, where the return losses are shown to be in good agreement (both under 13 dB on the whole band). The simulated insertion loss is 0.4 dB on average, which goes to 0.8 dB on average in the measurement. The decrease in the insertion loss level is due to the non-perfect contact between the waveguide and the transition and due to the connector losses.

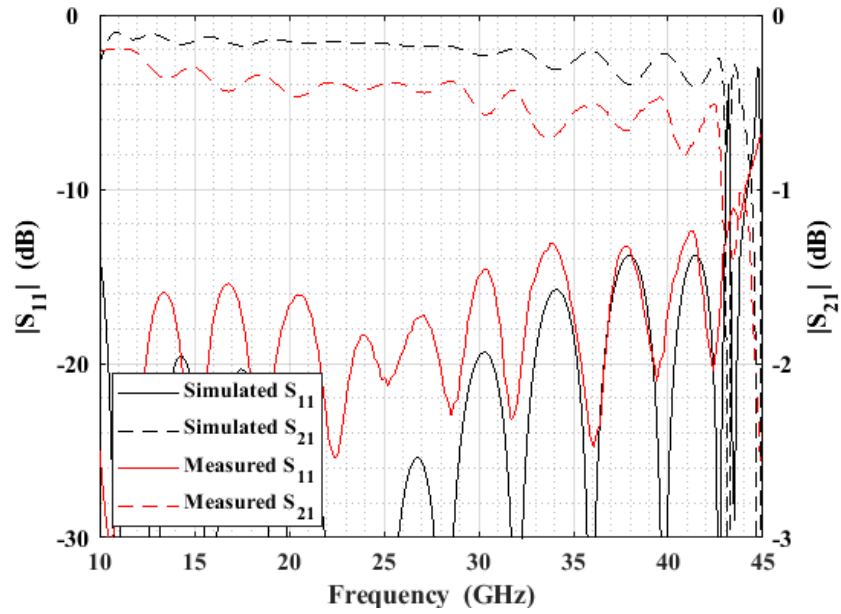


Fig. 3.17. Comparison of the measured and simulated (ANSYS) S-parameters for back-to-back configuration of the asymmetric double ridge transition.

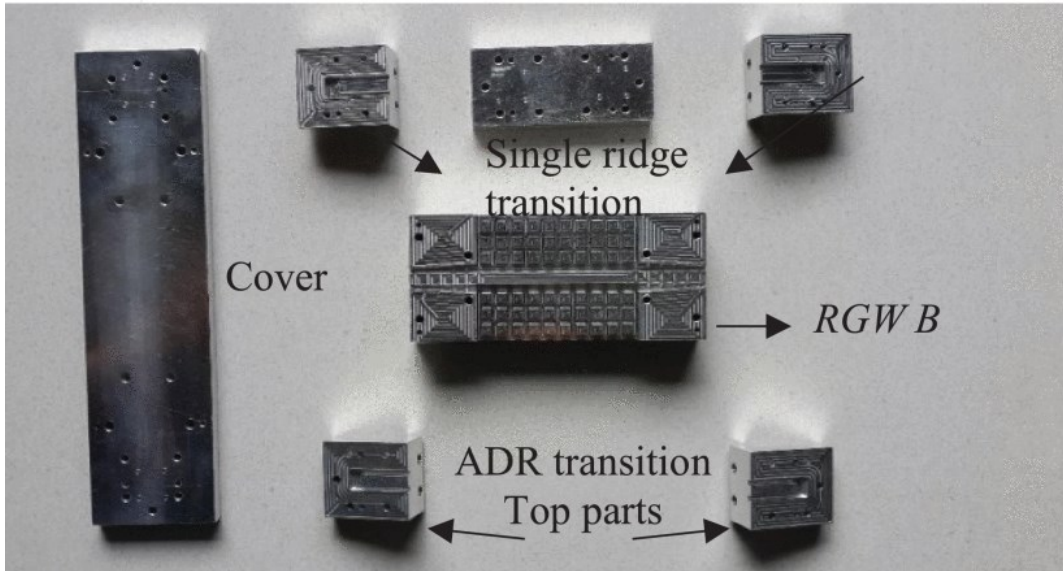


Fig. 3.18. A photo of the manufactured components.

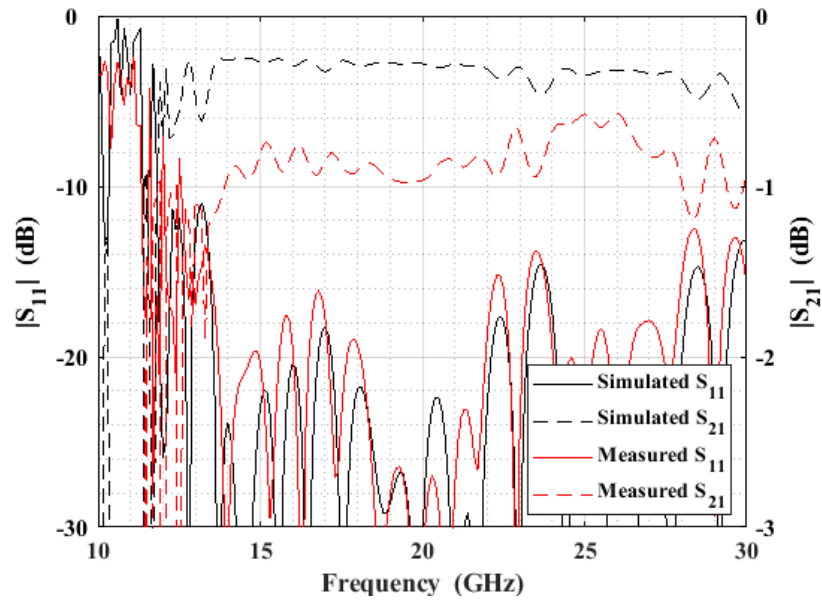


Fig. 3.19. Comparison of the measured and simulated (ANSYS) S-parameters for the single ridge transition feeding *RGWB* in back-to-back configuration.

# Chapter 4

## Wideband Single Ridge and RGW Power Splitters

### 4.1 Introduction

In this chapter, a ridge waveguide splitter of more than 100% bandwidth is designed using the concept of the zero- $E_t$  plane. After that, an important property of the RGW, which is the existence of zero field region physically connected to the region containing the field, is used to create a novel wideband power splitter working on 40% to cover the whole Ka-band. The tuning mechanism may be integrated into the zero field region in order to avoid any disturbance of the electric field. It is worth mentioning that a real-time tunable waveguide power splitter is usually implemented using several cascaded devices and not using one single device as shown here. More data will be available in Section 4.3.

### 4.2 Analysis of Asymmetric Double Ridge Waveguide

The double ridge waveguide shown in Fig. 4.1 (a) can be understood as two single ridge waveguides on the top of each other with the intermediate sheet removed, which indicates the existence of a horizontal zero tangential electric field plane (zero- $E_t$  plane) in the middle of double ridge waveguide. This may be deduced from the  $TE$  nature of the dominant mode in double ridge waveguide, and the symmetry of the guide around the zero-tangential-electric-field plane. This can also be deduced from the Finite Element Method  $FEM$  analysis in [11], which uses an electric wall at the position of this plane for the discretization of the domain to solve the double ridge waveguide. The single ridge waveguide in Fig. 4.1(b) may be regarded as a double ridge waveguide whose upper ridge height equals zero, and whose zero- $E_t$  plane is tangential to the upper guide plate. This zero- $E_t$  plane is sought to exist if the nonzero upper and lower guide heights are not equal (as in Fig. 4.1 (c)), which is the Asymmetric Double Ridge (ADR) waveguide for which the plane position is unknown. If the plane position is known, the power flowing in the ADR waveguide can be split into two portions by placing a metallic sheet in the position of the zero- $E_t$  plane shown dotted in Fig. 4.1 (a, c). This may be used to design a wideband power splitter.

In order to know the position of the zero- $E_t$  plane for the Asymmetric Double Ridge (ADR) waveguide in Fig. 4.1 (c), the guide is assumed to be consisting of two single ridge waveguides. The cutoff wavelength of the asymmetric double ridge waveguide decides the frequency at which the power starts flowing in the guide cross-section, so it is supposed to equal the cutoff frequency of the two single ridge waveguides. The position of the sheet will be obtained by using the equation from [11]:

$$\lambda_c = 2(w - s) \sqrt{1 + \frac{4}{\pi} \left( 1 + 0.2 \sqrt{\frac{b}{w - s}} \right) \left( \frac{b}{w - s} \right) \ln \left( \operatorname{cosec} \left( \frac{\pi d}{2b} \right) \right) + \left( 2.45 + 0.2 \frac{s}{w} \right) \left( \frac{sb}{d(w - s)} \right)}$$

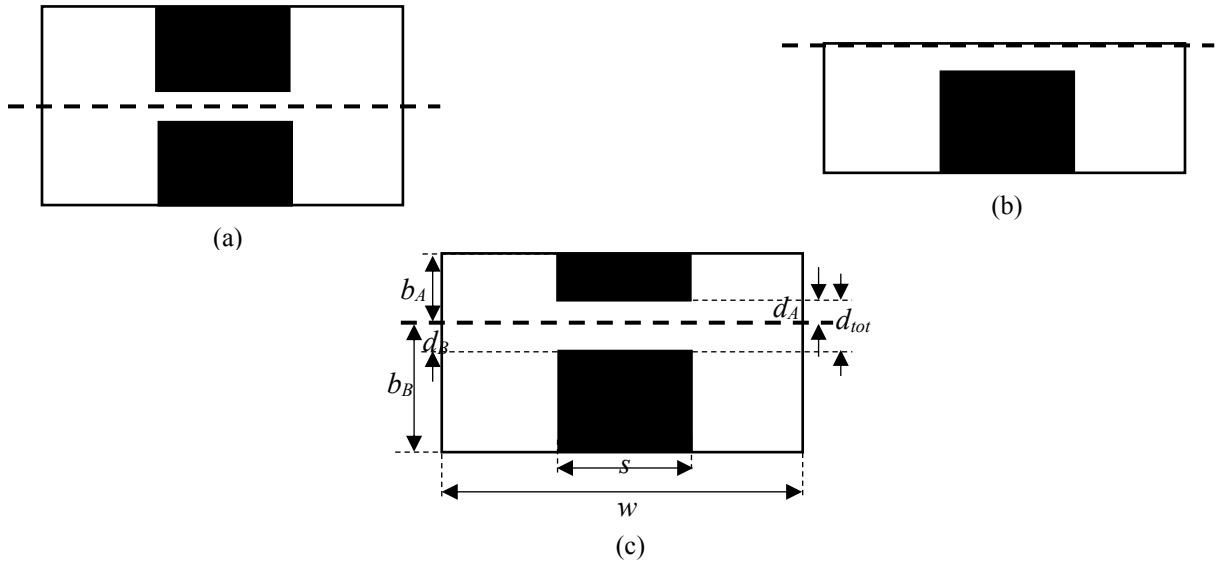


Fig. 4.1. Illustration of the reasoning behind the existence of zero tangential electric field plane (thick dashes) in ridge waveguide. (a) Double ridge waveguide. (b) Single ridge waveguide. (c) Asymmetric double ridge waveguide.

If the two cutoff wavelengths of the single ridge guides are equal:

$$\lambda_{cA} = \lambda_{cB}$$

$$\begin{aligned} & \frac{4}{\pi} \left( 1 + 0.2 \sqrt{\frac{b_A}{w - s}} \right) \left( \frac{b_A}{w - s} \right) \ln \left( \operatorname{cosec} \left( \frac{\pi d_A}{2b_A} \right) \right) + \left( 2.45 + 0.2 \frac{s}{w} \right) \left( \frac{s b_A}{d_A (w - s)} \right) \\ & = \frac{4}{\pi} \left( 1 + 0.2 \sqrt{\frac{b_B}{w - s}} \right) \left( \frac{b_B}{w - s} \right) \ln \left( \operatorname{cosec} \left( \frac{\pi d_B}{2b_B} \right) \right) + \left( 2.45 + 0.2 \frac{s}{w} \right) \left( \frac{s b_B}{d_B (w - s)} \right) \end{aligned}$$

(4.1)

which is one equation in 4 unknowns:  $b_A$ ,  $b_B$ ,  $d_A$ , and  $d_B$ . Other 3 equations are:

$$b_A + b_B = b_{tot} \quad (4.2)$$

$$d_A + d_B = d_{tot} \quad (4.3)$$

$$b_A - d_A = r_A \quad (4.4)$$

where  $r_A$  is the upper ridge height. By solving these equations together, the plane position is obtained.

It is worth mentioning that [130] can predict the cutoff frequency of the ADR waveguide; however, the physical explanation for the need to split the ADR guide into two single ridge waveguides (which is the existence of this zero- $E_t$  plane) is not mentioned. Instead, a trial and error procedure is used to determine the ADR guide cutoff.

One approximation adopted in [96] is to assume:

$$\frac{d_A}{b_A} = \frac{d_B}{b_B}$$

which means

$$b_A = \frac{b r_A}{r_A + r_B} \quad (4.5)$$

A comparison between the position of the zero- $E_t$  plane determined by  $b_A$  obtained by solving the 4 equations, and that obtained using the approximation is shown in Fig. 4.2 for  $b_{tot} = 6$  mm,  $w = 9.7$  mm, and  $s = 3.5$  mm while varying upper ridge height  $r_A$  from 0.2 mm to 2.2 mm, and varying upper ridge height  $r_B$  from 1 mm to 3 mm. It appears that the approximation is acceptable to calculate the plane in all the cases shown.

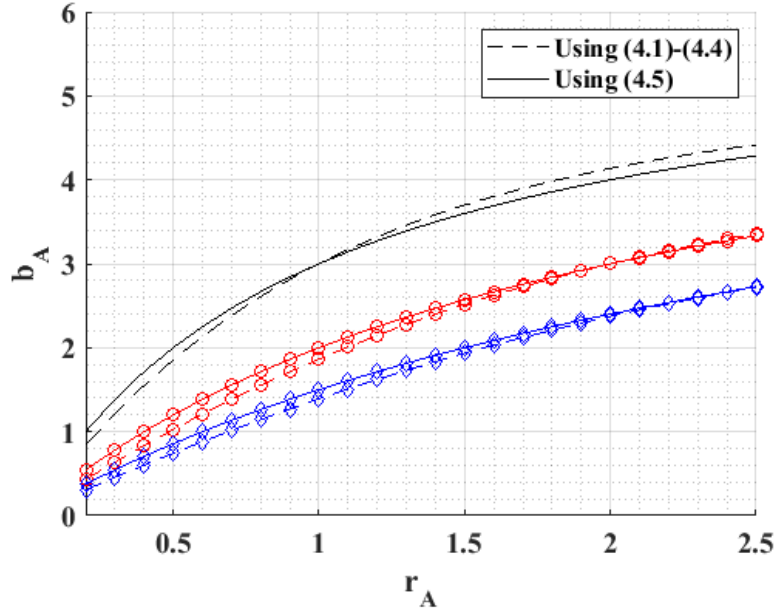


Fig. 4.2. A comparison between the approximate and accurate solutions obtained for the position of the Zero- $E_t$  plane versus upper ridge heights  $r_A$  for different lower ridges' heights of  $r_B = 1$  mm (black lines),  $r_B = 2$  mm (red circle),  $r_B = 3$  mm (blue diamond).

## 4.3 Wideband Ridge Waveguide Splitter

As mentioned, a double ridge waveguide of symmetric/asymmetric ridge heights has a horizontal zero- $E_t$  plane, where no tangential electric field exists. As a result, it is possible to split the guide into two single ridge waveguides using a metallic sheet without any perturbation for the electric fields. Also, since the position of the plane doesn't depend on the frequency of operation, it is expected to get a flat, and stable coupling level on a wide bandwidth.

### 4.3.1 Design of unequal power splitter

The proposed structure is shown in Fig. 4.3. The dimensions of the double ridge waveguide used are shown in Table 4.1, where  $r_B = 2.3$  mm and  $s = 3.5$  mm for all the cases. The sheet position depends on the ratio between upper and lower ridge heights, as in [96]. Two steps,  $k_A$  and  $k_B$ , are made in the ridges to account for the sheet non-zero thickness  $t$  so that the guide impedances are adjusted for better matching. The values of  $k_A$  and  $k_B$  are chosen by approximation such that:

$$\frac{k_A}{k_B} = \frac{b_A}{b_B} = \frac{d_A}{d_B} = \frac{r_A}{r_B}$$

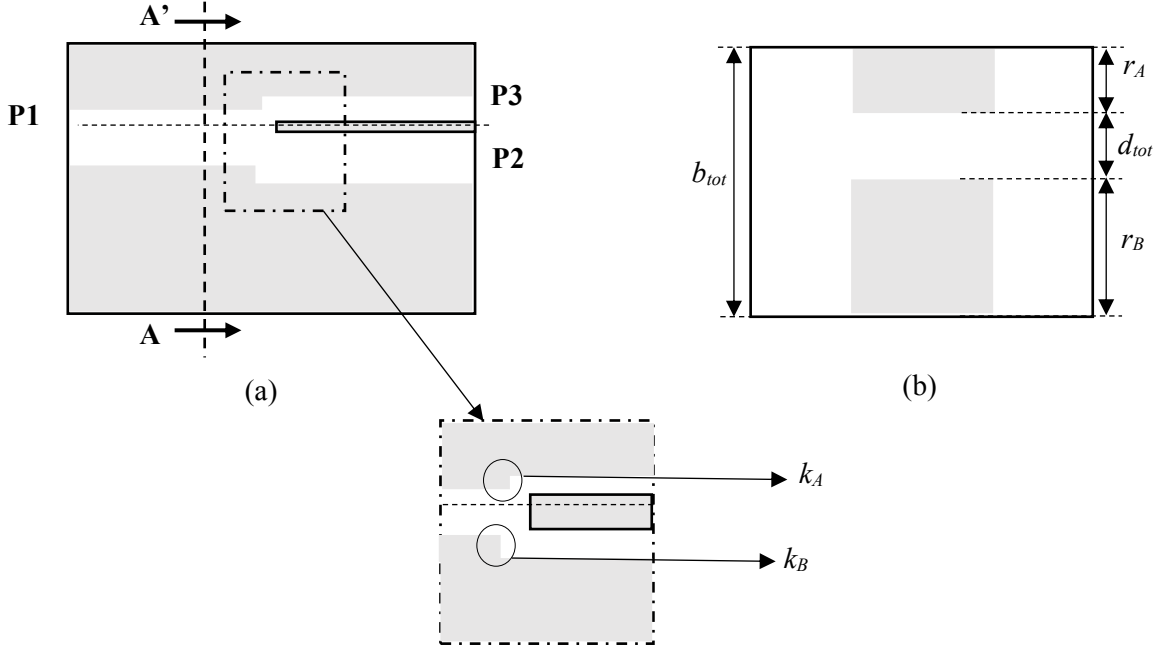


Fig. 4.3: Splitter structure using double/single ridge waveguides. (a) Side view of the splitter with 3 ports  $P1$ ,  $P2$  and  $P3$  and inset showing steps  $k_A$  and  $k_B$ . (b) Front view at Section  $AA'$ .

The exact estimation of the power division ratio of the splitter may be obtained from the expression of power flow in single ridge waveguide [11]:

$$P_{SR}(\infty) = \left( \frac{E_o^2 d \lambda_c}{2\pi\eta_o} \right) \left\{ \left( \frac{4d}{\lambda_c} \right) \ln \left( \operatorname{cosec} \left( \frac{\pi d}{2b} \right) \right) (\cos \theta_2)^2 + 0.5 \theta_2 + 0.25 \sin(2\theta_2) + \left( \frac{d}{b} \right) \left( \frac{\cos \theta_2}{\sin \theta_1} \right)^2 [0.5 \theta_1 - 0.25 \sin(2\theta_1)] \right\}$$

where  $E_o$  is the peak electric field at the center of the guide,  $\theta_1 = \pi(a - s)/\lambda_c$ , and  $\theta_2 = \pi s/\lambda_c$ . This gives the power division ratio expression:

$$\frac{P_A}{P_B} = \frac{d_A \left\{ \left( \frac{4d_A}{\lambda_c} \right) \ln \left( \operatorname{cosec} \left( \frac{\pi d_A}{2b_A} \right) \right) (\cos \theta_2)^2 + 0.5 \theta_2 + 0.25 \sin(2\theta_2) + \left( \frac{d_A}{b_A} \right) \left( \frac{\cos \theta_2}{\sin \theta_1} \right)^2 [0.5 \theta_1 - 0.25 \sin(2\theta_1)] \right\}}{d_B \left\{ \left( \frac{4d_B}{\lambda_c} \right) \ln \left( \operatorname{cosec} \left( \frac{\pi d_B}{2b_B} \right) \right) (\cos \theta_2)^2 + 0.5 \theta_2 + 0.25 \sin(2\theta_2) + \left( \frac{d_B}{b_B} \right) \left( \frac{\cos \theta_2}{\sin \theta_1} \right)^2 [0.5 \theta_1 - 0.25 \sin(2\theta_1)] \right\}} \quad (4.6)$$

where  $d_A$ ,  $d_B$ ,  $b_A$ , and  $b_B$  may be obtained using the approximate or exact method. Here, values are obtained initially by the approximate method then tuned in CST. The final dimensions of the splitters are shown in Table 4.1.

Table 4.1: Values of different parameters for 3 different cases of the splitter as shown in Fig. 4.3 (Sheet thickness=0.5 mm)

	Case A	Case B	Case C
$w$ (mm)	7.4	9	9
$s$ (mm)	3.5	3.5	3.5
$b_{tot}$ (mm)	6	4.2	3.5
$d_{tot}$ (mm)	1.4	1.2	1
$r_A$ (mm)	2.3	0.75	0.25
$d_A$ (mm)	0.7	0.3	0.1
$k_A$ (mm)	0.25	0.125	0.05
$k_B$ (mm)	0.25	0.375	0.45
$P_A/P_{tot}$ (dB)	-3	-6	-10

### 4.3.2 Results

In order to measure the performance of each splitter in Table 4.1, the 3 ports of each splitter have to be matched to the port of the vertical transition designed in Section 3.3. Fig. 4.4 shows the construction of the manufactured 6-dB splitter, where the 5<sup>th</sup> order Chebyshev transformer is used to match the splitter ports to the transition over a wideband. The values of different parameters for the 6 dB and 10 dB splitters are listed in Tables 4.2 and 4.3, respectively. The splitters are manufactured using CNC machining and measured using a vector network analyzer. A photo of the manufactured splitters is shown in Fig. 4.5. The measured and simulated results of the 3 splitters are shown in Fig. 4.6. The comparison shows good agreement for the S-parameters at the two output ports, while the measured and simulated return losses are below 10 dB for all the cases except for 6 dB case where the measurement is better than 8 dB around 35 GHz. Some discrepancies in the phase are attributed to the absence of a calibration kit for the double ridge waveguide port and to the measurement errors.

On the other hand, power splitting ratios of 10 dB or more may be reached using the proposed power splitter on the cost of the reduced gap height in the lower power single ridge waveguide arm, which makes the splitter performance hard to measure using 50  $\Omega$  transitions. That's where

the vertical transition in Chapter 3 may be used since its gap height is 0.3 mm, and its power voltage impedance  $Z_{PV}$  is  $29 \Omega$ ; hence, closer to the expected impedance and gap heights of the reduced height ridge waveguide. One solution to the reduced gap height of the low power arm is to increase the gap height in the higher power arm of the splitter on the cost of the splitter total bandwidth. A parametric study is carried out to determine the effect of larger gaps on the bandwidth of the splitter in case of high power splitting ratio (10 dB). The parametric study is shown in Table 4.2, where the bandwidth of different splitters are shown with the gap heights of lower power arm ( $d_A$ ) and the achieved approximate power split ratio for each case. The constant parameters in this study are  $s = b_{tot}=3.5$  mm, and  $w=9$  mm. The splitters' bandwidths in Table 4.4 are obtained using CST Microwave Studio's eigenmode simulation by taking the common band for the 3 ports of the splitter.

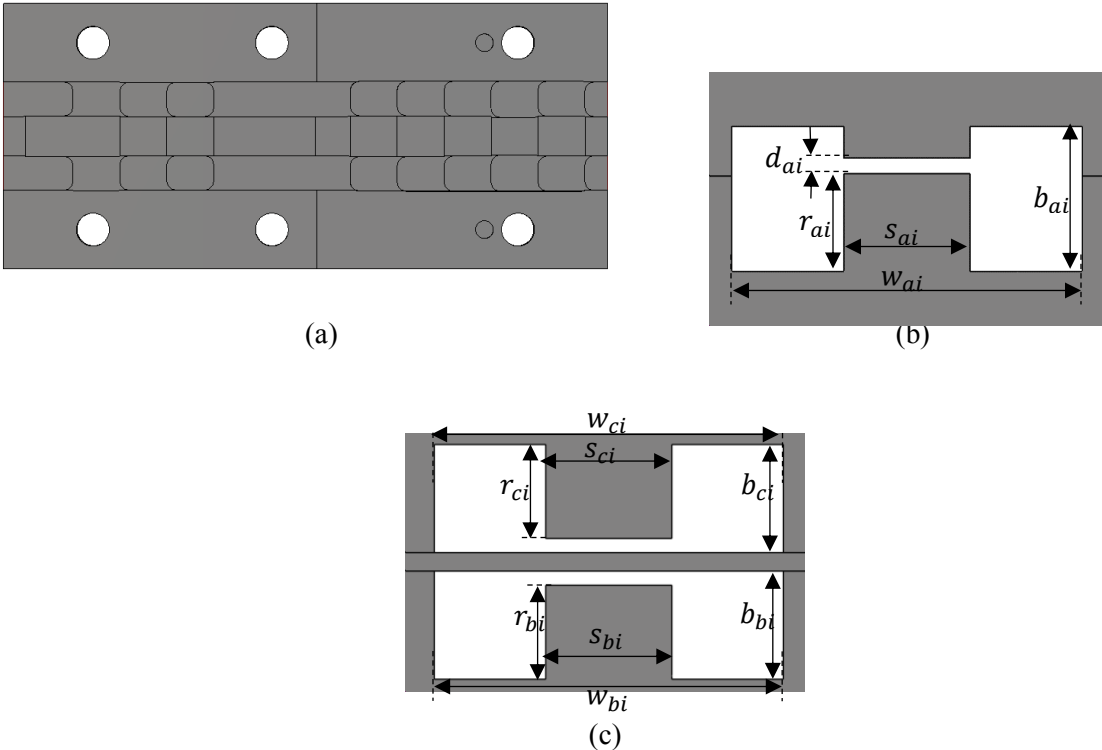


Fig. 4.4. Final design of the 6-dB splitter. (a) Top view of upper half with transformer stages numbered. (b) Front section BB'. (c) Front section CC'.

A parametric study is done on the effect of the sheet thickness  $t$  on the obtained results. The result of this study is shown in Fig. 4.7, where the return loss is better than 25 dB in all the cases, and the splitting ratio doesn't depend on the sheet thickness.

Table 4.2: Values of different parameters of 6-dB splitter following Fig. 4.4 notation (all in mm)

$i$	1	2	3	4	5
$w_{ai}$	6.8	7.2	7.8	8.2	8.6
$s_{ai}$	3.5	3.7	3.4	3.6	3.6
$b_{ai}$	3.65	3.65	3.75	4.05	4.05
$r_{ai}$	1.8	2	1.9	2.1	2.2
$d_{ai}$	0.35	0.45	0.6	0.85	1.01
$w_{(b/c)i}$	8.6/8.6	8.2/8.2	7.8/7.8	7.2/7.2	6.8/6.8
$s_{(b/c)i}$	3.5/3.5	3.4/3.5	3.3/3.5	3.5/3.5	3.7/3.5
$b_{(b/c)i}$	2.6/1.1	2.5/1.4	2.4/1.6	2.2/1.8	2.2/2
$r_{(b/c)i}$	1.75/0.8	1.8/1.1	1.9/1.3	1.8/1.5	1.8/1.7

Table 4.3: Values of different parameters of 10-dB splitter following Fig. 4.4 notation (all in mm)

$i$	1	2	3	4	5
$w_{ai}$	6.8	7.2	7.6	8.2	8.6
$s_{ai}$	3.5	3.5	3.6	3.5	3.5
$b_{ai}$	2.3	2.5	2.7	2.9	3.2
$r_{ai}$	1.7	1.75	1.8	1.75	1.8
$d_{ai}$	0.35	0.45	0.65	0.95	1.25
$w_{(b/c)i}$	8.6/8.7	8/7.6	7.5/8	7.2/7.6	6.8/6.7
$s_{(b/c)i}$	3.3/3.1	3.4/3.3	3.6/3.4	3.6/3.6	3.6/3.1
$b_{(b/c)i}$	2.6/0.35	2.6/0.6	2.45/0.9	2.1/1.5	2.05/1.6
$r_{(b/c)i}$	1.45/0.2	1.7/0.45	1.8/0.7	1.65/1.25	1.7/1.35

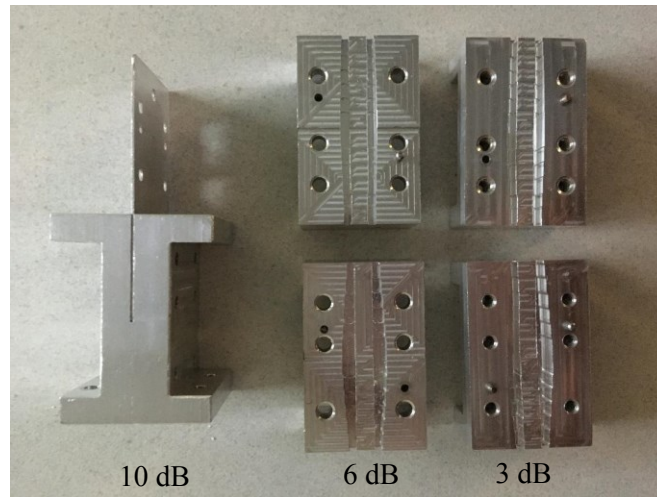
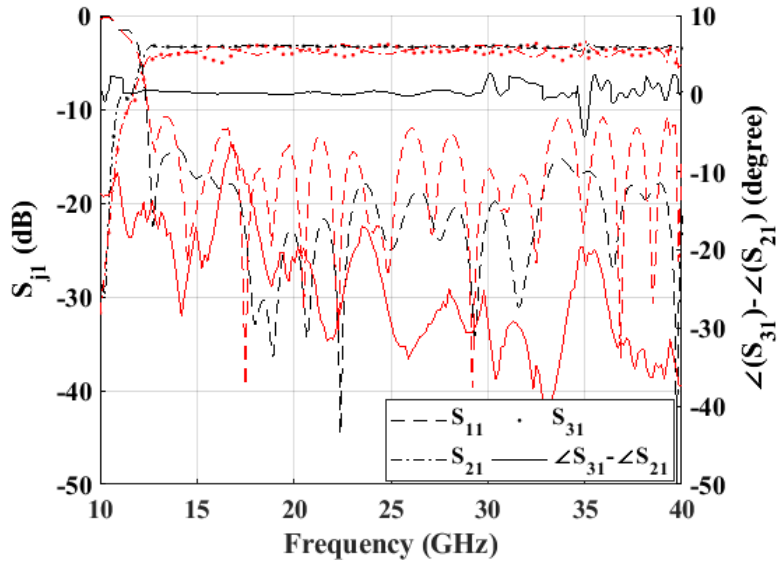
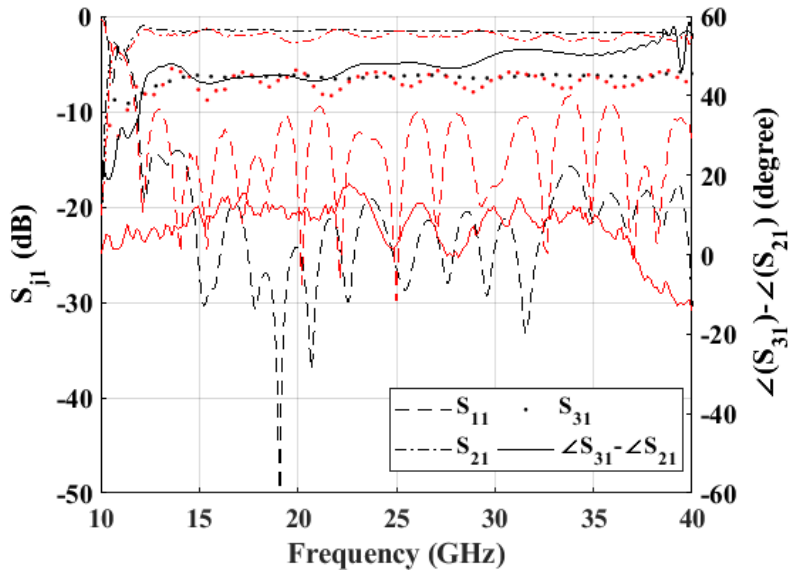


Fig. 4.5. A photo of the manufactured splitters.

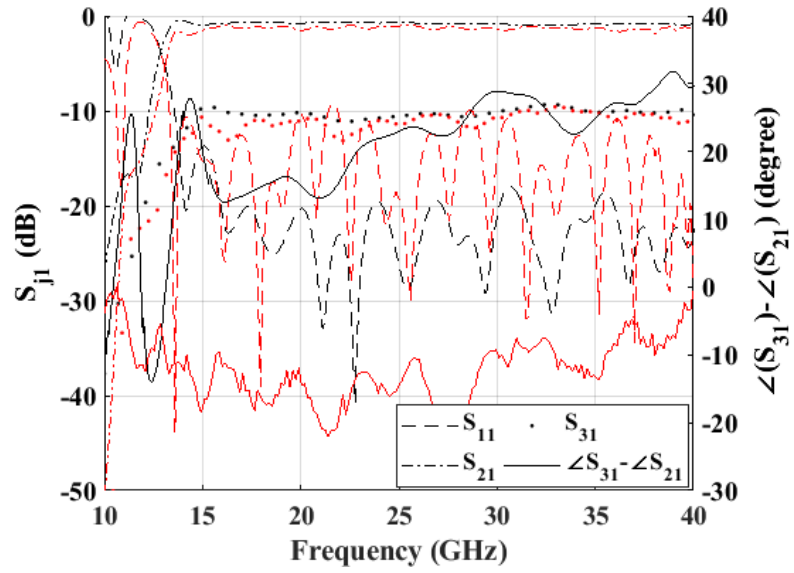


(a)



(b)

Fig. 4.6 (a). Simulated (black) and measured (red) S-parameters of the 3-dB power splitter. (b) Simulated (black) and measured (red) S-parameters of the 6-dB power splitter.



(c)

Fig. 4.6 (c) Simulated (black) and measured (red) S-parameters of the 10-dB power splitter.

Table 4.4: Parametric study on the effect of increased gap height on the bandwidth of the wideband splitter.

	Case D	Case E	Case F
$w$ (mm)	9	9	9
$s$ (mm)	3.5	3.5	3.5
$b_{tot}$ (mm)	3.5	3.5	3.5
$r_B$ (mm)	2.25	1.8	0.9
$r_A$ (mm)	0.25	0.15	0.1
$b_A$ (mm)	0.3	0.3	0.3
$d_A$ (mm)	0.1	0.15	0.2
$P_A/P_{tot}$ (dB)	-10	-10	-10
Band (GHz)	13-44	16-37	17.6-34
Band (%)	108.77	79.25	63.57

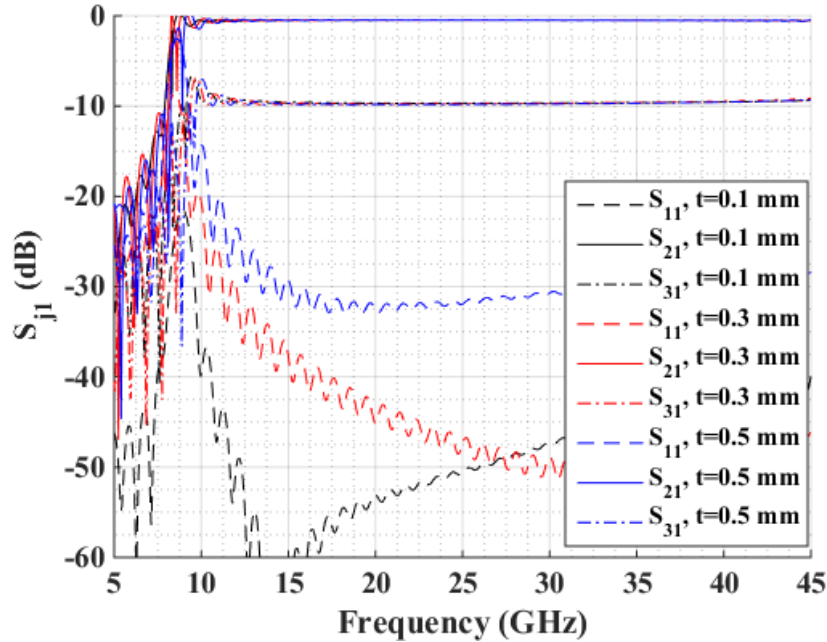


Fig. 4.7. Parametric study on the effect of sheet thickness on the S-parameters of the wideband splitter using CST.

## 4.4 Wideband Reconfigurable Ridge Gap Waveguide Splitter

Reconfigurable power splitter has several applications like tunable beamforming network and antenna arrays. In satellite applications, the reconfigurable power splitter is used to reconfigure the antenna coverage spot [40]. In the next sections, an RGW reconfigurable power splitter (which can give any power split ratio on wide bandwidth) is introduced. Since the splitter can achieve any power split ratio, then it can be regarded as a switch. A literature survey on the reconfigurable power dividers and switches in different technologies is shown next.

### 4.4.1 Design of the reconfigurable power divider

The geometry of the reconfigurable power splitter is shown in Fig. 4.8. It consists of two ridge gap waveguides with a common upper wall realized using a deflectable sheet. This sheet starts in the mid-length of the device such that the device consists of 3 ports: one of its 3 ports is the double ridge gap waveguide (DRGW) shown in Fig. 4.8(b) (named port 1) and the other two ports (2 and

3) are the ridge gap waveguide ports shown in Fig. 4.8(c). In the power division mode, the power enters the structure from port 1 to exit the structure from ports 2 and 3 after being separated by the metallic sheet of thickness  $t$ . Due to the possible leakage of different polarizations supported by the sheet, a packaged soft surface is used to confine the power of both polarizations at the sheet tip position in the device. This packaged soft surface does not necessarily have the same dimensions of the pins in the bed of nails. The position of the sheet tip between the upper and lower ridges of guide 1 decides the power division ratio between guides (ports) 2 and 3. The sheet tip position can be changed by means of 2 metallic posts located behind the packaged soft surface where no field exists, such that the tuning mechanism does not affect the S-parameters of the 3-port device.

If the height of the ridge was chosen equal to or more than the height of the pins in the single ridge waveguide, this allows the sheet to touch the ridge at the highest deflection. This makes all the power go to only one guide, which means that the 3-port device may work as a switch. In most cases, the height of the ridge is chosen equal to or less than the height of the soft surface in order to ensure wider bandwidth.

Some requirements have to be fulfilled for the reconfigurable power divider to work as intended:

- a- A DRGW (port 1) that can confine the electromagnetic power to the ridge region.
- b- An RGW (ports 2 and 3) that can confine the power to the ridge region.
- c- A packaged soft surface that can confine the power for both ridge gap waveguide and double ridge gap waveguide sides at the sheet tip.

In order to satisfy these requirements, a design procedure is proposed to design the splitter. The design procedure allows the choice of the maximum split ratio provided by the splitter as well as choosing the frequency range on which the splitter works and the bandwidth. The design procedure starts by deciding the maximum power division ratio required. The maximum power division ratio  $PSR_{max}$  with the maximum operating frequency decides approximately the height of the ridge with respect to the height of the soft surface at the splitting region. The upper-frequency limit for the stop band of the packaged soft surface may be used to determine the approximate height of the DRGW. The DRGW height  $h_d$  is approximated as:

$$h_d = 2 * h_s + t = \frac{C}{2 * f_{max}} \quad (4.7)$$

where  $t$  represents the sheet thickness,  $C$  is the speed of light in air,  $f_{max}$  is the maximum frequency of interest, and  $h_s$  is the height of one RGW, as illustrated in Fig. 4.8. By assuming the sheet thickness  $t$ , the value of  $h_s$  may be obtained. After that, a linear approximation of the relation between the power and the height of the gap above the ridge in the RGW would lead to the approximate relation:

$$PSR_{max} = \frac{h_{ss} - h_r}{2h_s - h_{ss}}. \quad (4.8)$$

which leads to an approximate ratio between  $h_{ss}$  and  $h_r$ .

After that, the obtained approximate values of  $h_s$  and  $h_r$  may be used to start 1D eigenmode simulations to optimize their approximate values and obtain the other dimensions of the RGW and DRGW. After that, an eigenmode analysis of the packaged soft surface is done in order to tune its parameters according to the required band of operation. After obtaining all the parameters, S-parameter simulation may be carried out to see if the required specifications have been met.

#### 4.4.2 Parametric studies and results

In this section, one example of a reconfigurable power splitter designed to work on the Ka-band is shown with all parameter values and simulation results. Since the splitter works on the Ka-band, this implies  $f_{max} = 40$  GHz. This means according to (4.7) that  $h_s = 1.7$  mm. If  $PSR_{max}$  is zero (which is equivalent to operating as a switch in the extreme case) is required, this makes  $h_{ss} = h_r$ . After that, 1D eigenmode analysis is carried out using commercial software CST, as shown in Fig. 4.9(a), to design the RGW and DRGW for the specified bandwidth. The resulting 1D-dispersion diagrams are shown in Fig. 4.9(b,c) for the DRGW and RGW, respectively. As shown in the figure, the DRGW and RGW can cover the whole Ka-band if proper values of the gap height, the pin period and the pin dimensions are chosen. After that, 1D eigenmode analysis of the packaged soft surface on both sides of the sheet is carried out in order to ensure good packaging in all deflections of the sheet. The dimensions of the variable splitter, obtained through the eigenmode analysis, are all listed in Table 4.5.

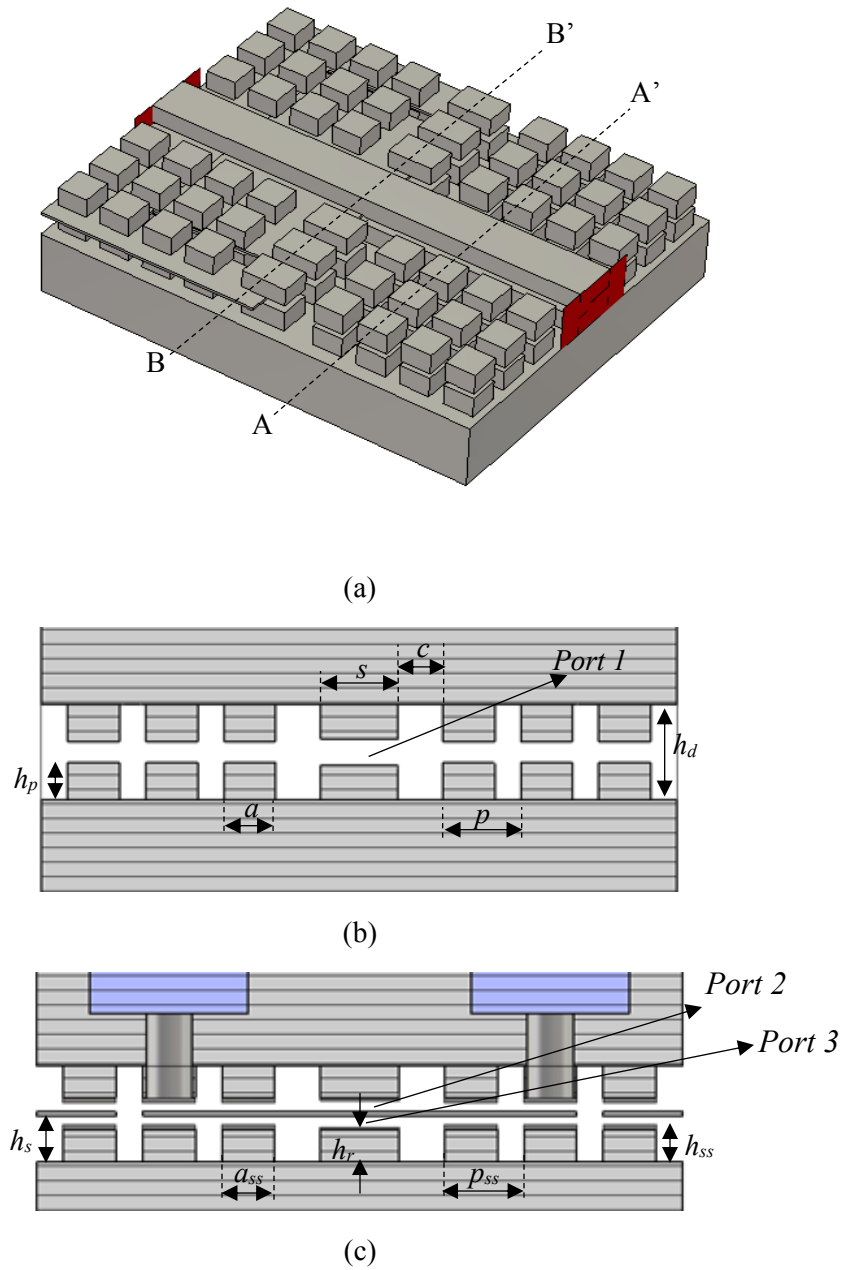


Fig. 4.8. Geometry of the reconfigurable power splitter with all design parameters shown. (a) Isometric view. (b) Section AA'. (c) Section BB'.

The last step is to obtain the S-parameters of the designed splitter in order to see if the requirement has been met. The dimensions of the soft surface have been optimized in order to ensure good operation of the splitter for all splitting ratios.

In order to simulate the deflected sheet, the sheet profile is needed. If a vertically applied force  $F$  at the sheet tip is assumed to deflect the sheet, The sheet profile  $\delta(x)$  is obtained, as mentioned in [135]:

$$\delta(x) = \frac{2Fx^2}{Ewt^3}(3L - x)$$

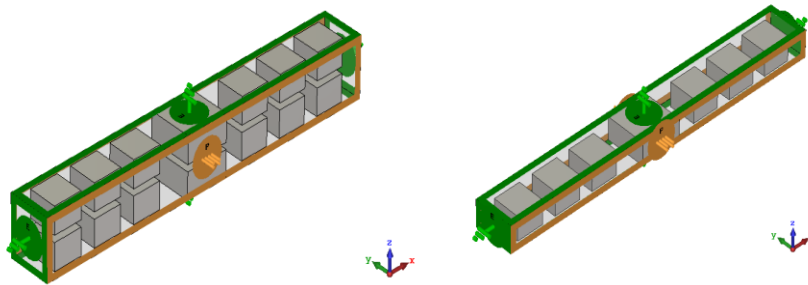
where  $E$  is Young's modulus for the sheet material (68.9 KN/mm<sup>2</sup> for Aluminum). The parameters  $L$ ,  $w$ , and  $t$  are the free-deflection length, width, and thickness of the sheet, respectively, while  $\delta(x)$  is the deflection of the sheet at each point.

Table 4.5: Values of different parameters of the reconfigurable power splitter following Fig. 4.8 notation

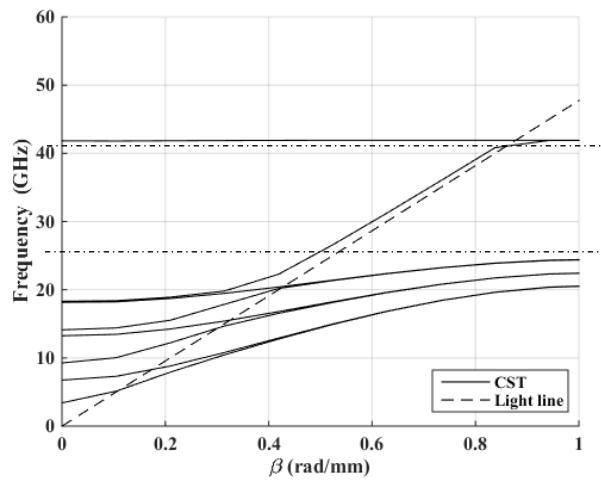
<b>Parameter</b>	$t$	$s$	$c$	$a$	$p$	$a_{ss}$	$h_{ss}$
<b>Value (mm)</b>	0.2	3	1.7	2	3	2	1.5
<b>Parameter</b>	$p_{ss}$	$h_s$	$h_p$	$h_d$	$h_r$	$l$	
<b>Value (mm)</b>	3	1.7	1.5	3.6	1.5	2	

The resulting  $S_{11}$  and  $S_{31}$  of the splitter in 3 different states are shown in Fig. 4.10. As illustrated in the figure, the splitter can give any power split ratio over the whole Ka-band with a return loss better than 15 dB. One drawback for this splitter is the isolation between the two output ports in case any power is reflected back. This drawback may be avoided in practice by using isolators at the output port, yet the splitter in this compact form may be used in several applications, where output port isolation is not necessary.

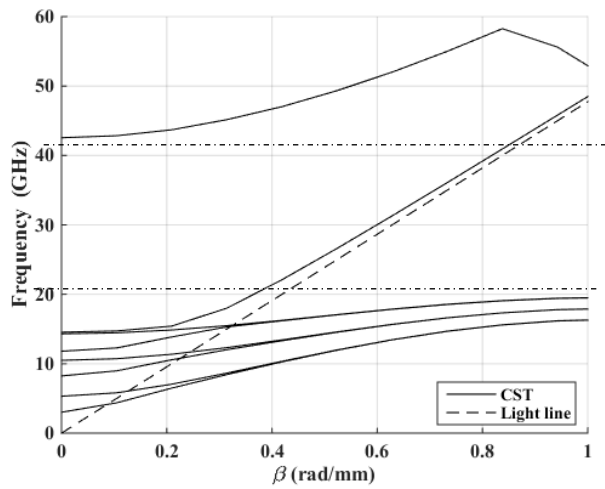
As shown previously, the design of the splitter involves several parameters. As a result, studying the effect of these parameters on the splitter performance is necessary. In this study, the value of the parameter  $c$  was taken equal to 1 mm instead of 1.7 mm to provide wider bandwidth for the study. One of the most important parameters is the height of the soft surface since it decides the maximum possible deflection of the sheet and the widest bandwidth over which the splitter can operate. A study is carried out on the change in the stop band of the packaged soft surface with the soft surface height and width on the double ridge side. Fig. 4.11 shows the results of this study, where the height of the soft surface is shown to be directly proportional to the bandwidth, while the width is shown to have a smaller effect on the bandwidth of the splitter. It is shown that



(a)



(b)



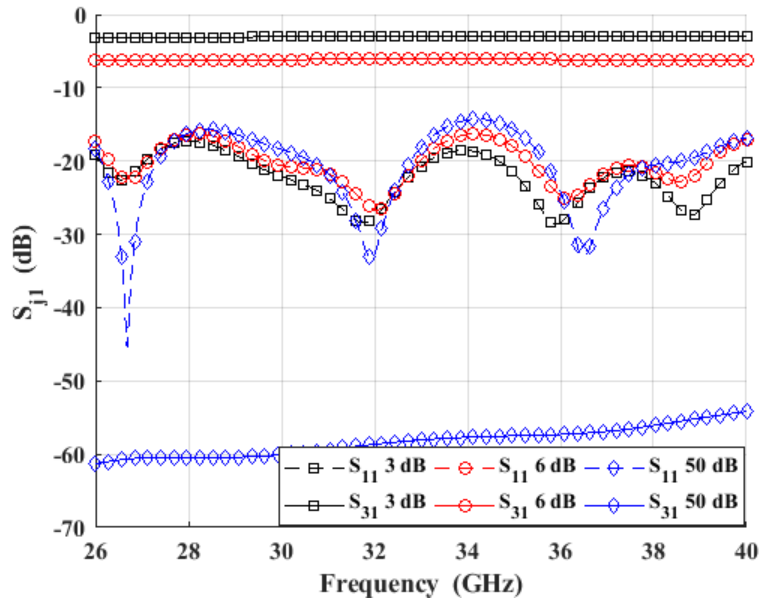
(c)

Fig. 4.9. 1D-eigenmode analysis and its results for DRGW and RGW waveguides. (a) Eigenmode analysis setup in CST. (b) 1D-dispersion diagram of DRGW. (c) 1D-dispersion diagram of RGW.

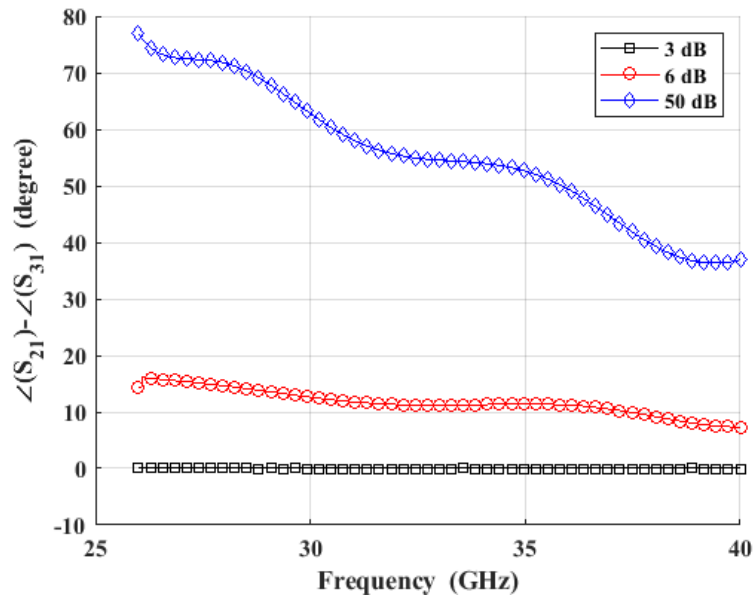
for a gap height of 0.2 mm (where  $h_s=1.7$  mm), the bandwidth of the soft surface on the double ridge side extends from 28 GHz to 43 GHz (42.25 % bandwidth).

Another study is the effect of bending the sheet on the confinement of the waves by the soft surface in the single ridge side. Since bending the sheet increases the gap between the soft surface and the sheet in the top guide of Fig. 4.8(c), a study is done on the stop band of the soft surface at the top guide to see the bandwidth on which the wave will be confined in maximum deflection position. Fig. 4.12 shows that for an initial  $h_s = 1.7$  mm and an initial soft surface height  $h_{ss} = 1.5$  mm, the deflection of 0.2 mm causes the stop band of the soft surface to work from 30 GHz to 43 GHz, which is equivalent to 35.6 % bandwidth instead of 42.25 % of Fig. 4.11. The final bandwidth of this splitter is the intersection of Fig. 4.11 and Fig. 4.12, which is from 30 GHz to 43 GHz. In another case, where  $h_{ss}=1.25$  mm, and initial  $h_s = 1.7$  mm, DRGW side bandwidth is from 35 GHz to 43 GHz, while RGW side (for 0.5 mm maximum deflection) is from 38 GHz to 44 GHz, which makes intersection bandwidth from 38 GHz to 43 GHz (12.35 % bandwidth). Fig. 4.13 shows the bandwidth limitations for the reconfigurable splitter by considering the intersection bandwidth of the splitter ports at best case (3 dB splitting) and worst case (switch) scenarios.

Increasing the soft surface gap height might be important to reduce the sensitivity of the power split ratio to the errors of the tuning mechanism. It also decides the maximum possible height of the ridges (ridges may be of less height if the switch operation is not required). The maximum ridge height decides the minimum power handling capability for a given soft surface height. A parametric study is carried out to show the power handling capacity of the splitter and the corresponding bandwidth as a function of the ridge height for the case, where  $h_s=1.7$  mm. The results of this study are shown in Fig. 4.14, where it can be proved that for a ridge height of 1.5 mm, the single ridge port of the splitter can handle a maximum power level of 5 KW with a 33 % bandwidth, which goes up to 21 KW with 5 % bandwidth for ridge height of 1.125 mm. The maximum power handling capability is, traditionally, increased by putting the waveguide into a vacuum state. In Fig. 4.15, another parametric study is done to show the sensitivity of the device to the deflection of the sheet for different gap heights. It is shown that for  $h_{ss} = h_r = 1.5$  mm ( $h_s=1.7$  mm), the power split ratio is changed from 3 dB to 12 dB for 0.2 mm of deflection, while phase error is below  $-15^\circ$ .



(a)



(b)

Fig. 4.10. S-parameters for the splitter in different states of 3 dB, 6 dB and 60 dB splitting. (a) Magnitude of  $S_{11}$  and  $S_{31}$  in dB. (b) Phase difference between output arms.

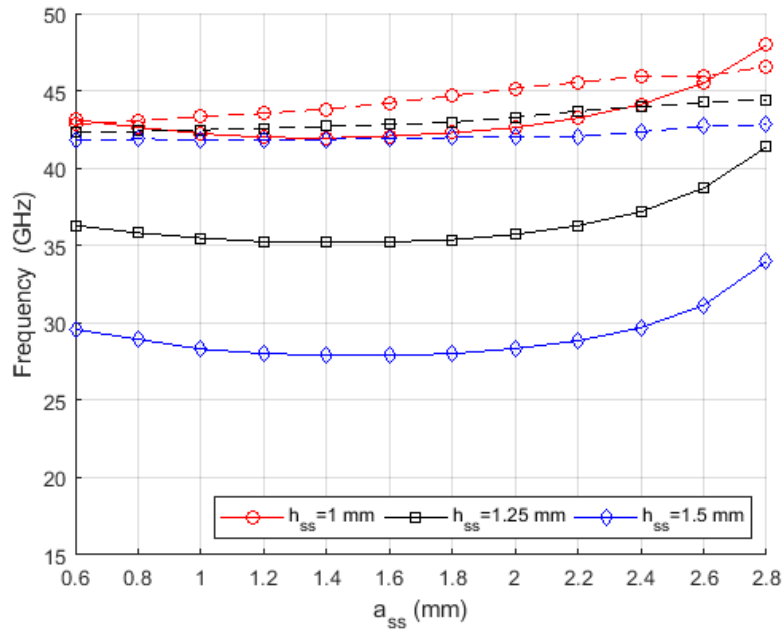


Fig. 4.11. Parametric study on the effect of varying  $h_{ss}$  and  $a_{ss}$  on the upper (dashed) and lower (solid) frequency limits of the DRGW side of the reconfigurable splitter.

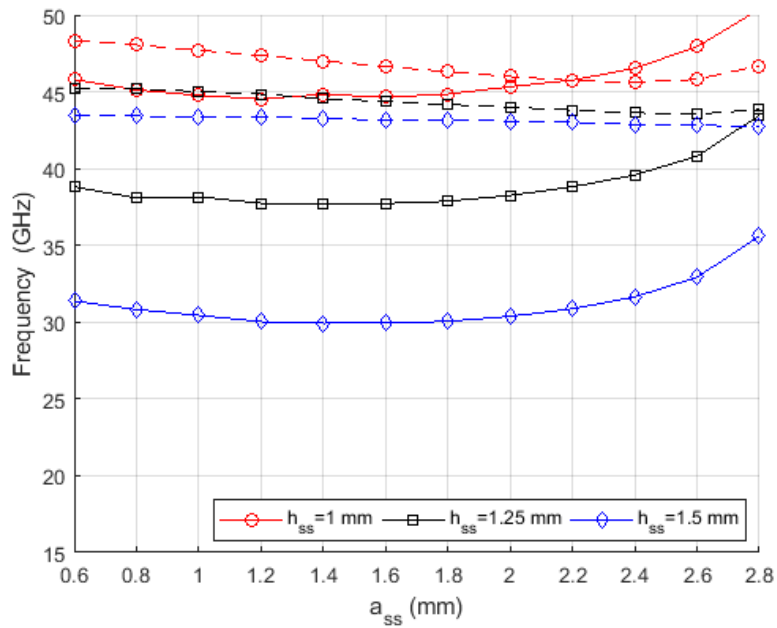


Fig. 4.12. Parametric study on the effect of the maximum sheet deflection on the upper (dashed) and lower (solid) frequency limits of the reconfigurable splitter for several values of  $h_{ss}$  and  $a_{ss}$ .

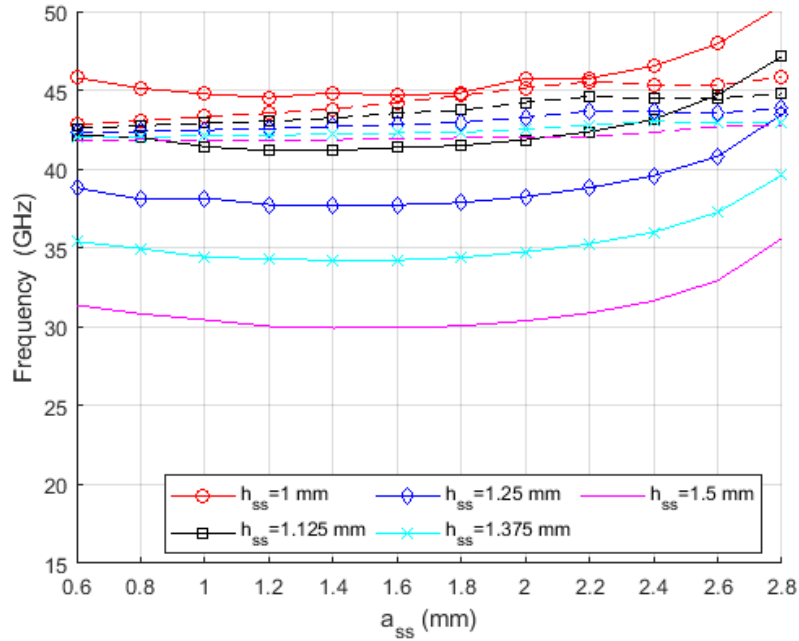


Fig. 4.13. Parametric study on the upper (dashed) and lower (solid) frequency limits of the reconfigurable splitter for several values of  $h_{ss}$  and  $a_{ss}$  ( $h_{ss}=1$  mm shows zero bandwidth).

The final simulation and measurement results of the variable splitter are presented and compared. The splitter is manufactured from Aluminum using CNC machining and measured by using *PNA Network Analyzer N5227A* using the transition in [73]. Table 4.6 shows a comparison between the splitter presented here and different splitters in literature. A photo for the measurement setup is shown in Fig. 4.16, where equal power split ratio is desired. The measured and simulated S-parameters for the variable splitter are shown in Fig. 4.17, where the simulated and measured return losses are better than 8 dB from 26 GHz to 40 GHz in all the states. The simulated phase difference between ports 2 and 3 is less than  $25^\circ$  from 26 to 40 GHz, while the measured phase difference is  $-10^\circ \pm 20^\circ$  from 26 to 40 GHz. Two different power split ratios are shown in Fig. 4.17 (a, b). The high return loss and the fluctuation in the power split ratio are due to the return loss and insertion loss of the transition.

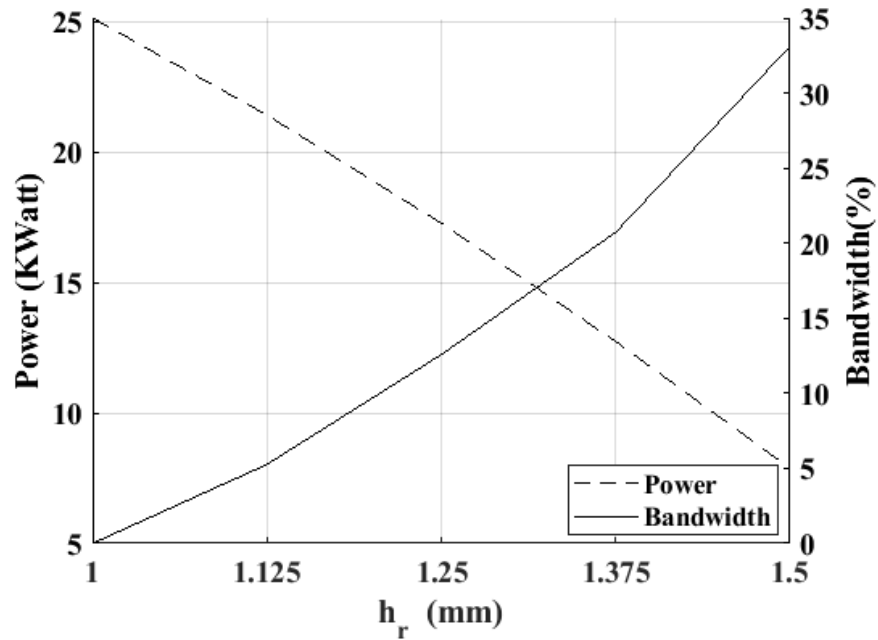


Fig. 4.14. Maximum power handling capability of the splitter and the corresponding bandwidth for different ridge heights ( $h_r = h_{ss}$ )

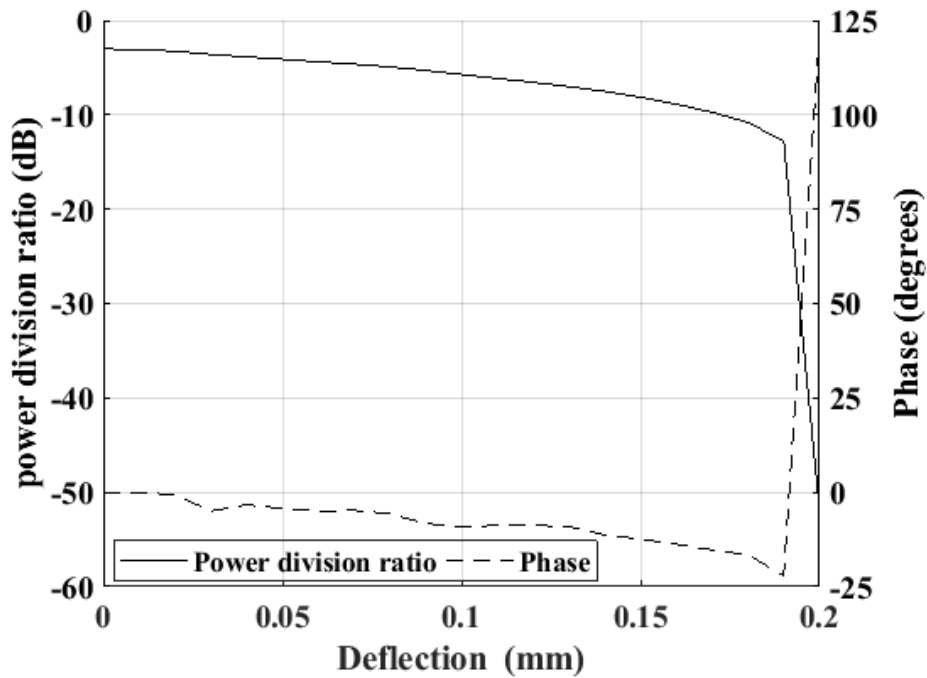


Fig. 4.15. Parametric study on power division ratio and phase difference provided by different sheet deflections.

Table 4.6: Comparison between different variable splitters in the literature.

References	Frequency / bandwidth	Technology	Tuning means	Tunable operation
[85]	Around 1 GHz	Printed	Varactor	Variable power division ratio 2:44 dB (in or out of phase)
[86]	1.98-2.02 GHz	Printed	Varactor	2:1 to 4:1 power division ratio
[87]	4.6% around 5 GHz	Printed	Pin diodes	1:5 to 1:0 division ratio
[91]	4.6-5.3 GHz	Printed	Pin diodes	SPDT to power divider
[40]	16 % in Ku band	Regular WG	2 reconfigurable phase shifters + 2 90° hybrids	Variable power division ratio
[41]	10-12 GHz	Regular WG	Polarizer + 2 OMT	Variable power division ratio
[92]	Not mentioned	Regular WG	Ferrite with tunable bias current	Variable power division ratio.
This work	26-40 GHz	RGW	Deflectable sheet	Power split ratio from 1:0 up to 0:1.

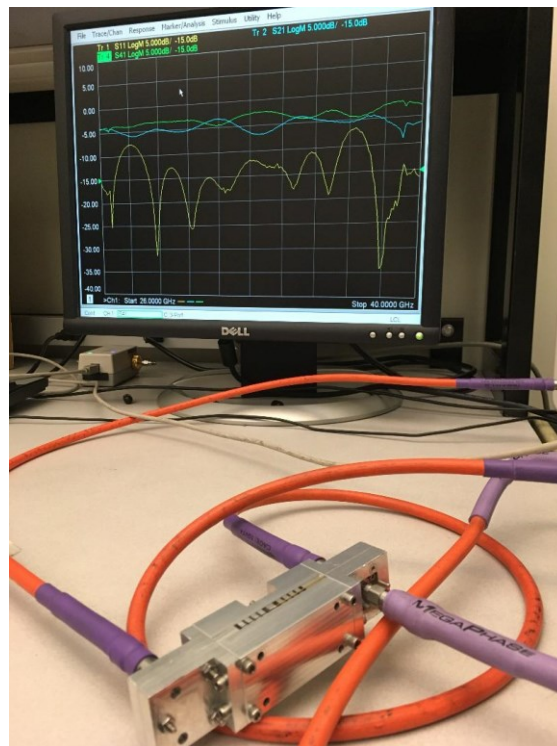
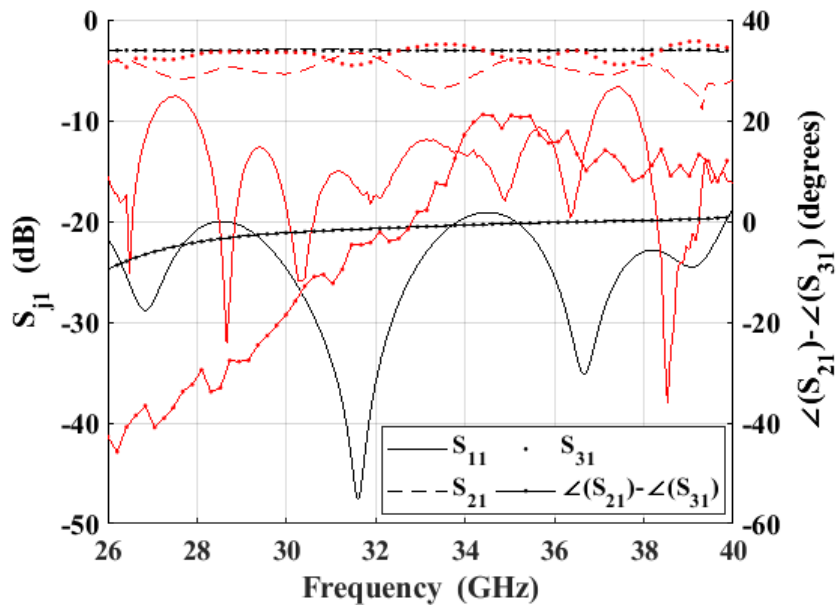
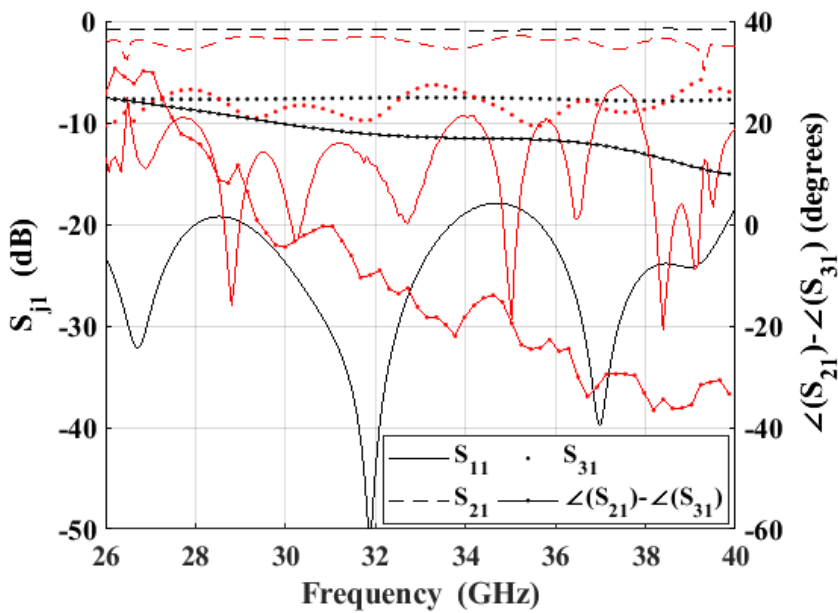


Fig. 4.16. Photo of the measurement setup of the reconfigurable splitter with 3-dB power split ratio shown.



(a)



(b)

Fig. 4.17. Comparison of the measured (red) and simulated (black) S-parameters for different cases of the reconfigurable splitter. (a) 3-dB case. (b) 8-dB splitter.

# Chapter 5

## Arbitrary-coupling RGW Quadrature Hybrid

### 5.1 Introduction

In this chapter, a  $90^\circ$  hybrid coupler is designed using the RGW to work from 15 GHz to 22.5 GHz. The coupler is able to provide any coupling level from 3 dB to 33 dB. It can also provide a return loss and isolation better than 25 dB on more than 30 % of bandwidth and can provide return loss and isolation better than 20 dB over 40 % of bandwidth. A literature survey on different couplers is shown in the next section, followed by the design of the coupler and the results.

### 5.2 Coupler Geometry and Theory of Operation

The coupler geometry structure is shown in Fig. 5.1. It consists of two parallel RGWs sharing a common broad wall sheet. The RGW used in this prototype is the one used for the vertical transition and shown in Fig. 3.12, whose dispersion diagrams are shown in Fig. 3.13. Dispersion diagrams show that the RGW has single-mode bandwidth from 13 to 28.7 GHz. The parameters of this RGW are  $a=3$  mm,  $p=5$  mm,  $s=3.5$  mm,  $c=3.1$  mm,  $h=3.3$  mm,  $r=2.2$  mm, and  $g=0.3$  mm, according to Fig. 1.6 notation. Coupling takes place when power is transferred from one waveguide to the other through holes in the sheet. The holes are made on the sides of the ridge to maintain acceptable return loss for the coupler. The size and number of holes control the coupling level. In the coupler presented here, two modes coexist in the coupling region, which are a TEM even mode and the TE odd mode of the double RGW. A special characteristic in this coupler over other multimode couplers is the ability to tune of the coupling level by changing the gap height; hence, changing the characteristics of the two modes existing in the coupling region. To understand this better, the coupler is analyzed using even-odd analysis, where the odd mode is the double ridge gap waveguide mode (which may be represented by the ridge gap waveguide mode in one waveguide), while the even mode is obtained by replacing the slots by a PMC wall in order to separate the upper and lower guides. In an even-odd analysis of coupler, the S-parameters of the couplers can be obtained from the S-parameters of the even and odd problems as follows:

$$\begin{aligned}
S_{11} &= \frac{S_{11e} + S_{11o}}{2} & , & & S_{21} &= \frac{S_{11e} - S_{11o}}{2} \\
S_{31} &= \frac{S_{21e} + S_{21o}}{2} & , & & S_{41} &= \frac{S_{21e} - S_{21o}}{2}
\end{aligned}
\tag{5.1}$$

where  $S_{21}$ ,  $S_{31}$ , and  $S_{41}$  represent the S-parameters of the isolated, through and coupled ports, respectively, while  $S_{11e,o}$  and  $S_{21e,o}$  are the reflection and transmission coefficient of the even and odd problems, respectively. The characteristic impedance of the even and odd modes can be obtained using the equivalent single ridge waveguide using the resemblance between single ridge waveguide and RGW mentioned in [13]. The characteristic impedances of the even and odd modes of the equivalent single ridge waveguide are obtained from ANSYS by replacing the slot by a PMC sheet for even mode and by a PEC sheet for the odd mode.

Three types of waveguides are analyzed, and their characteristic impedances are plotted in Fig. 5.2(a). One of them is the normal single ridge waveguide (accounting for the odd mode), the other two are having PMC sheet on one side (denoted ‘‘PMC 1 slot’’ in the figure) and on both sides of the ridge (denoted ‘‘PMC 2 slots’’ in the figure). As shown in the figure, having 2 slots covered with PMC turns the guide into a TEM guide of constant characteristic impedance at  $120\pi$ . The difference in the characteristic impedance of the 3 guides ensures the existence of non-zero coupling. In addition, the propagation constants of the 3 guides are plotted in Fig. 5.2 (b), where it is shown that they have a constant difference over a wide bandwidth. According to even-odd analysis [10], perfect matching is achieved if  $Z_o = \sqrt{Z_{oe}Z_{oo}}$ . Also, the coupling may be obtained using:

$$S_{41} = \frac{j(Z_{oe} - Z_{oo})}{2 Z_o \cot((\beta_e - \beta_o)l) + j(Z_{oe} + Z_{oo})}
\tag{5.2}$$

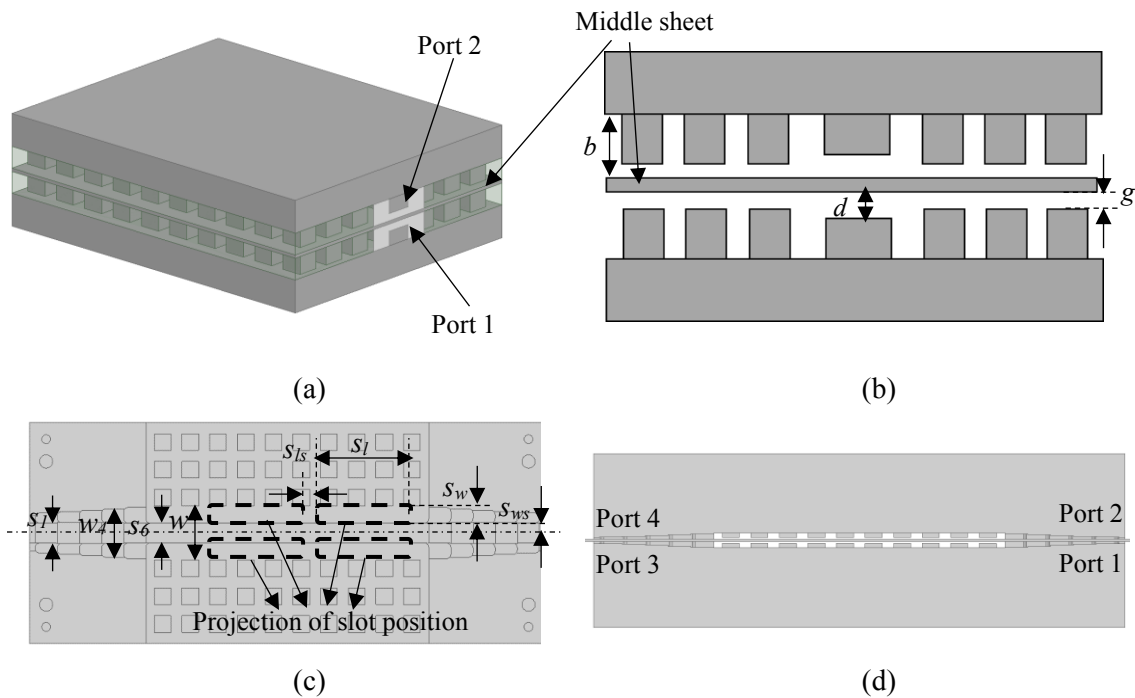
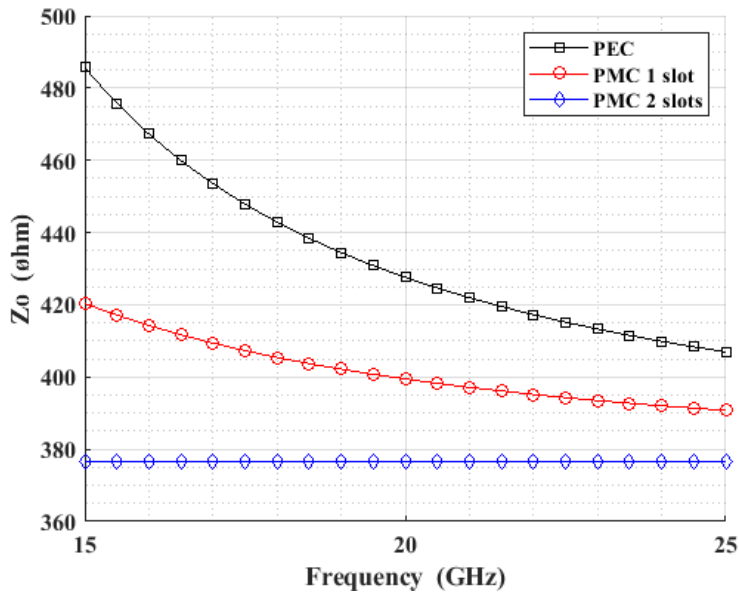


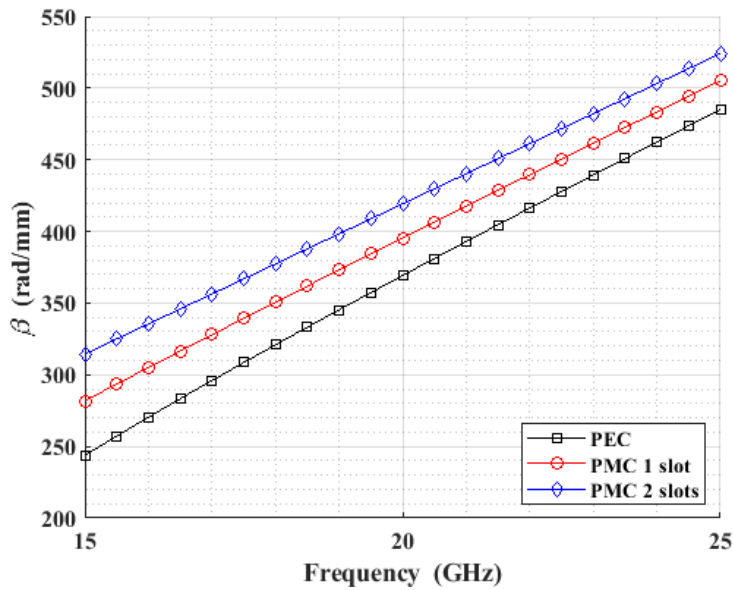
Fig. 5.1. Directional coupler structure showing its parameters. (a) 3D view without the transformer (b) Transversal cross-section, (c) The lower half of the coupler with transformer. Positions of slots are dotted. (d) A longitudinal section.

The 10 dB and 15 dB coupler design procedure would be:

1. Make sure the single mode band of the RGW contains the desired coupler band.
2. Extract  $Z_0$  and  $\beta$  of the even and odd problems for the assumed guide dimensions. Use 1 PMC slot for the even problem if the required coupling is  $\geq 12$  dB and use 2 PMC slots otherwise. The intersection of the slots with the ridge should be small enough to avoid high reflection.
3. Assume slot(s) length  $l = \lambda_o$  at the center frequency of the desired band.
4. Verify that  $S_{41}$  computed using (5.2) is close to the required coupling value otherwise repeat steps 1-3 for different dimensions until  $S_{41}$  is close to the required coupling value.
5. Use full-wave simulation to optimize the obtained dimensions.



(a)



(b)

Fig. 5.2. Characteristic impedances and the propagation constants of the 3 guides required in the eigenmode analysis: (a) Characteristic impedance. (b) Propagation constant.

For the 3 and 6 dB couplers, it might be required to use more than 2 slots on the coupling sheet. In that case, a 9 dB coupler is designed using steps 1-3 of the previous procedure then a second row of slots (1 slot on one side of the ridge for 6 dB coupler and 2 slots on both sides of the ridge

for 3 dB coupler) is added to the coupling sheet then the full-wave optimization is carried out to obtain the final dimensions of the coupler. In order to show the difference between the calculated coupling using (5.2) and the full-wave analysis final result, the coupling is plotted in Fig. 5.3 for both the 2 slots (eventually 10 dB coupler) and 1 slot (eventually 15 dB coupler) cases.

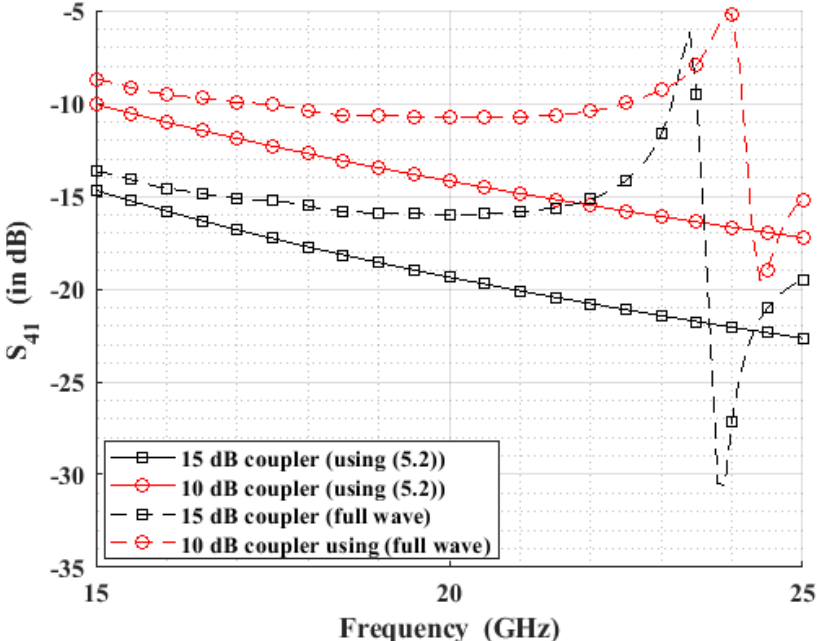
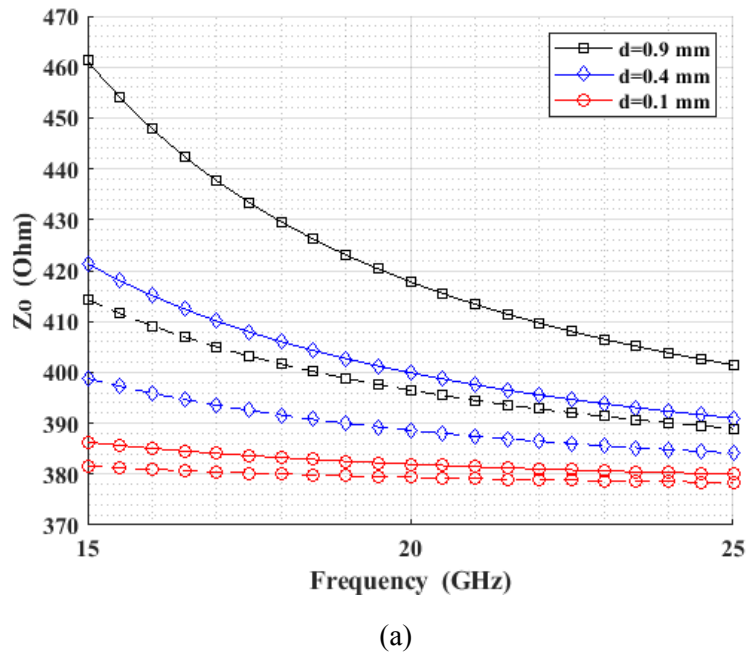
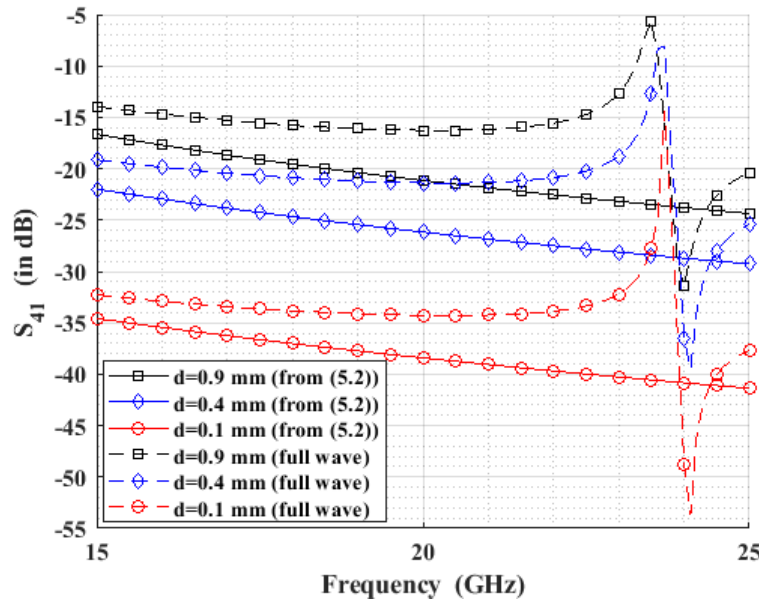


Fig. 5.3. Comparison of coupling computed using (5.2) to full-wave analysis for 1-slot waveguide (15 dB coupler) and 2-slot waveguide (10 dB coupler) .

It is shown that the initial coupling obtained using (5.2) is close to the full-wave analysis results. The deviation of the coupling calculated by (5.2) from the full-wave analysis results is due to not accounting for the discontinuities at the coupling region boundary, which has not been done in the literature. After that, a study on the effect of the gap height on the coupling level of the 1 slot coupler is carried out. The characteristic impedances of the even and odd mode guides for single slot coupler are obtained using ANSYS for several ridge heights then used to obtain the coupling coefficient using (5.2).



(a)



(b)

Fig. 5.4. (a) Characteristic impedance of the even (solid) and odd (dashed) modes of the 1 slot coupler for several ridge heights. (b) Comparison of the coupling level obtained using (5.2) and the full-wave results.

The characteristic impedances and coupling plots are shown in Fig. 5.4. It is shown that the greater the ridge height, the lower the coupling value. It is not possible to obtain an exact coupling level

estimation using (5.2) due to several factors such as neglecting the effect of discontinuity at the end of the coupling region.

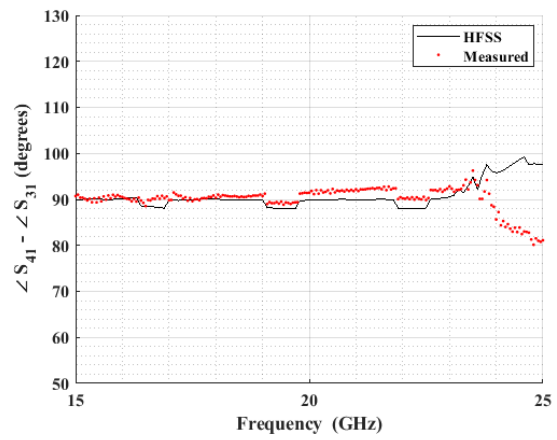
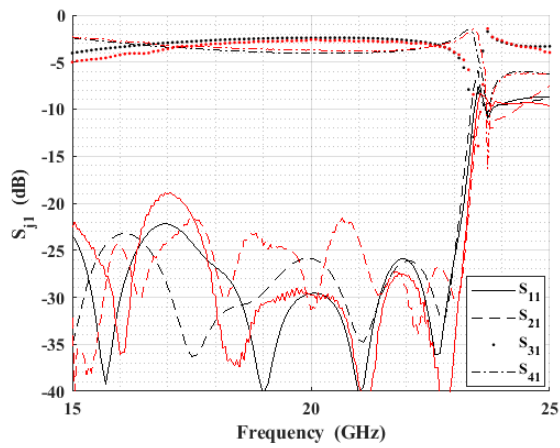
### 5.3 Results and Parametric Studies

In this section, several wideband couplers of coupling levels 3 dB, 6 dB, 10 dB, 15 dB with ( $90^\circ(\pm 2^\circ)$ ) phase difference are introduced. Couplers are working from 15 GHz to 22.5 GHz (40 % bandwidth percentage), where values of the parameters for each case are shown in Table 5.1 following the notation of Fig. 5.1. The simulated and measured results of the coupler are shown in Fig. 5.5 (a-d). Fig. 5.6 shows a photo of the measurement setup for 6 dB coupler and a photo of the manufactured structures. A comparison for the coupler characteristics to the state-of-the-art RGW couplers is shown in Table 5.2, where the bandwidth, magnitude and phase error of the coupler and its area are shown. It can be deduced from the table that the coupler presented here is superior to other couplers in terms of bandwidth.

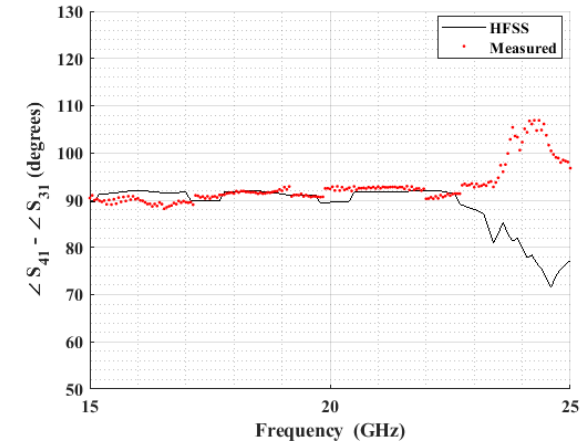
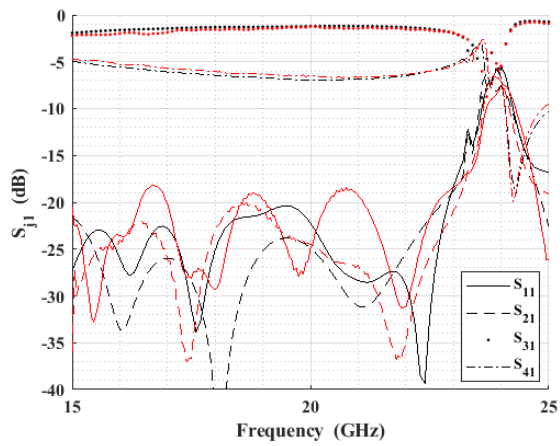
A parametric study is carried out on several parameters of the coupler to show their effect on the coupling level and the bandwidth. In this study, the following parameters are used unless otherwise stated:  $s_{ws} = 2.4$  mm,  $s_w = 2.7$  mm,  $s_l = 14$  mm,  $s_{ls} = 1$  mm, and  $t = 0.5$  mm. In Fig. 5.7, it can be shown that the bandwidth is inversely proportional to the sheet thickness. This is due to the higher order mode that originates in the coupling region when the height of the coupling region is more than twice the RGW's height. Fig. 5.8 shows the effect of the RGW ridge height on the coupling level of the coupler. It is shown that the height of the gap is directly proportional to the coupling levels, where the coupling level changes from 15 dB to 33 dB if the ridge height changes from 0.1 mm to 0.9 mm.

Table 5.1: Values of the parameters of different couplers in Fig. 5.5 (next), following Fig. 5.1 notation.

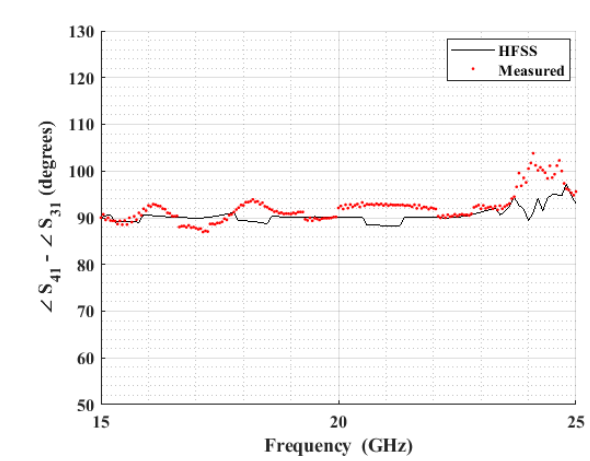
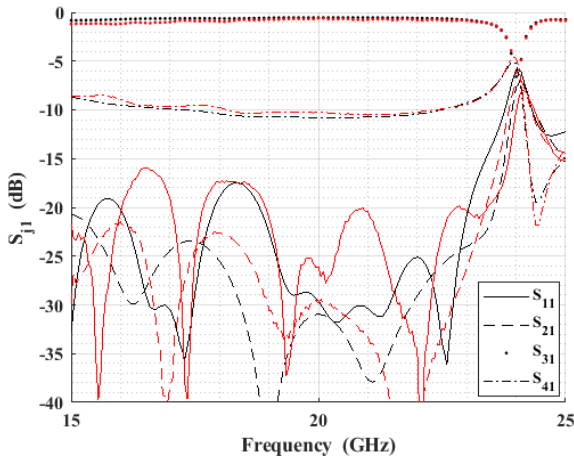
Parameter Coupler Case	$s_l$ (mm)	$s_w$ (mm)	$s_{ws}$ (mm)	$s_{ls}$ (mm)	# of slots
(a)	15	3	1.6	2.5	4
(b)	14	3.2	1.6	1	3
(c)	13.5	3	1.8	N/A	2
(d)	13.7	3.4	1.9	N/A	1



(a)



(b)



(c)

Fig. 5.5. Simulated (black) and measured (red) S-parameters of the proposed coupler with different coupling levels fed by the vertical transition (a) 3 dB (b) 6 dB (c) 10 dB, Results are obtained using ANSYS.

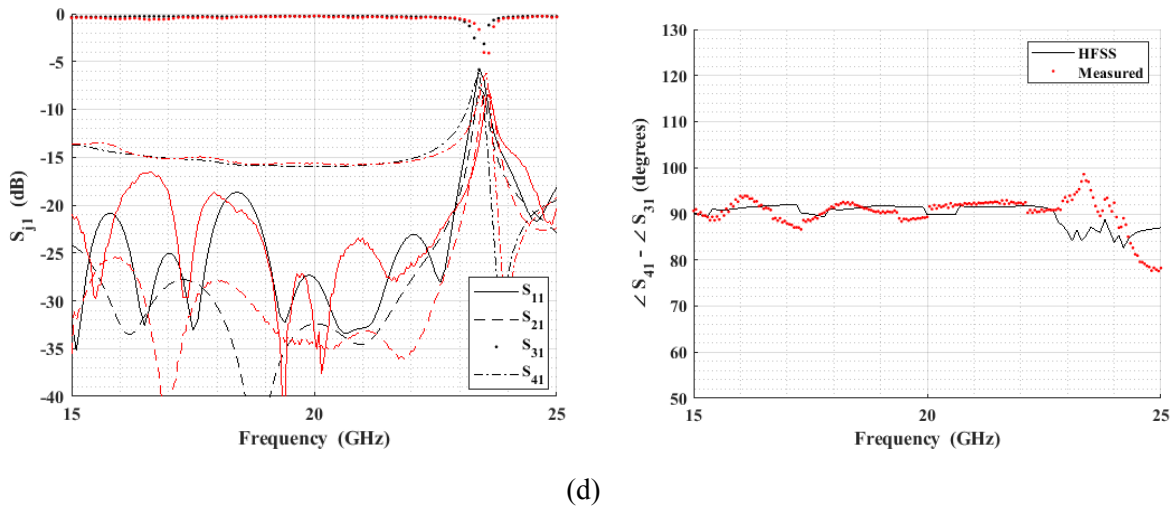
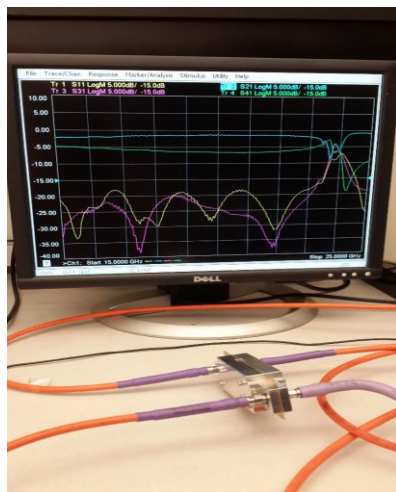


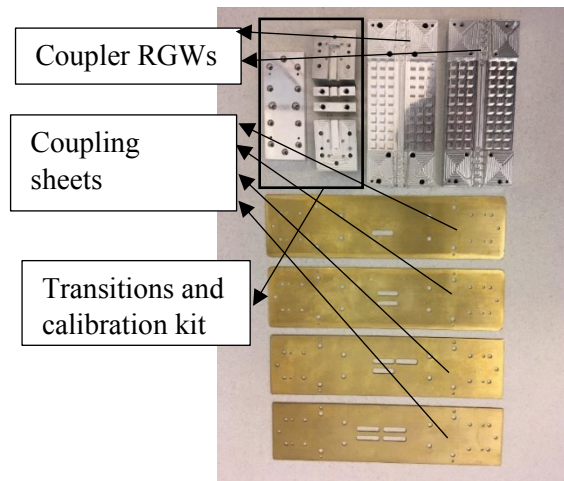
Fig. 5.5. Simulated (black) and measured (red) S-parameters of the proposed coupler with different coupling levels fed by the vertical transition (d) 15 dB. Results are obtained using ANSYS.

Table 5.2: Comparison of different RGW couplers in literature.

References	Technology	Bandwidth	Size	Coupling
[106]	RGW	30%	$6 \lambda_o$ long	$9$ & $18.5 \pm 1$ dB
[107]	RGW	14%	$1.6 \times 1.6 \lambda$	$3 \pm 1$ dB
[109]	GGW	14%	$4.7 \lambda_o$ long	$3 \pm 1$ dB $90^\circ \pm 1^\circ$
[111]	PRGW	13%	$2 \lambda_g$ long	3 dB $90^\circ \pm 1^\circ$
This work	RGW	40%	$2 \lambda_o$ long	$3 \pm 1$ dB $90^\circ \pm 2^\circ$



(a)



(b)

Fig. 5.6. (a) Photo of the measurement setup of the 6 dB coupler. (b) Photo of the manufactured structure.

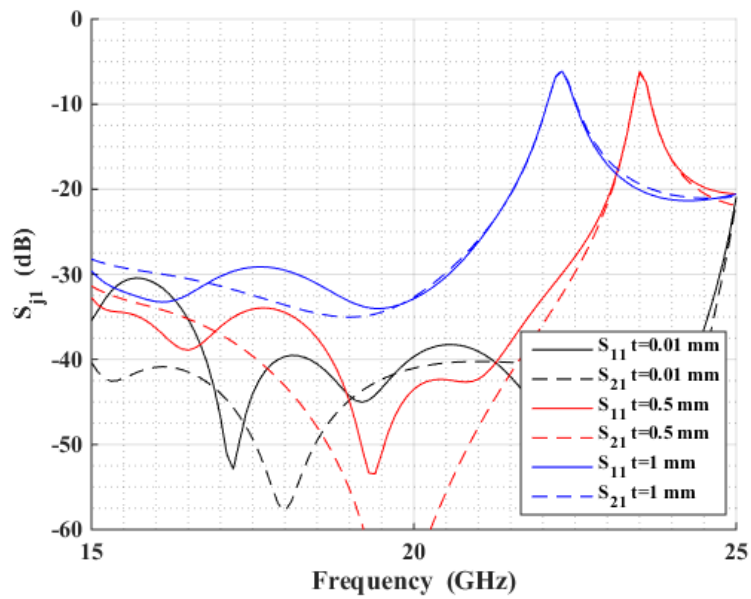


Fig. 5.7. Effect of the sheet thickness on the coupler bandwidth obtained using ANSYS.

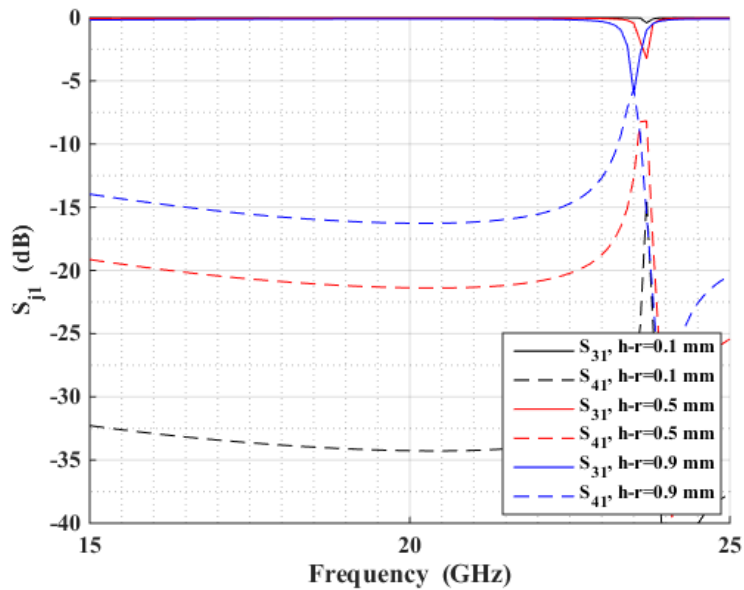


Fig. 5.8. Effect of ridge height on the coupling level of the coupler obtained using ANSYS.

# Chapter 6

## Low-Error Reconfigurable Phase Shifter Using RGW

### 6.1 Introduction

A reconfigurable phase shifter is designed using the ridge gap waveguide with a rectangular waveguide to operate in the Ka-band. The ridge gap waveguide is used to couple the power to and from the phase shifter input and output arms. The phase shifter is designed using a broad wall rectangular waveguide coupler, where two fixed screws, and two tunable screws are used with waveguide short circuits to provide a phase shift up to  $200^\circ$  with a worst-case error less than  $\pm 15^\circ$ .

### 6.2 Analysis of Reflection-type Phase Shifter

The reflection type phase shifter is based on the use of a hybrid coupler terminated by 2 reactive loads of tunable reactances at two of its 4 ports. The reactive loads at these two ports are used to provide a variable phase shift, which ends up in the form of a phase shift between the input and the output signals at the other two ports. For example, the schematic in Fig. 6.1 shows a  $90^\circ$  hybrid coupler terminated by two identical phase shifting elements at ports 2 and 3 introducing a phase shift  $\varphi_x$ . If a signal of incident wave amplitude  $a_1$  is input from port 1, the incident wave amplitudes at ports 2 and 3 may be, ideally, expressed as:

$$b_2 = \frac{a_1}{\sqrt{2}}, \text{ and } b_3 = \frac{a_1}{\sqrt{2}} \angle 90^\circ$$

After introducing the phase shift, the reflected wave amplitude at ports 2 and 3, assuming zero delay lines between different components, can be expressed as:

$$a_2 = \frac{a_1}{\sqrt{2}} \angle -180^\circ - 2\varphi_x, \text{ and } a_3 = \frac{a_1}{\sqrt{2}} \angle -90^\circ - 2\varphi_x$$

After passing through the coupler, the wave amplitudes at ports 1 and 4 are represented as:

$$b_1 = \frac{a_2}{\sqrt{2}} + \frac{a_3}{\sqrt{2}} \angle 90^\circ = 0, \text{ and}$$
$$b_4 = \frac{a_3}{\sqrt{2}} + \frac{a_2}{\sqrt{2}} \angle 90^\circ = a_1 \angle -90^\circ - 2\varphi_x.$$

Ideally, all the power is supposed to go to port 4 with no power reflected at port 1. As indicated

in the previous equation, the phase shift introduced at port 4 can be controlled by the value of the phase shift  $\varphi_x$  introduced at ports 2 and 3. The maximum phase shift introduced by  $\varphi_x$  decides the maximum phase shift of the device. This ideal situation, however, does not exist in practice due to several factors like phase error of the hybrid, balance error in the hybrid output at the coupled and through ports, and non-zero return loss and isolation of the hybrid. These factors will deteriorate the return loss at port 1, which would not be ideally zero. It is necessary to study these factors in order to decide what is the appropriate constraints on the hybrid to obtain satisfactory results. If the isolation and return loss of the hybrid are assumed better than 20 dB. The two remaining factors to study are the phase and balance errors of the 90° hybrid.

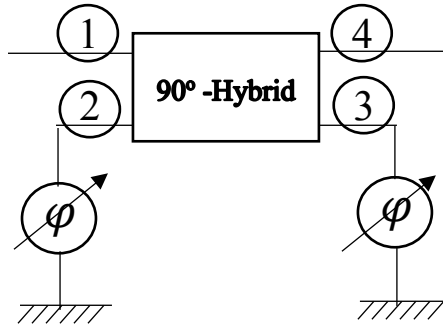


Fig. 6.1: Schematic of the reflection type phase shifter.

If the erroneous  $b_2$  and  $b_3$  may be expressed, with  $a_1$  assumed unity, as:

$$b_2 = \sqrt{0.5 + \Delta P}$$

$$b_3 = \sqrt{0.5 - \Delta P} \angle (90^\circ + \Delta\varphi)$$

where  $\Delta P$  represents the power error and  $\Delta\varphi$  represents the phase error. As a result, the final reflected wave amplitudes are:

$$b_1 = b_2 a_2 + b_3 a_3$$

$$b_1 = (0.5 - \Delta P) \angle (-2\varphi_x + 2\Delta\varphi) - (0.5 + \Delta P) \angle (-2\varphi_x) \quad (6.1)$$

$$b_4 = b_2 a_3 + b_3 a_2$$

$$b_4 = 2\sqrt{(0.5 + \Delta P)(0.5 - \Delta P)} \angle (-90^\circ - 2\varphi_x + \Delta\varphi) \quad (6.2)$$

both of which represent  $S_{11}$  and  $S_{41}$ , respectively.

As deduced from (6.1) and (6.2), the power and phase errors do not affect the relative value of the phase shift introduced. However, the value of the transmission and reflection coefficients are the most affected by these errors.

In order to quantify the effect of the coupler errors on the S-parameters, Fig. 6.2 shows the values of the reflection coefficient of the phase shifter versus the power and phase error of the coupler. This plot is a useful design tool for the reflection-type phase shifter. It shows the requirement of a good hybrid that may be used in the design of this phase shifter.

### 6.3 Phase Shifter Design and Parametric Studies

The design of the reflection-type phase shifter is shown in Fig. 6.3, which is designed using a rectangular waveguide broad wall coupler shown in Fig. 6.3(b). The coupler is placed vertically to save the space and a wideband ridge gap waveguide to rectangular waveguide transition is used to couple the power to the horizontal ridge gap waveguide plane. As shown in the previous section, the reflection-type phase shifter design starts with the choice of good parameters for the coupler.

As a result, the coupler is optimized in order to achieve wideband optimum performance in terms of the phase error and the power balance. The 3 dB hybrid is shown in Fig. 6.3(b), where two large slots of length  $l_{s1}$  are created symmetrically in a 0.5 mm thick metal sheet around the waveguide centerline with two short slots of length  $l_{s2}$  for reflection cancellation. The slots' and guides' dimensions are optimized to give a power balance of  $\pm 0.5$  dB from 28 to 39 GHz with phase error less than  $2^\circ$  over the whole band. The S-parameters of the coupler are shown in Fig. 6.4.

On the other hand, a good reconfigurable phase shifter should guarantee an equal phase shift within the frequency band of interest for the different states of the tuning element. To achieve this with the reflection-type phase shifter, the tuning element placed between the hybrid and the short circuit should present linear phase shift  $\varphi_x$  with frequency. Using a variable-height metallic post alone does not provide such a linear phase shift with frequency [126]. The circuit model of a variable-height metallic post inside a rectangular waveguide is mentioned in [136], as shown in Fig. 6.5 with no mathematical expressions for reactance values.

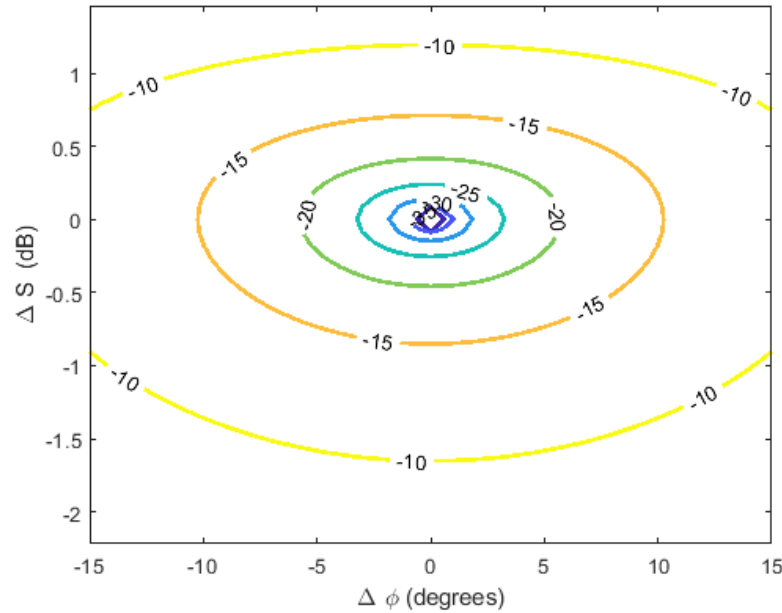
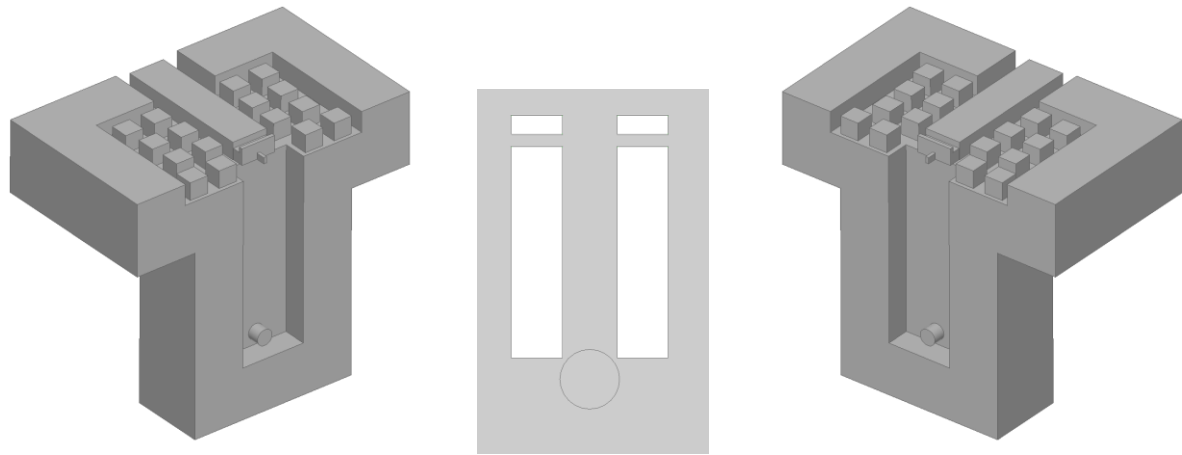
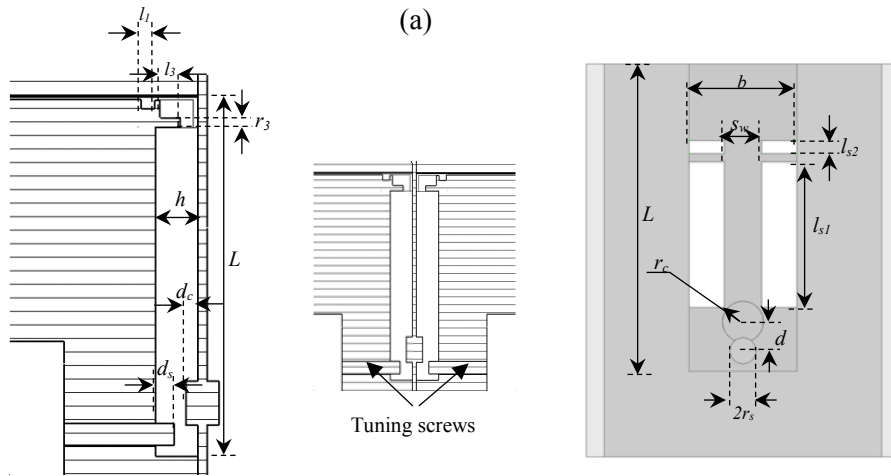


Fig. 6.2. Contour plot showing values of the reflection coefficient of the phase shifter of different phase and balance errors of the 90° hybrid.

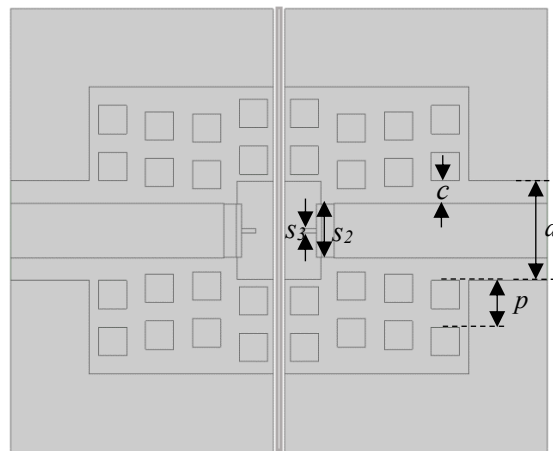
Instead, experimental values for the reactances for different heights at specific frequencies are shown in [136] and replicated here in Table 6.1 for two frequencies. To equalize the phase shift at different frequencies for different screw heights, a fixed height post of radius  $r_c$  and height  $d_c$  is used on both sides of the sheet in addition to two tuning screws of radius  $r_s$  passing through the upper and lower walls of the hybrid and having depth  $d_s$  inside the guide. The coupling between the two screws is to compensate for the phase shift introduced by their circuit models [136] and the shorted waveguide. The dimensions of the two screws are optimized for an equal phase shift  $\varphi_x$  on a wide frequency band while moving the screw. Fig. 6.6 shows the simulation used to optimize the screws' positions and dimensions with the resulting phase shift with and without the fixed height screw. After that, a wideband rectangular to ridge gap waveguide transition is designed in order to couple the power from the coupler ports to the ridge gap waveguide ports so that the reconfigurable phase shifter may be easily integrated with different RGW microwave devices in a larger system. The single-sided S-parameters of the RGW to rectangular waveguide transition are obtained using Ansoft ANSYS and shown in Fig. 6.7. It is shown that the transition provides return loss better than 15 dB from 28 GHz to 40 GHz. The values of all parameters of the reconfigurable phase shifter are provided in Table 6.2.



(a)



(b)



(c)

Fig. 6.3. Design geometry for the reconfigurable phase shifter. (a) Isometric view for one half of the phase shifter (b) Side cut of half the coupler (left), side cut of the coupler (middle) and front view of the coupler with dimensions. (c) Top view of the phase shifter.

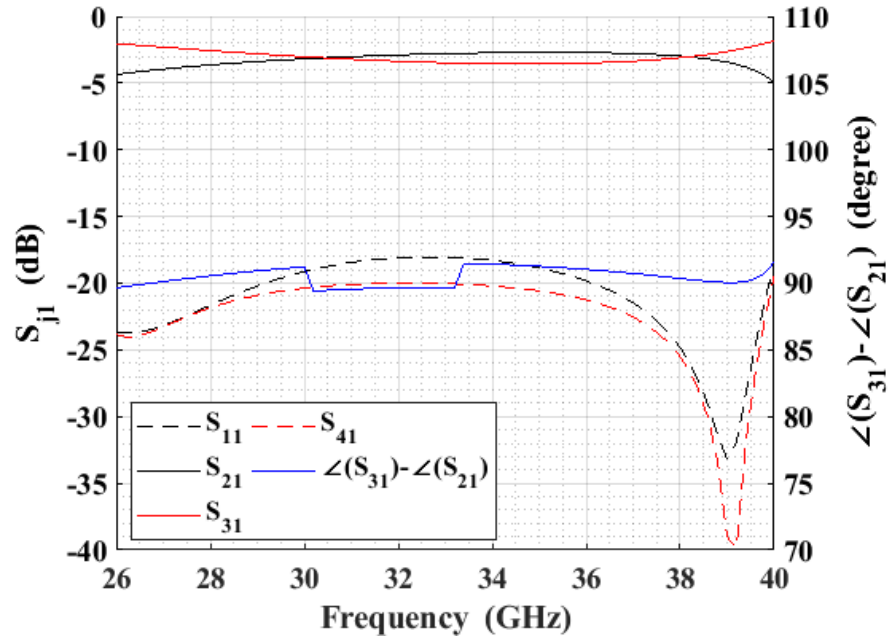


Fig. 6.4. S-parameters for the 4-port coupler without screws or short circuits.

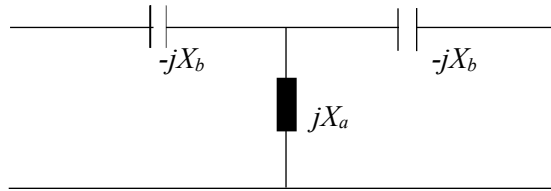


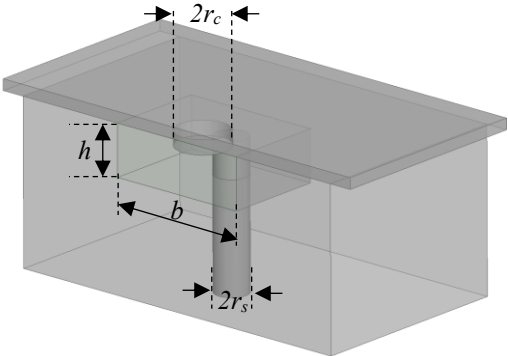
Fig. 6.5. Circuit model of a variable height screw inside a rectangular waveguide, according to [136].

Table 6.1: Values of different components in Fig. 6.5 at different screw heights as in [136].

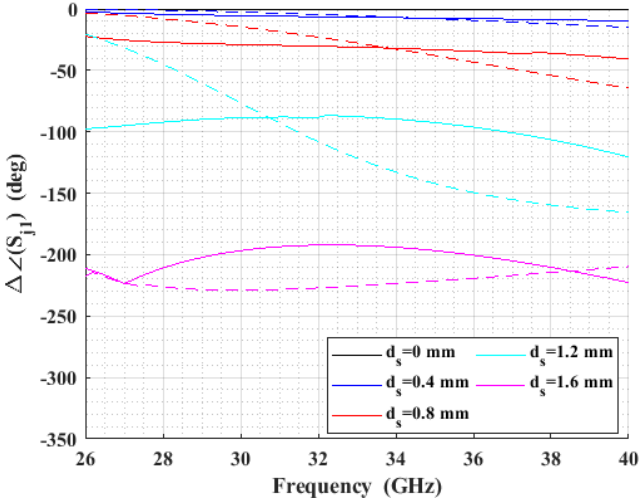
$r_s=1/32$ in., $\lambda=3.4$ cm					
$d_s/b$	0.249	0.497	0.746	0.921	1
$X_a/Z_o$	0.005	0.01	0.014	0.018	0.02
$X_b/Z_o$	-6.481	-1.015	-0.894	0.016	0.241
$r_s=1/32$ in., $\lambda=3.2$ cm					
$d_s/b$	0.254	0.505	0.756	0.943	1
$X_a/Z_o$	0.006	0.011	0.017	0.021	0.023
$X_b/Z_o$	-6.204	-0.906	-0.122	0.083	0.277

Finally, all the components of the phase shifter are put together to test its performance. The overall dimensions of the phase shifter are 15 mm x 30 mm x 25 mm. Two metallic screws are used to tune the phase shift. A question would be whether the sensitivity of the phase shift to the screw depth is suitable for a practical application. As a result, a parametric study on the phase shift

obtained for various screw depths is conducted, and its results are shown in Fig. 6.8. It is shown that the phase shifter provides an almost linear phase shift for different screw depths with an average slope of  $15^\circ / 0.1 \text{ mm}$ . The S-parameters of the reconfigurable phase shifter are obtained using ANSYS and verified using CST for different screw heights and shown in Fig. 6.9. The phase shifter has a return loss better than 13 dB from 28 GHz to 40 GHz, while the relative phase shift can change from  $0^\circ$  to  $200^\circ$  with phase error  $\pm 15^\circ$  from 28 GHz to 39 GHz. The overall bandwidth of the phase shifter is from 28 GHz to 39 GHz, which is 33% bandwidth.



(a)



(b)

Fig. 6.6. (a) Simulation setup to show the effect of adding a fixed height cylinder on the flat phase variation due to variable height screw. (b) Simulation of the phase difference between the transmitted signal for different heights of the screw and the transmitted signal for zero-height screw for two cases: with fixed height cylinder (solid) and without fixed height cylinder (dashed).

Table 6.2: Values of different parameters of reconfigurable phase shifter, according to Fig. 6.3 notation

Parameter	$h$	$b$	$r_s$	$r_c$	$L$	$l_{s1}$	$l_{s2}$	$d_c$	$l_1$	$l_2$	$l_3$
Value (mm)	2	6.3	0.61	1.2	18	8.5	0.75	1.8	0.75	0.4	1
Parameter	$s_1$	$s_2$	$s_3$	$a$	$p$	$c$	$s_w$	$d$	$r_1$	$r_2$	$r_3$
Value (mm)	3.5	3.4	0.3	2	3	1.45	2.2	1.7	1	1.5	0.5

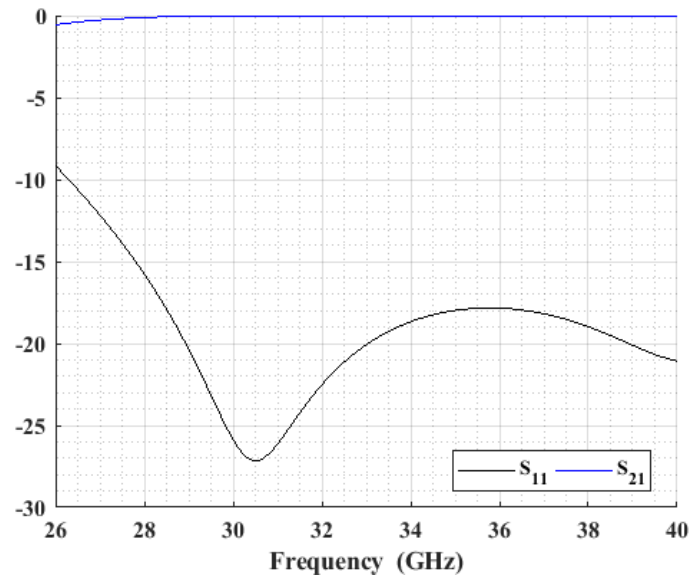


Fig. 6.7. Single-sided S-parameters of the RGW to rectangular waveguide transition generated using ANSYS.

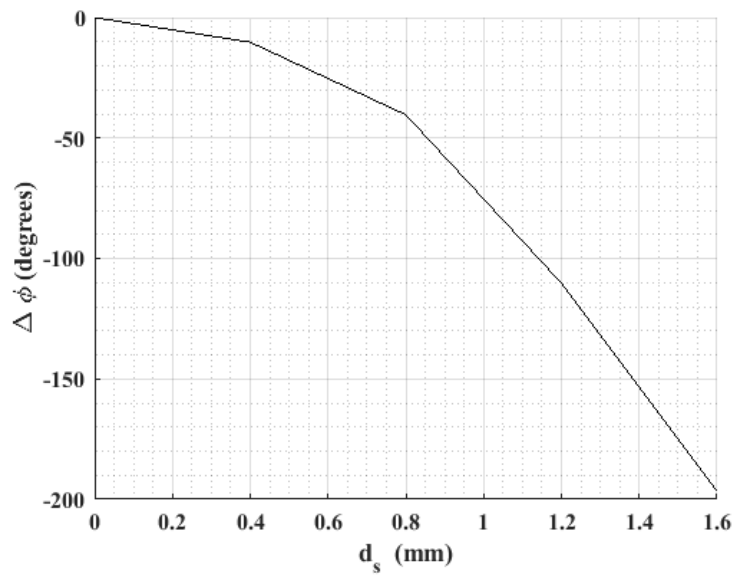
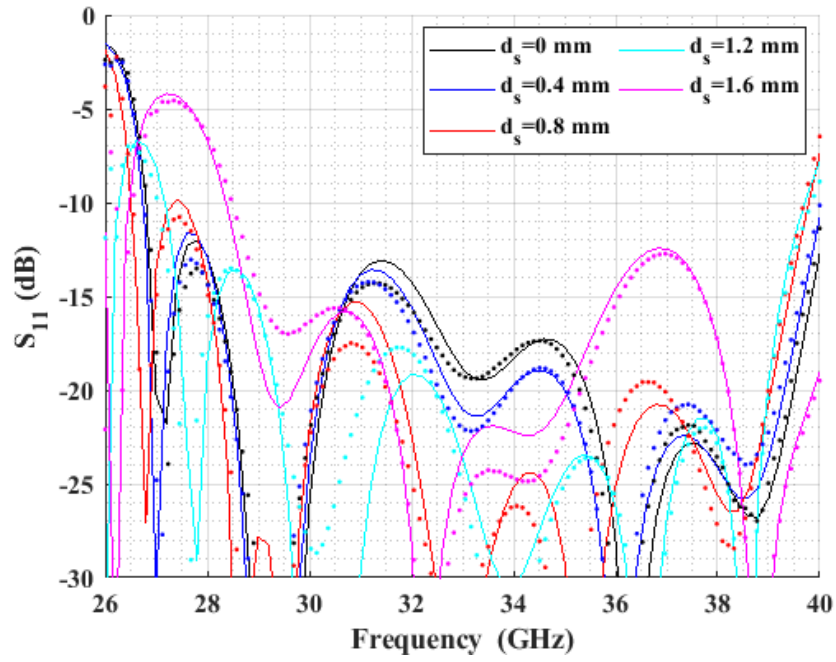
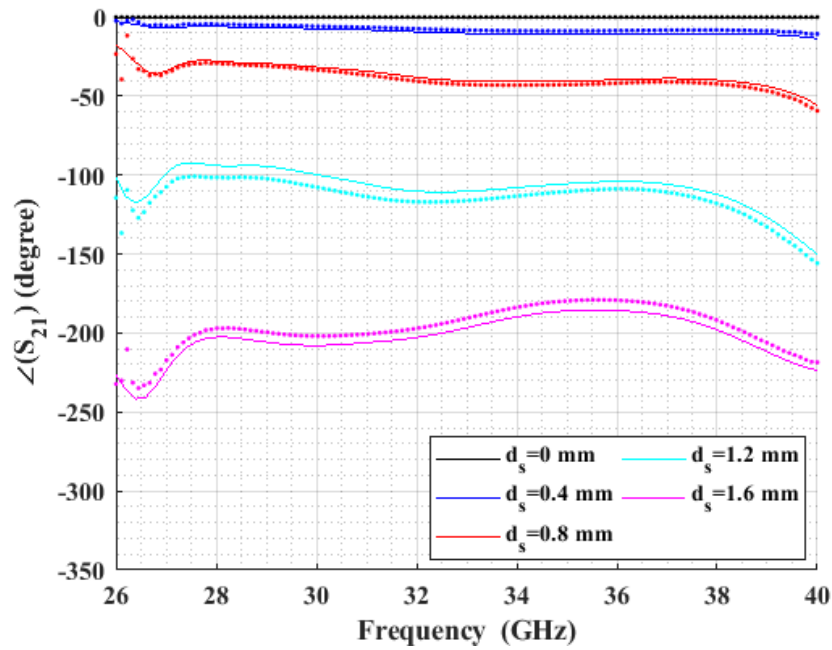


Fig. 6.8. Parametric study on the variation of the phase shift with different screw depths.



(a)



(b)

Fig. 6.9. Simulated S-parameters of the reconfigurable phase shifter obtained using ANSYS (line) and verified using CST (dotted) (a) Magnitude in dB (b) Phase in degrees.

# Chapter 7

## Butler Matrix Assembly and Results

In this chapter, the Butler matrix design and results are presented. First, an analysis of the expected performance of the Butler matrix under ideal circumstances is shown. Then, the basic Butler matrix is simulated and its S-parameters are shown to work on the Ka-band. After that, the S-parameter results of the reconfigurable part are presented to show the ability to configure the amplitude and phase distribution at the antenna ports.

### 7.1 Analysis of Proposed Butler Matrix

In this section, the proposed Butler matrix is analyzed to show its phase profile and orthogonality property. The topology is shown in Fig. 7.1 where inputs are denoted by  $I_1$  to  $I_4$ , intermediate stage outputs are denoted by  $A_1$  to  $A_4$ , while the final outputs are denoted  $O_1$  to  $O_8$ .

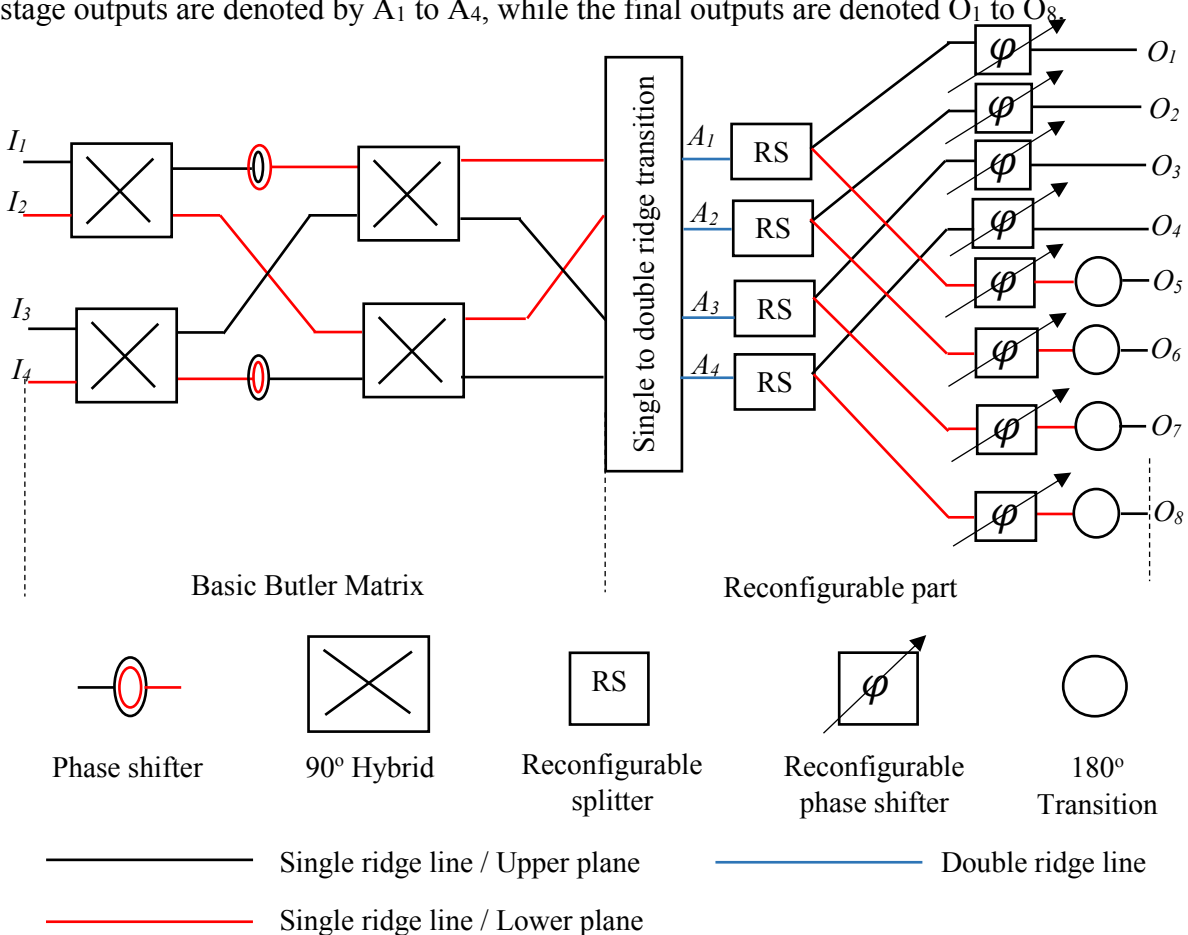


Fig. 7.1. Topology of the reconfigurable Butler matrix

Table 7.1 shows the different phases at nodes  $A_1$  to  $A_4$  and  $O_1$  to  $O_8$  for unity input power at inputs  $I_1$  to  $I_4$ , one at a time. It may be noted that for the intermediate nodes  $A_1$  to  $A_4$ , the progressive phase shifts for different inputs  $I_1$  to  $I_4$  are  $-45^\circ$ ,  $135^\circ$ ,  $-135^\circ$  and  $45^\circ$ , respectively. According to [8], the  $90^\circ$  difference between progressive phase shifts shows that the beams obtained are orthogonal. It is also expected that, for equal power splitting ratio, each output port will have one eighth of the input power at one input port. The  $180^\circ$  phase shift added to the outputs  $O_5$  to  $O_8$  keeps the same progressive phase shift achieved at the intermediate stage. This phase shift may be obtained by using  $180^\circ$  transition, as denoted in Fig. 7.1, cascading an extra reconfigurable phase shifter or by using  $180^\circ$  antenna feeding as in [137].

Table 7.1. Phases obtained at different nodes for single input excitation of the Butler matrix in Fig. 7.1.

	$A_1$	$A_2$	$A_3$	$A_4$	$O_1$	$O_2$	$O_3$	$O_4$	$O_5$	$O_6$	$O_7$	$O_8$
$I_1$	$-180^\circ$	$-225^\circ$	$-270^\circ$	$-315^\circ$	$-180^\circ$	$-225^\circ$	$-270^\circ$	$-315^\circ$	$0^\circ$	$-45^\circ$	$-90^\circ$	$-135^\circ$
$I_2$	$-90^\circ$	$-315^\circ$	$180^\circ$	$-45^\circ$	$-90^\circ$	$-315^\circ$	$180^\circ$	$-45^\circ$	$90^\circ$	$-135^\circ$	$0^\circ$	$135^\circ$
$I_3$	$-225^\circ$	$0^\circ$	$135^\circ$	$-90^\circ$	$-225^\circ$	$0^\circ$	$135^\circ$	$-90^\circ$	$-45^\circ$	$-180^\circ$	$315^\circ$	$90^\circ$
$I_4$	$-135^\circ$	$-90^\circ$	$-45^\circ$	$0^\circ$	$-135^\circ$	$-90^\circ$	$-45^\circ$	$0^\circ$	$45^\circ$	$90^\circ$	$135^\circ$	$180^\circ$

## 7.2 Basic Butler Matrix

The basic Butler matrix is shown in Fig. 7.2, where four couplers and 2 dual-plane phase shifters are used. The 3-dB coupler in Chapter 5 is shifted up in frequency, and its parameters are modified such that the return loss and isolation are better than 30 dB from 28 GHz to 38 GHz (33% bandwidth). The parameters of the new coupler are shown in Table 7.2, and its S-parameters are shown in Fig. 7.3. It is shown that the magnitude error is  $\pm 1$  dB on the whole band. The dual-plane phase shifter used here belongs to a family of phase shifters introduced in several papers [17], [18], [19] where a geometric shape is used to form the transition element between the upper and lower planes. The phase shifter is shown in Fig. 7.4, where an elliptical slot and two elliptically shaped ridges are used to create a relative phase shift of  $135^\circ$  between two lines 1 and 2 (or 3 and 4). The S-parameters of the phase shifter are shown in Fig. 7.5, along with the relative phase shift between the two ports. Return loss is better than 10 dB from 30 GHz to 37.5 GHz, while phase

difference is equal  $135^\circ \pm 5^\circ$ . The dimensions of the phase shifter are shown in Table 7.3.

Table 7.2. Parameters of the coupler working in the Ka-band (28 GHz to 38 GHz) (following Fig.5.1 notation for slots and Fig. 1.6 notation for RGW)

Parameter	$s$	$c$	$p$	$a$	$r$	$b$	$g$	$s_l$	$s_{ls}$	$s_w$	$s_{ws}$
Value (mm)	1.9	1.9	3	2	1.24	1.9	0.3	8.4	0.48	1.9	0.85

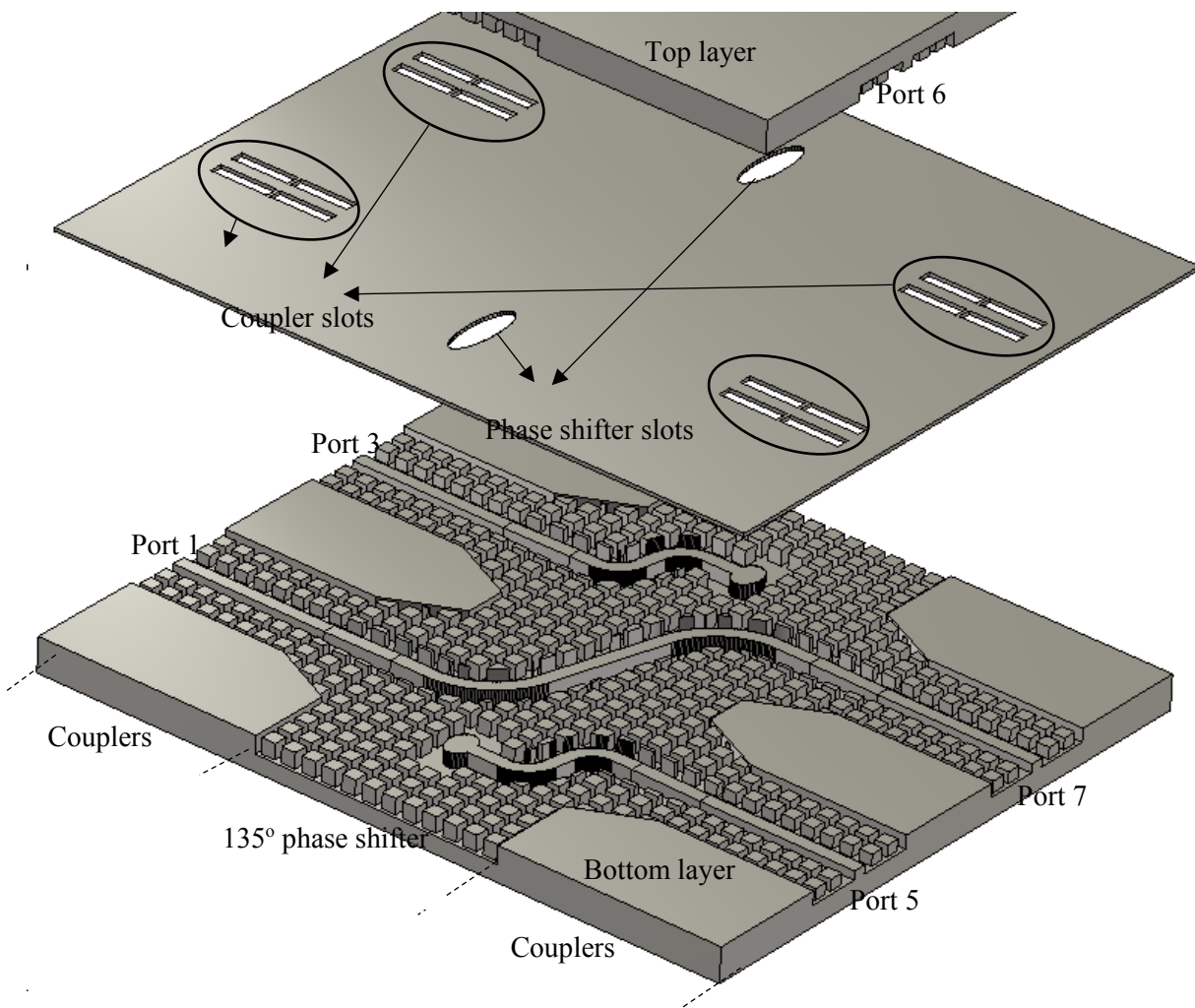


Fig. 7.2. 3D exploded view of the basic Butler matrix with the details of the bottom layer and the middle sheet shown.

Finally, the resulting S-parameters of the Basic Butler matrix are produced in Fig. 7.6 (a-c) using ANSYS and verified using CST. The return losses are shown to be below 15 dB from 29 GHz to

37.5 GHz, and transmission S-parameters are  $6 \pm 1.5$  dB between an input port and the four output ports. Transmission phases shown in Fig. 7.6(c) are for input from port 1 ( corresponds to  $I_3$  in Fig. 7.1) and have  $-135^\circ$  progressive phase shifts between the ports 5, 7, 6 and 8, respectively. By simulating other input ports, it is deduced that a  $90^\circ$  phase difference exists between different progressive phase shifts generated due to different input ports.

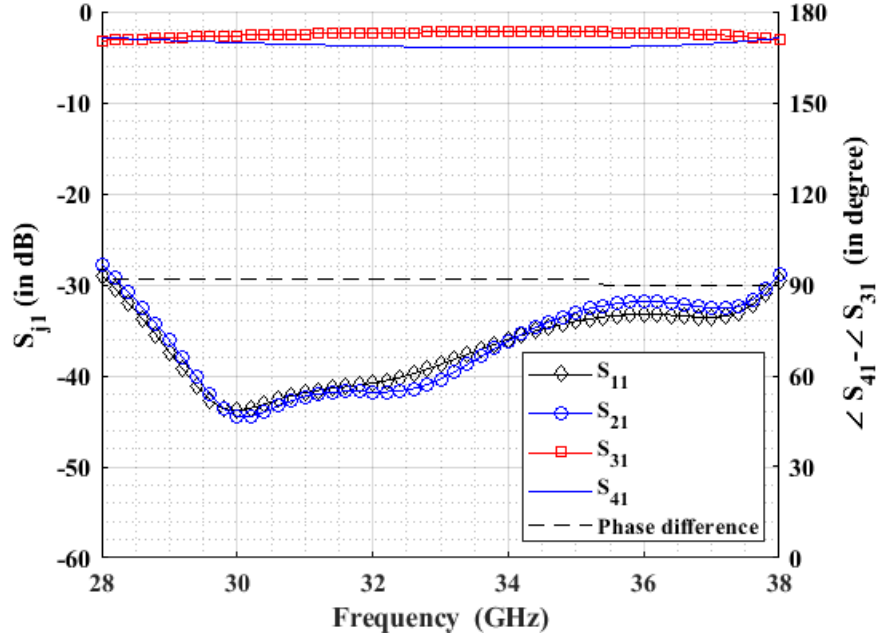


Fig. 7.3. S-parameters of the coupler.

## 7.3 Reconfigurable Part

The reconfigurable part of the Butler matrix is shown in Fig. 7.7. It starts by routing the output signals from the basic Butler matrix to reach a single-ridge to double-ridge transition. After that, the reconfigurable splitter is used to split the signal in each of the 4 DRGW waveguides into two parts producing 8 RGW ports. Signals in each RGW is routed through the bed of nails to a reconfigurable phase shifter. The return losses (in dB) of the reconfigurable part are shown in Fig. 7.8 (a) for equal power splitting case (deflection = 0 mm) with equal phase shift and Fig. 7.8 (b) for unequal power splitting case ((Output power ratios are 0.01, 0.36, 1.75, 1.96, 1.96, 1.75, 0.36, 0.01), sheets deflections needed are 0.2 and 0.12 mm) with unequal phase shifts ( $30^\circ, 20^\circ, 10^\circ, 0^\circ, 0^\circ, 10^\circ, 20^\circ, 30^\circ$ ) using screw positions 0.64, 0.5, 0.36, and 0 mm.

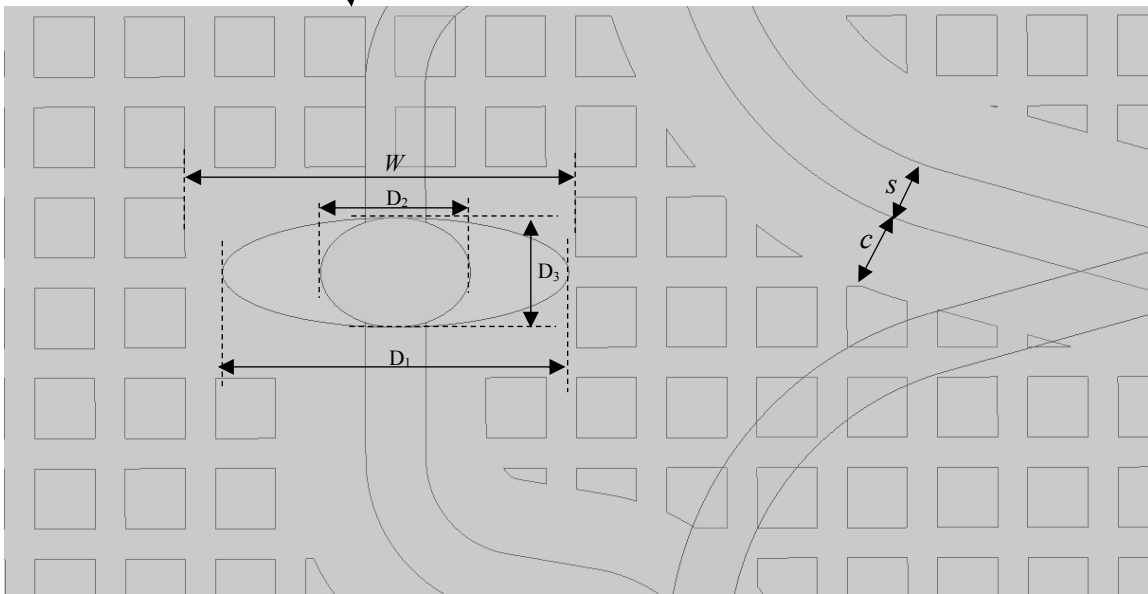
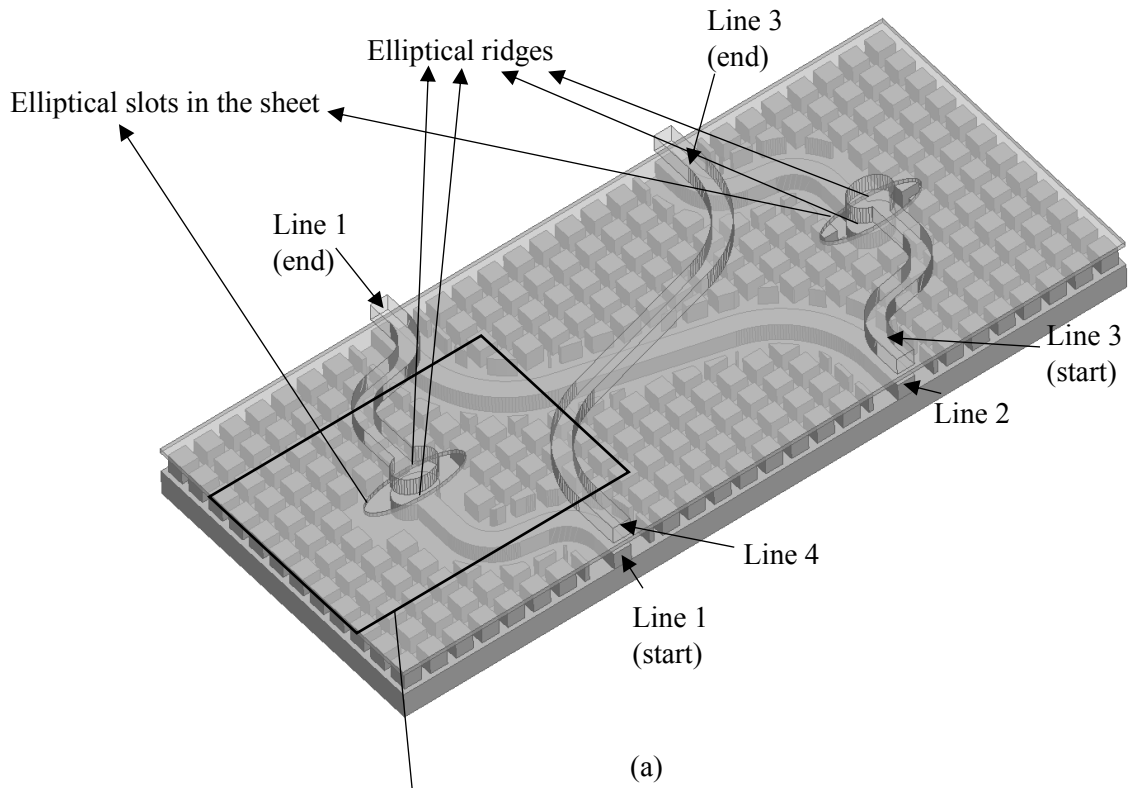


Fig. 7.4. Design of the 135° phase shifter working on the Ka-band showing different design parameters. (a) Phase shifter structure with transparent sheet and ridges of the upper half (upper pins and plate removed) (b) Closer look at the phase shifter dimensions.

Table 7.3. Parameters of the phase shifter in Fig. 7.4.

Parameter	$s$	$c$	$b$	$r$	$p$	$a$	$W$	$D_1$	$D_2$	$D_3$
Value (mm)	2	2.5	2.5	2	3	2	13	11.5	5	3.6

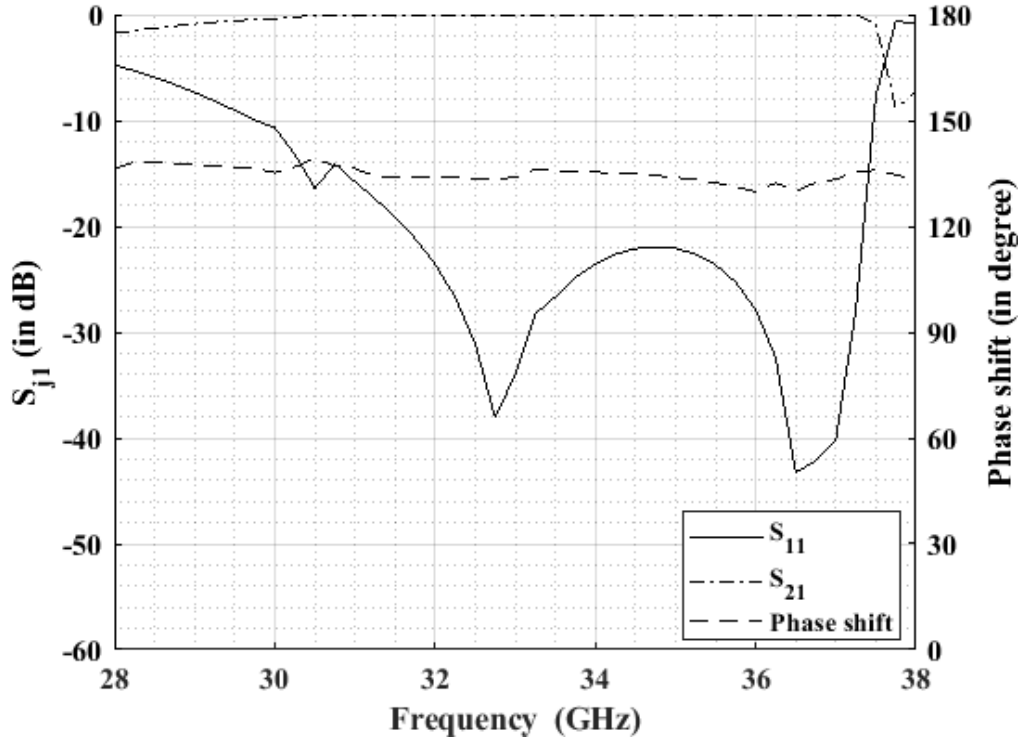
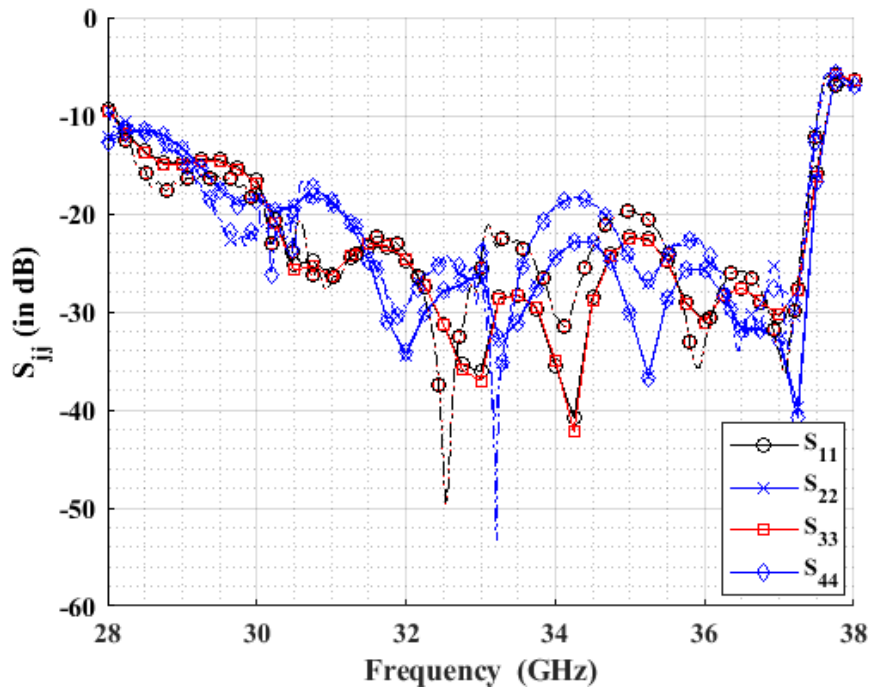
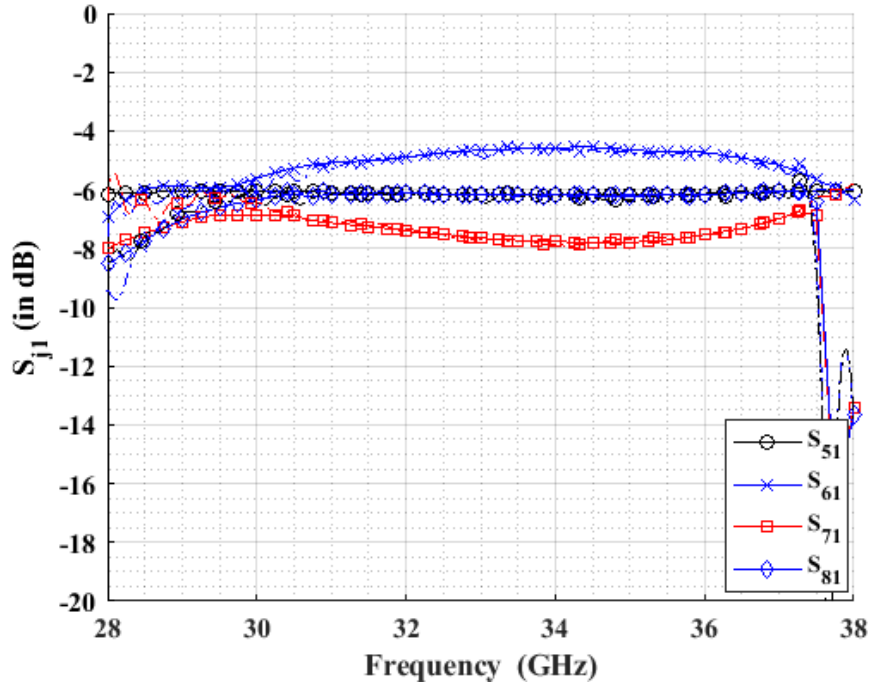


Fig. 7.5. S-parameters of the 135° phase shifter.

It is shown in Fig 7.8 that the return loss of the reconfigurable part is better than 10 dB from 28 GHz to 37.5 GHz for the two states except around 32 GHz where return loss is better than 8 dB. The transmission coefficients between different ports are shown in Fig. 7.9 (magnitude) and Fig. 7.10 (phase). Fig. 7.9 shows that the change in the transmission coefficients magnitudes is within 2 dB for all the cases. It is shown in Fig. 7.10 that different phase shifts may be obtained using different tuning states for the phase shifter. The two states simulated here will be used with other states in the next section to present the capabilities of the Butler matrix to produce different radiation patterns. Fig. 4.15 and Fig. 6.8 may be used to decide the appropriate splitter deflections and appropriate screw depths for the phase shifters.

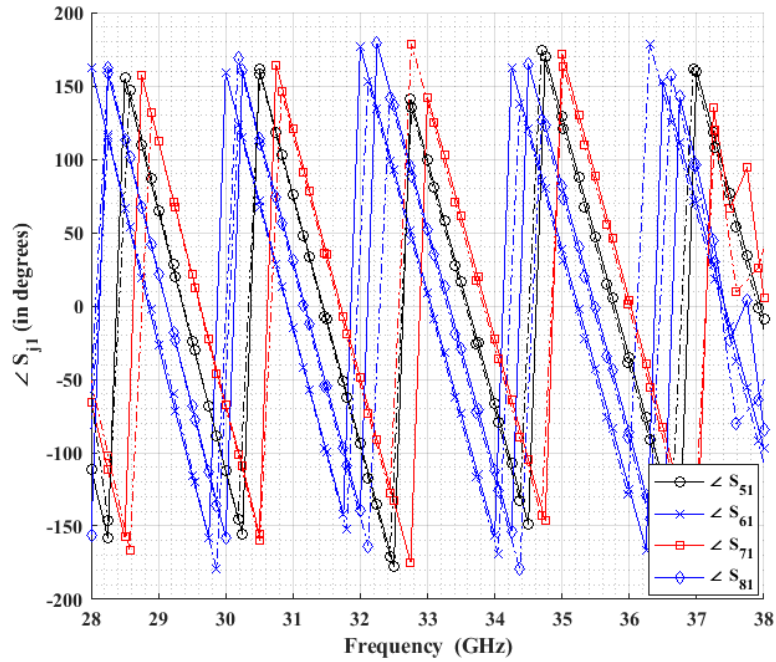


(a)



(b)

Fig. 7.6. S-parameters of the basic Butler matrix (ANSYS line, CST dash-dot) (a) Return loss (b) Transmission.



(c)

Fig. 7.6. S-parameters of the basic Butler matrix (ANSYS line, CST dash-dot) (c) Phase.

After that, ADS, a commercial circuit simulator, is used to connect the basic Butler matrix and the reconfigurable part for the two cases presented above. Fig. 7.11 shows the schematic used to check the S-parameters of the entire Butler matrix. Fig. 7.12 shows the return loss and transmission S-parameters of the Butler matrix in the case of equal phase shift and equal power. It is shown that the return loss of the entire Butler matrix is better than 10 dB from 28 GHz to 37.5 GHz, while the transmission coefficients are  $9 \pm 1.5$  dB, which shows 6 dB decrease from Fig. 7.9 (a). The 6 dB decrease is due to having the input port of Fig. 7.12 at the input of the basic Butler matrix rather than at the input of the reconfigurable part, as in Fig. 7.9.

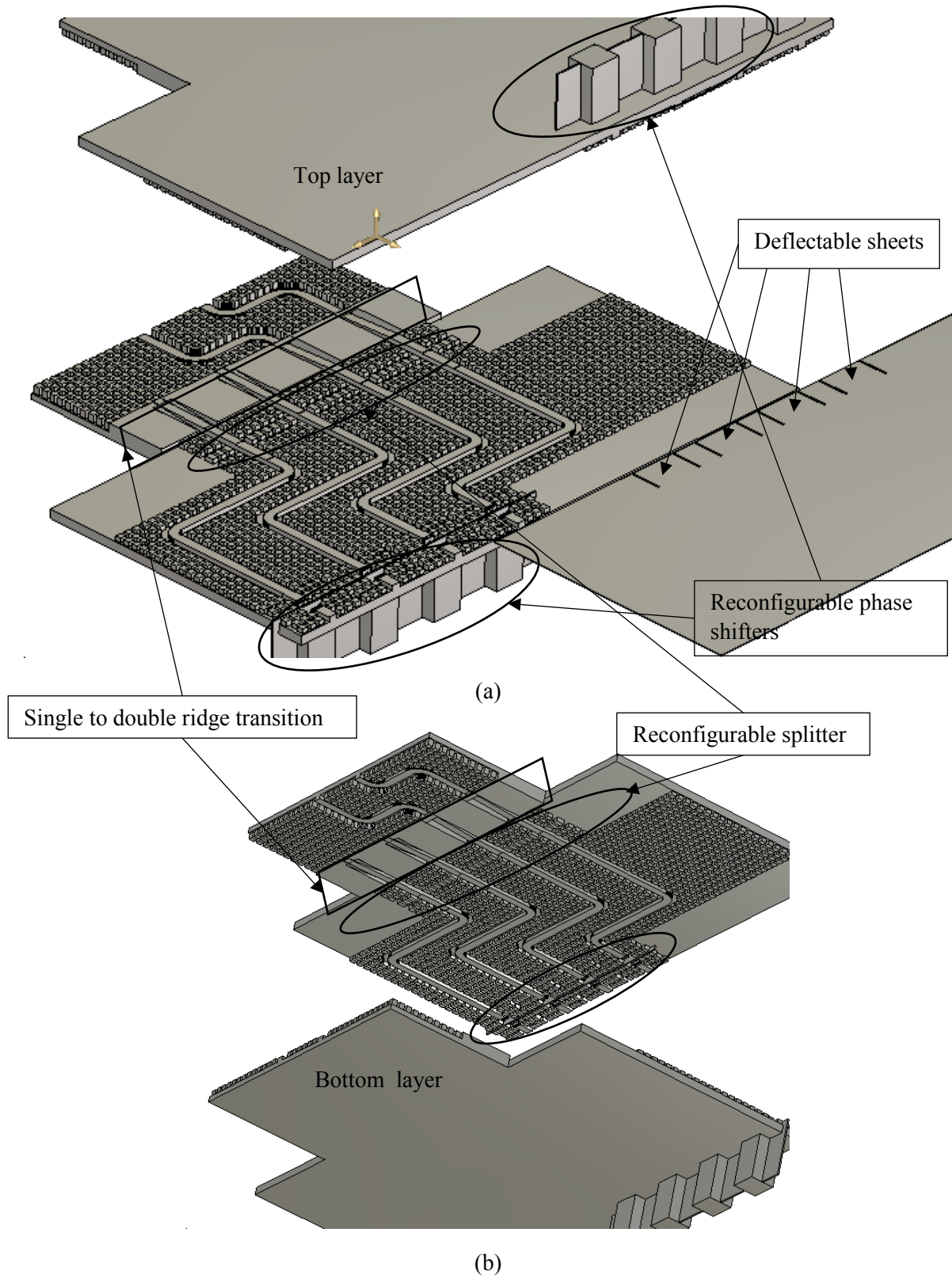
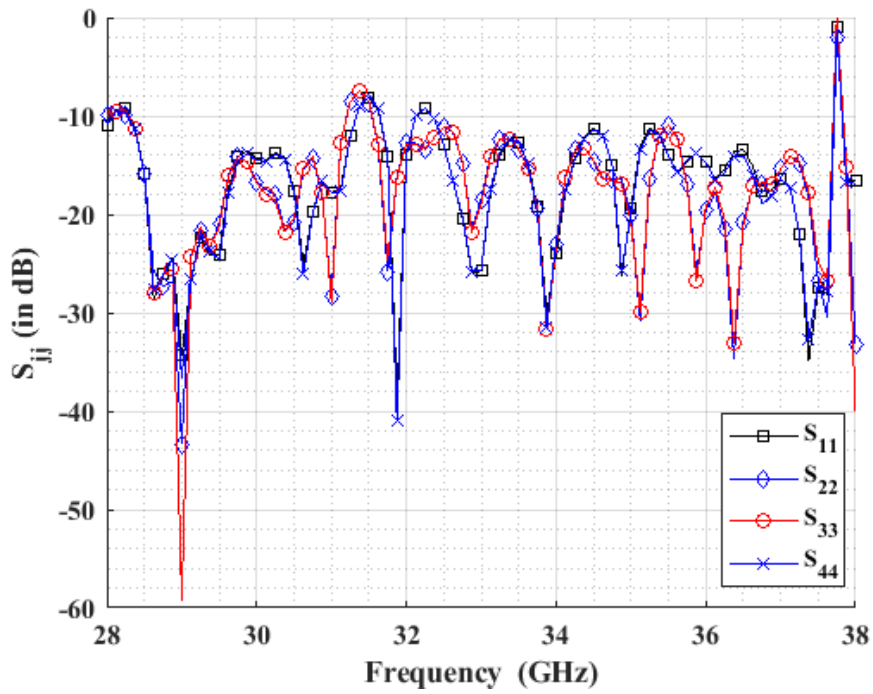
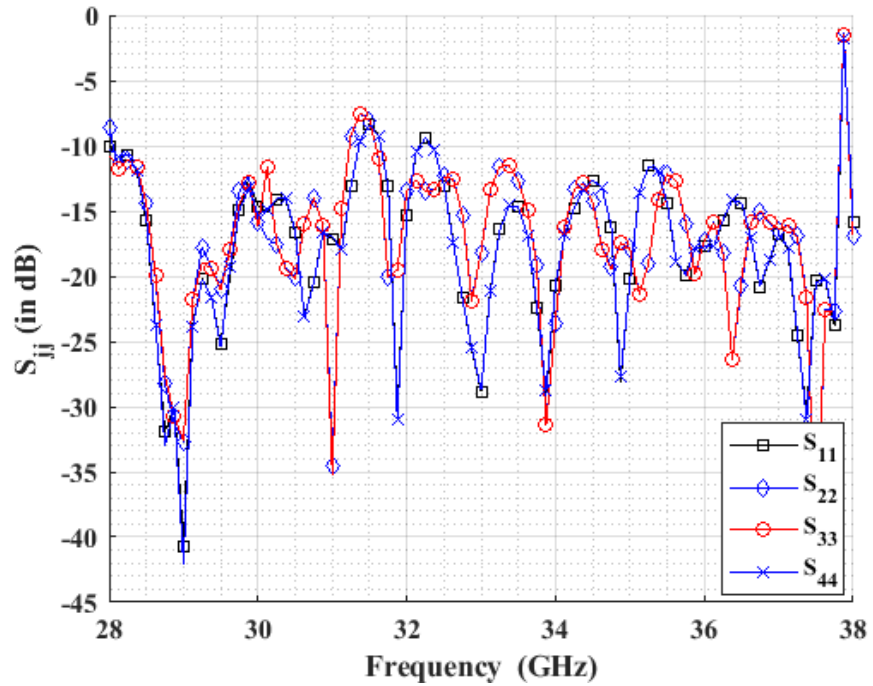


Fig. 7.7. Design of the reconfigurable part of Butler matrix. (a) 3D exploded view showing bottom layer details looking from top with middle sheet exposed. (b) 3D exploded view showing top layer details looking from bottom.

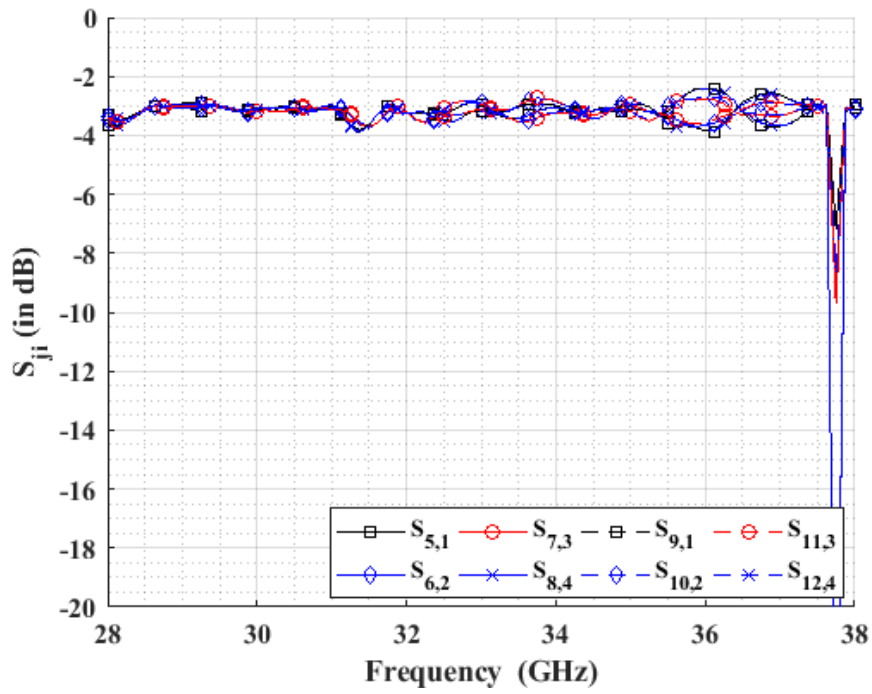


(a)

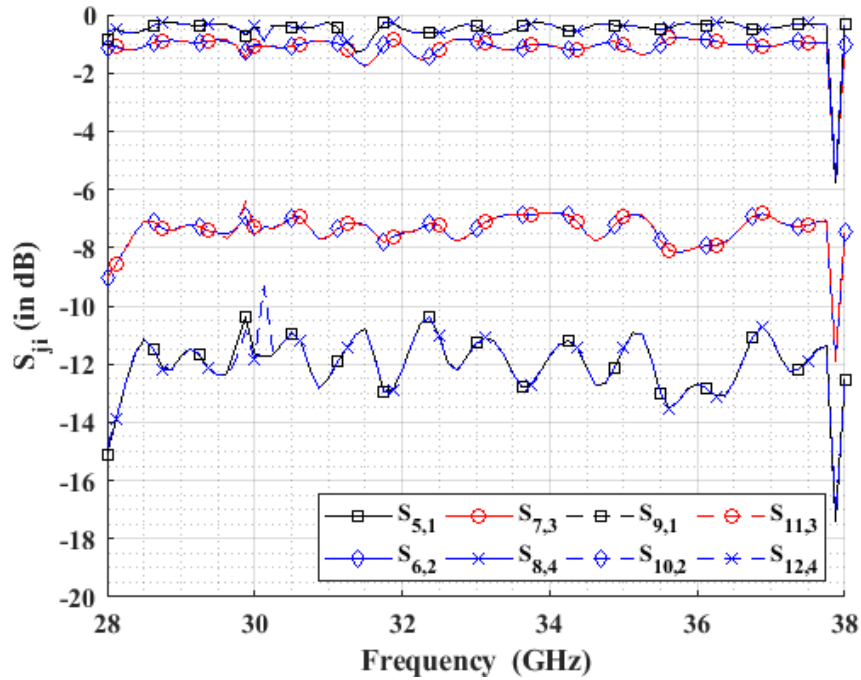


(b)

Fig. 7.8. Return loss at 1 input port of the reconfigurable part in 2 different cases (a) Equal power splitting (b) Unequal power splitting.

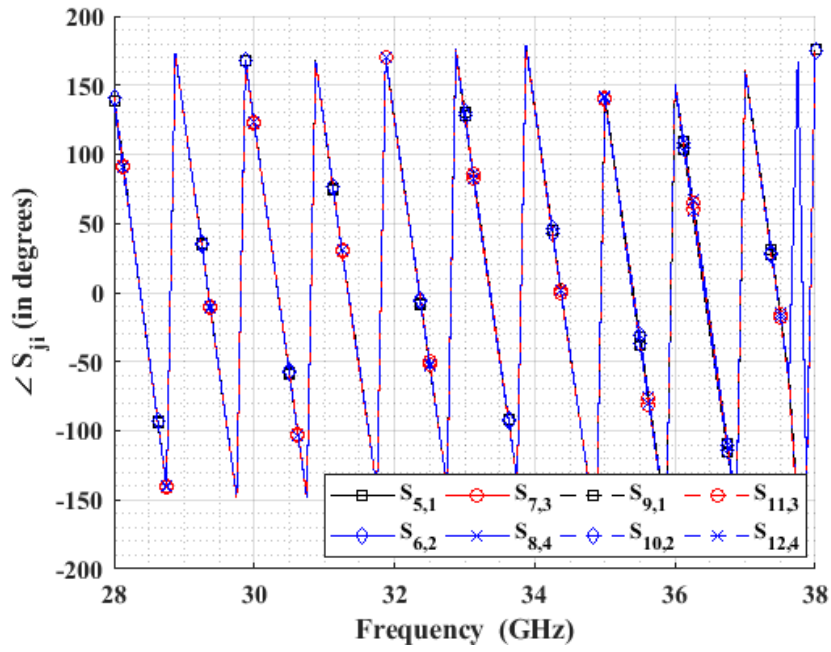


(a)

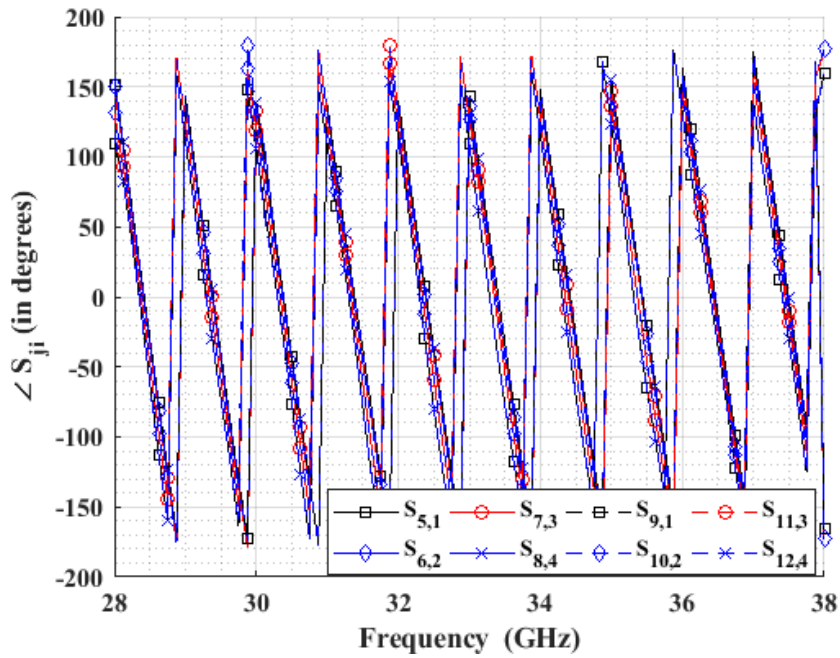


(b)

Fig. 7.9. Transmission coefficients in dB at different output ports for the two cases (a) equal power splitting at all ports (b) unequal splitting.



(a)



(b)

Fig. 7.10. Transmission coefficients in degrees at different output ports for the two cases (a) equal power splitting at all ports (b) unequal splitting at 2 ports.

Fig. 7.13 shows the return loss and transmission S-parameters of the Butler matrix in the case of unequal phase shift (Phase shifts are  $30^\circ$ ,  $20^\circ$ ,  $10^\circ$ ,  $0^\circ$ ,  $0^\circ$ ,  $10^\circ$ ,  $20^\circ$ ,  $30^\circ$ ), and unequal power splitting (Output power ratios are 0.01,0.36,1.75,1.96,1.96,1.75,0.36,0.01). It is shown that return loss of the entire Butler matrix is better than 10 dB from 28 GHz to 37.5 GHz, while the transmission coefficients show a 6 dB decrease from Fig. 7.9 (b). The change in the transmission coefficient with the frequency is within 2 dB. The deviation in the values of some S-parameters in Fig. 7.13 from the intended (ideal) power levels is due to the errors introduced by non-ideal components in addition to using the dB scale, which amplifies the errors in the lower power values than higher power values.

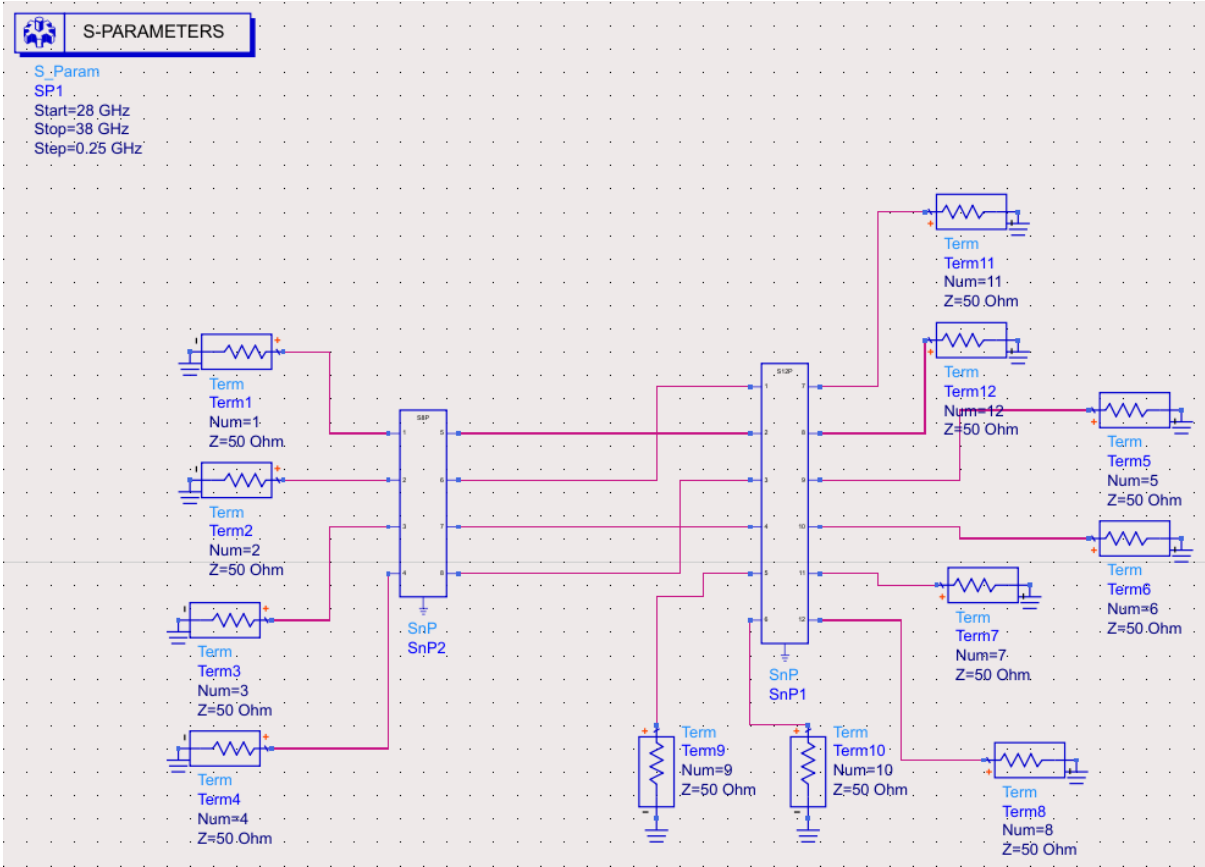
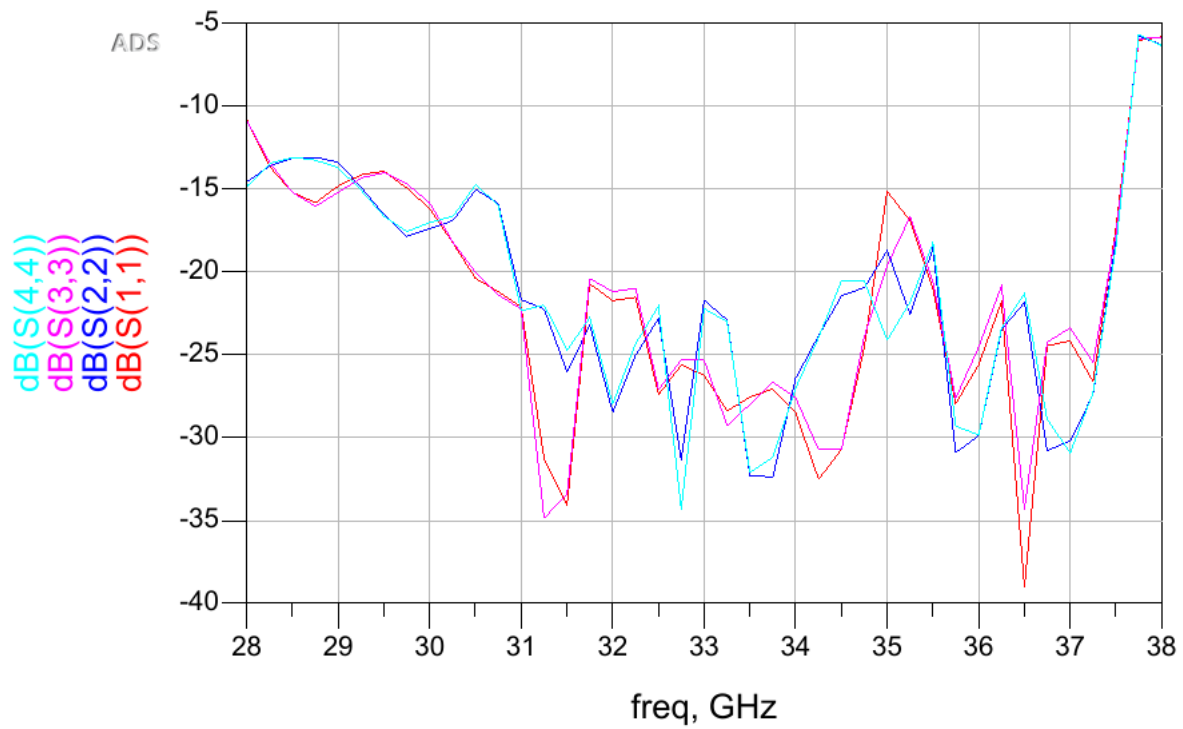
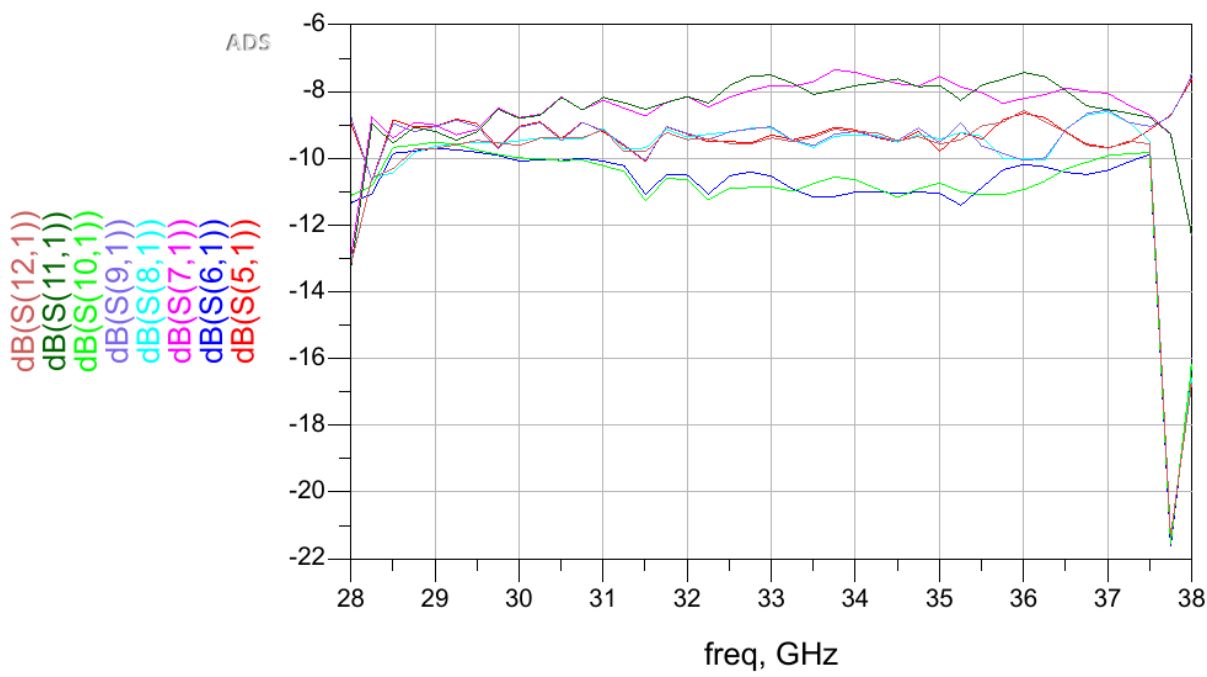


Fig. 7.11. ADS schematic to show the assembly of full Butler matrix as building blocks.

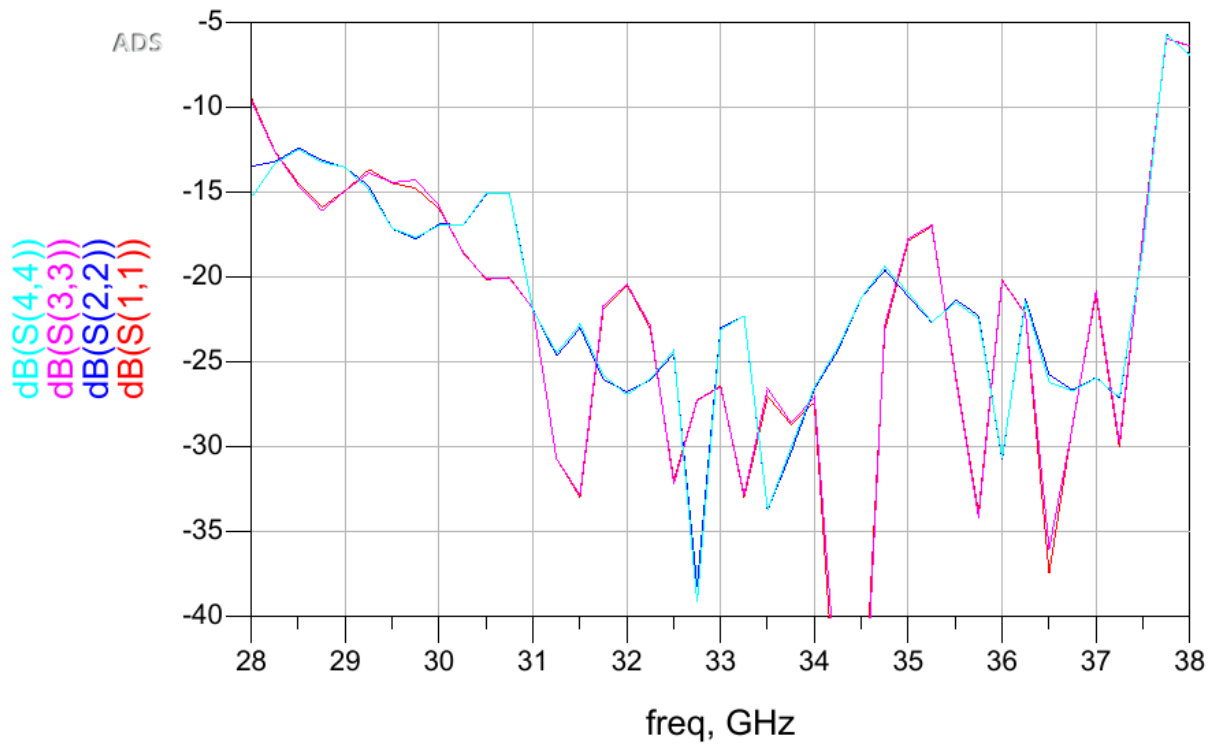


(a)

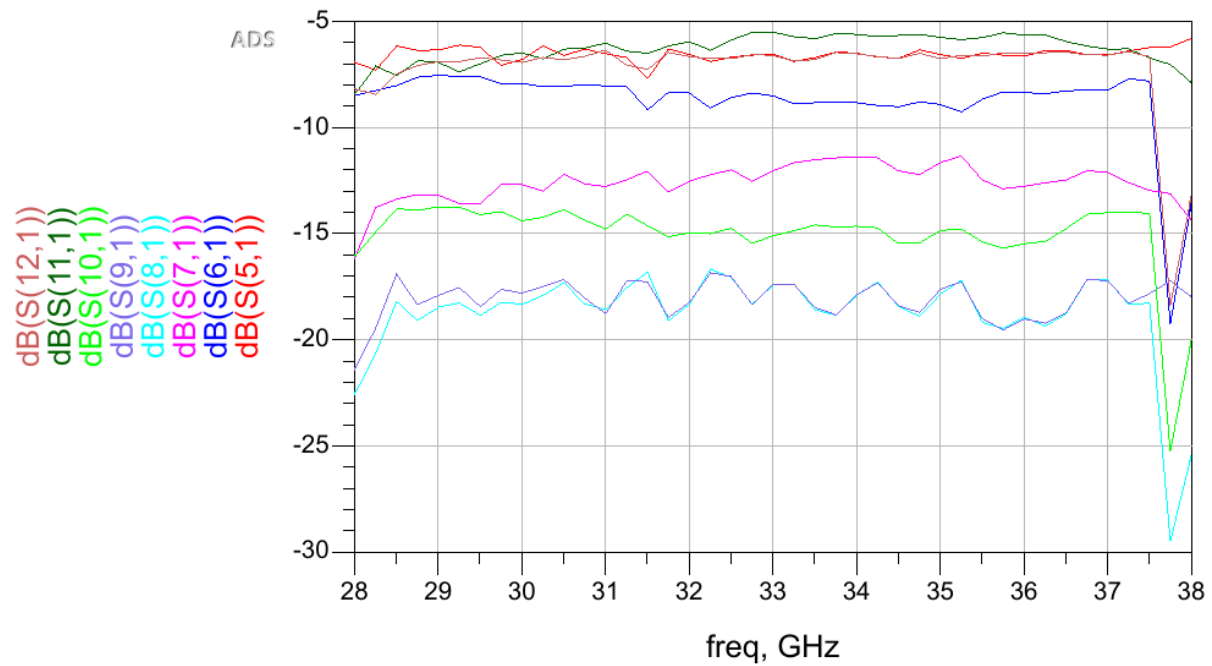


(b)

Fig. 7.12. S-parameters of the Butler matrix in the case of pattern 1 configuration (a) Return loss (b) Transmission S-parameters in dB.



(a)



(b)

Fig. 7.13. S-parameters of the Butler matrix in the case pattern 3 configuration. (a) Return loss (b) Transmission S-parameters in dB.

## 7.4 Capabilities of Tunable Butler matrix

The proposed Butler matrix can provide controllable beamwidth, gain, and beam directions. Beam directions may be controlled by progressively increasing the phase shift of the output ports of the Butler matrix using the reconfigurable phase shifter. Since the maximum phase shift obtained using the reconfigurable phase shifter is  $200^\circ$ , the maximum change in the direction of each beam is equal to  $25^\circ$  for each additional reconfigurable phase shifter.

A study on the characteristics of current amplitudes that may be generated from the tunable Butler matrix is presented next to show control of the radiation pattern. Fig. 7.14 shows the reconfigurable Butler matrix part of Fig. 7.1, where the current amplitudes at the outputs of the basic Butler matrix are assumed equal to  $A_1$  to  $A_4$ , while the current amplitudes due to splitting are denoted by symbols  $O_1$  to  $O_8$  with phases  $\phi_1$  to  $\phi_8$ . Since basic Butler matrix has equal amplitude outputs (where  $A_1 = A_2 = A_3 = A_4$ ), the following equation applies:

$$A_1^2 = O_1^2 + O_5^2 = O_2^2 + O_6^2 = O_3^2 + O_7^2 = O_4^2 + O_8^2 \quad (7.1)$$

Taking (7.1) in consideration and assuming symmetric amplitude distribution pattern ( $O_n = O_{9-n}$ ;  $n=1:4$ ), the ability to control the aperture distribution is investigated by obtaining several array factors and plotting their radiation patterns for variable beamwidth/gain assuming that antenna spacing is  $0.5 \lambda$  at 33 GHz (which is the middle of the band). The result of this

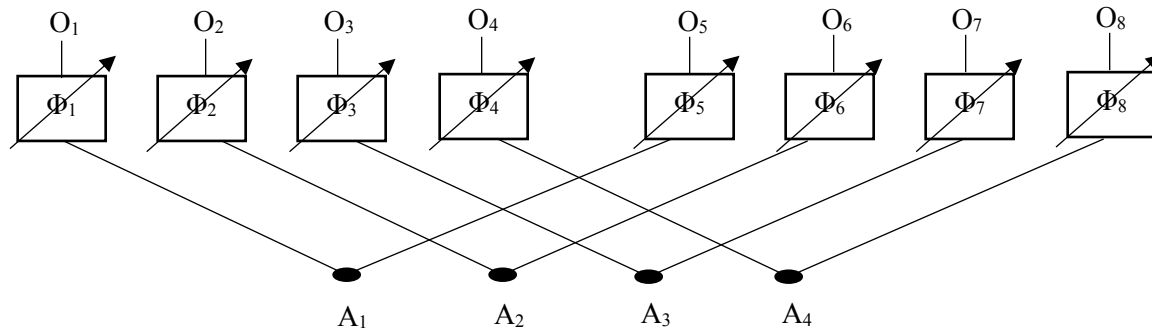


Fig. 7.14. Schematic of the relative phase shift and power distribution for the  $1 \times 8$  antenna array fed by Butler matrix

Table 7.4. Different splitting ratios and phase shifts at different antenna ports.

Parameter		O <sub>1</sub>	O <sub>2</sub>	O <sub>3</sub>	O <sub>4</sub>	Φ <sub>1</sub>	Φ <sub>2</sub>	Φ <sub>3</sub>	Φ <sub>4</sub>	Φ <sub>5</sub>	Φ <sub>6</sub>	Φ <sub>7</sub>	Φ <sub>8</sub>
Pattern 1	Current ratio	1	1	1	1	0	0	0	0	0	0	0	0
	dB (-ve)	9	9	9	9								
Pattern 2	Current ratio	0.45	0.77	1.18	1.34	0	0	0	0	0	0	0	0
	dB (-ve)	16	11.2	7.5	6.5								
Pattern 3	Current ratio	0.1	0.6	1.3	1.4	30	20	10	0	0	10	20	30
	dB (-ve)	28	13.5	6.8	6.02								
Pattern 4	Current ratio	0	0	1.42	1.42	-	-	0	0	0	0	-	-
	dB (-ve)	Inf	Inf	6	6								
Pattern 5	Current ratio	0.6	0.87	1.1	1.3	120	90	30	0	0	30	90	120
	dB (-ve)	13.5	14	8.1	6.8								
Pattern 6	Current ratio	0.34	1.12	0.86	1.38	0	0	40	115	115	40	0	0
	dB (-ve)	18.4	8	10.3	6.3								
Pattern 7	Current ratio	0	0	1.42	1.42	-	-	0	105	105	0	-	-
	dB (-ve)	Inf	Inf	6	6								

investigation is shown in Fig. 7.15 (a-c), where three different element spacing ( $0.4 \lambda$ ,  $0.5 \lambda$ , and  $0.6 \lambda$ ) are assumed and their radiation patterns are plotted. This estimates the performance of the same antenna array from 28 GHz ( $0.42 \lambda$ ) to 37 GHz ( $0.56 \lambda$ ). The 3-dB beamwidths (and maximum directivities) of Fig. 7.15 (a) are  $18^\circ$ ,  $20^\circ$ ,  $24.6^\circ$ ,  $33^\circ$ ,  $60^\circ$ ,  $76^\circ$  and  $180^\circ$  (18 dB, 17.5 dB, 16.5 dB, 15 dB, 14.8 dB, 13.5 dB, and 10.7 dB), while the beamwidths (and maximum directivities) of Fig. 7.15 (b) are  $12.6^\circ$ ,  $15.6^\circ$ ,  $20^\circ$ ,  $26^\circ$ ,  $30^\circ$ ,  $60^\circ$ , and  $110^\circ$  (18 dB, 17.5 dB, 16.5 dB, 15 dB, 14.8 dB, 13.5 dB, and 10.7 dB). Fig. 7.15(c) shows that the 3-dB beamwidths (and maximum directivities) are  $10^\circ$ ,  $13^\circ$ ,  $16^\circ$ ,  $26^\circ$ ,  $30^\circ$ ,  $50^\circ$ , and  $90^\circ$  (18 dB, 17.5 dB, 16.5 dB, 15 dB,

14.8 dB, 13.5 dB, and 10.7 dB). The side lobes at the endfire direction in Fig. 7.15(c) may be avoided by choosing an antenna element that suppresses radiation at  $\theta_{\text{elevation}} < 30^\circ$ . Table 7.4 shows the required amplitude distribution, and phase shifts needed to obtain array factors in Fig. 7.15 (a, b). The dB values in the table are calculated as S-parameters for the full Butler matrix. Table 7.5 shows sheet's maximum deflection values of the reconfigurable splitter and screw depths of the reconfigurable phase shifters to obtain the values in Table 7.4.

Table 7.5. Screw depths and sheet deflections (in mm) needed to achieve values in Table 7.4.

Parameter	Deflection $O_{1,4}$	Deflection $O_{2,3}$	Depth $\Phi_{1,8}$	Depth $\Phi_{2,7}$	Depth $\Phi_{3,6}$	Depth $\Phi_{4,5}$
Pattern 1	0	0	0	0	0	0
Pattern 2	0.16	0.07	0	0	0	0
Pattern 3	0.2	0.12	0.64	0.5	0.36	0
Pattern 4	0.2	0.2	-	-	0	0
Pattern 5	0.12	0.05	1.24	1.1	0.64	0
Pattern 6	0.18	-0.05	0	0	0.8	1.2
Pattern 7	0.2	0.2	-	-	0.8	1.36

Fig. 7.16, 7.17 and 7.18 show a study on the radiation pattern that may be obtained from the full Butler matrix with isotropic antennas of different separations. Fig. 7.16 (a-c) shows that the output beams of the Butler matrix can be scanned to the right as a result of a  $25^\circ$  progressive phase shift introduced by the reconfigurable phase shifters. As mentioned for Fig. 7.15, if the spacing between antennas is chosen to be  $0.5 \lambda$  at the center frequency, the same physical spacing will represent  $0.4 \lambda$  at 28 GHz and  $0.6 \lambda$  at 38 GHz. The value of the scanning angle is around  $3^\circ \pm 0.5^\circ$  for all these frequencies. It can also be noticed in Fig. 7.16 that the beam crossover level is more than 20 dB below the peak directivity of the beams (which is 18 dB). Different beam crossover levels may be achieved if other patterns are used. Fig. 7.17 shows that the beam crossover level is

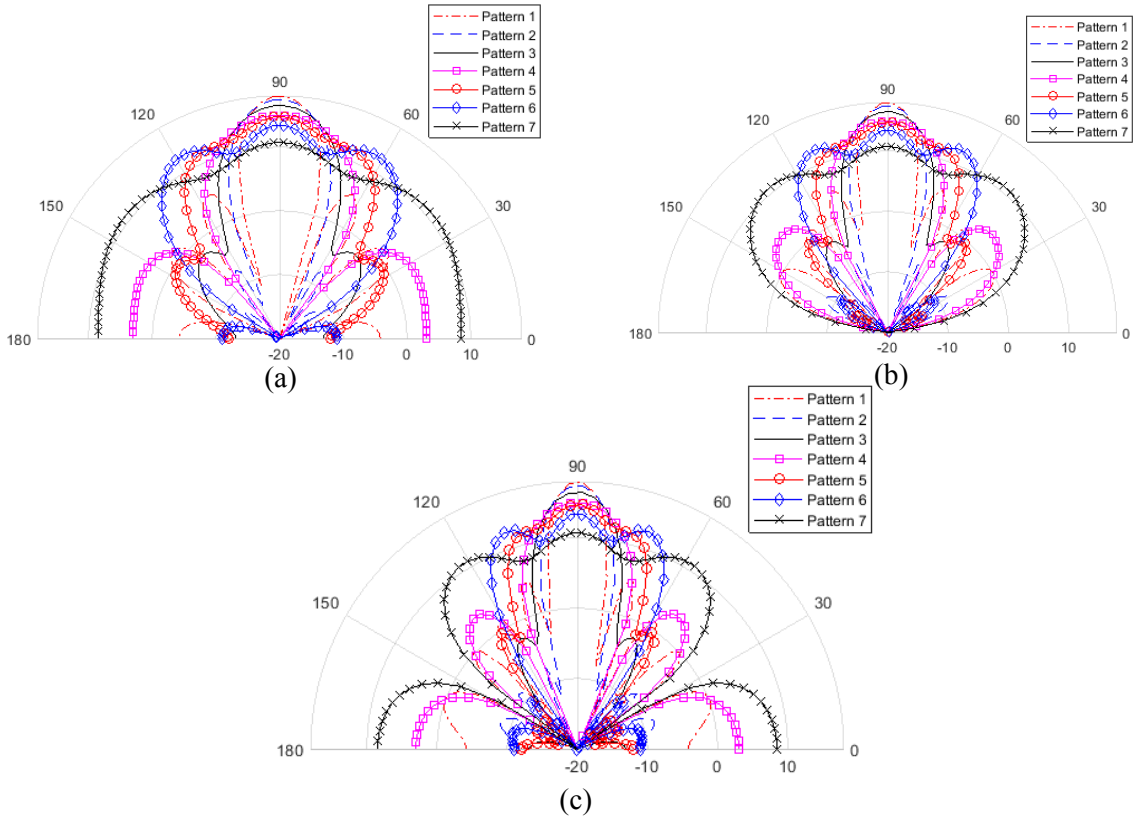


Fig. 7.15. Different array factors produced by different power ratios and phase shifts of the reconfigurable part feeding isotropic antennas (a)  $0.4 \lambda$  element spacing (b)  $0.5 \lambda$  element spacing (c)  $0.6 \lambda$  element spacing.

changed to 7 dB below the peak directivity (16.5 dB) when using pattern 3 configuration for the same antenna spacing, as in Fig. 7.16. Fig. 7.18 shows that the beam crossover level can reach 3.7 dB below the peak directivity (15 dB) if pattern 4 configuration (only 4 antennas) is used. Pattern 4 ensures an “almost” continuous coverage of the part of the upper halfspace ( $\theta_{elevation} > 30^\circ$ ) using the 4 inputs  $I_1$ ,  $I_2$ ,  $I_3$ , and  $I_4$ . Less number of inputs may be used to cover the same region as presented in Fig. 7.19; however with less directivity. Using pattern 5 configuration shows that inputs  $I_1$  or  $I_4$  of the Butler matrix may be used to cover the whole upper halfspace with  $10 \pm 1$  dB directivity and  $40^\circ$  overlap between the beams. This mode of operation may be used if the same signal is meant to be directed everywhere (without the need for high directivity) to achieve the minimum capacity requirements.

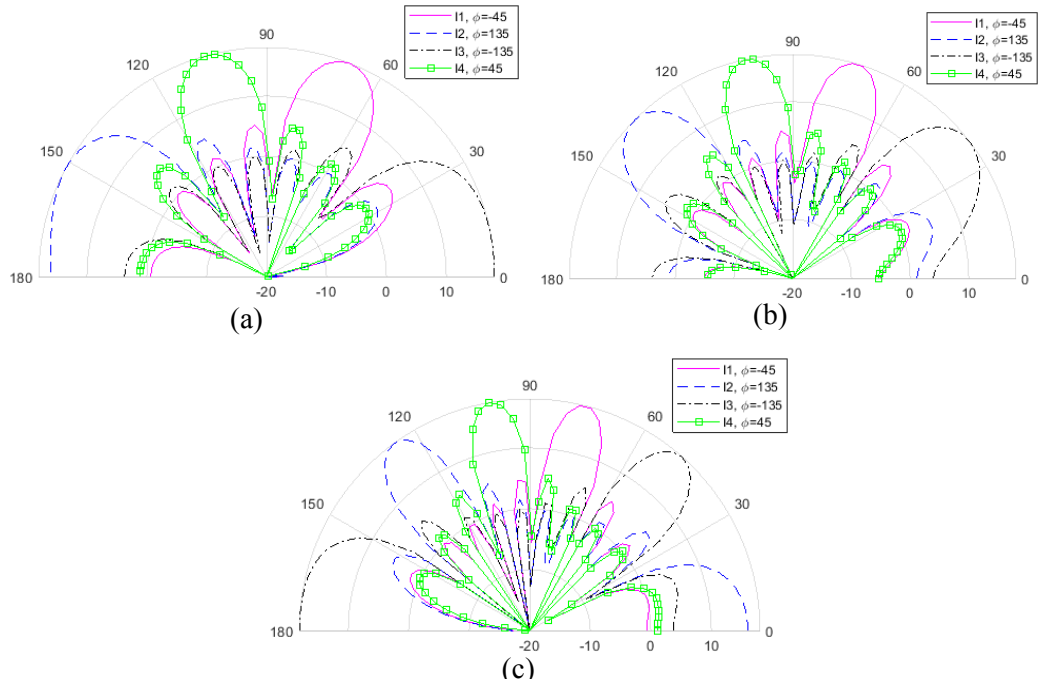


Fig. 7.16. Array factor of Butler matrix with equal power splitting and  $25^\circ$  progressive phase shift with different antenna spacing (maximum directivity 18 dB) (a)  $0.4 \lambda$  element spacing (b)  $0.5 \lambda$  element spacing (c)  $0.6 \lambda$  element spacing.

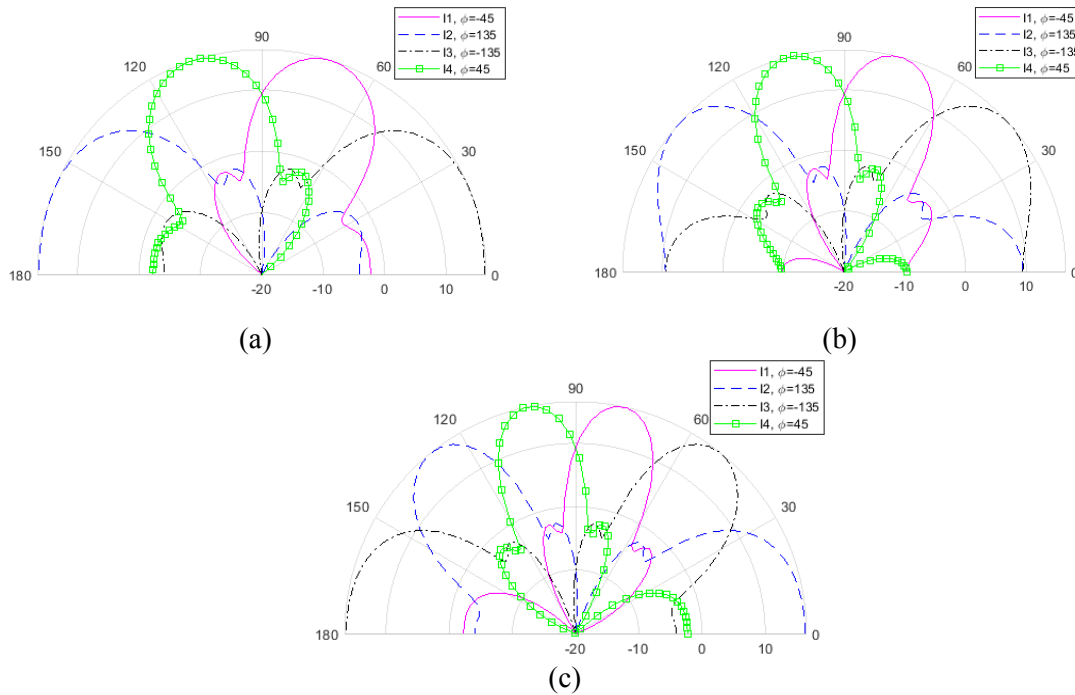


Fig. 7.17. Array factor of Butler matrix pattern 3 of Table 7.4 with different antenna spacing (maximum directivity 16.5 dB) (a)  $0.4 \lambda$  element spacing (b)  $0.5 \lambda$  element spacing (c)  $0.6 \lambda$  element spacing.

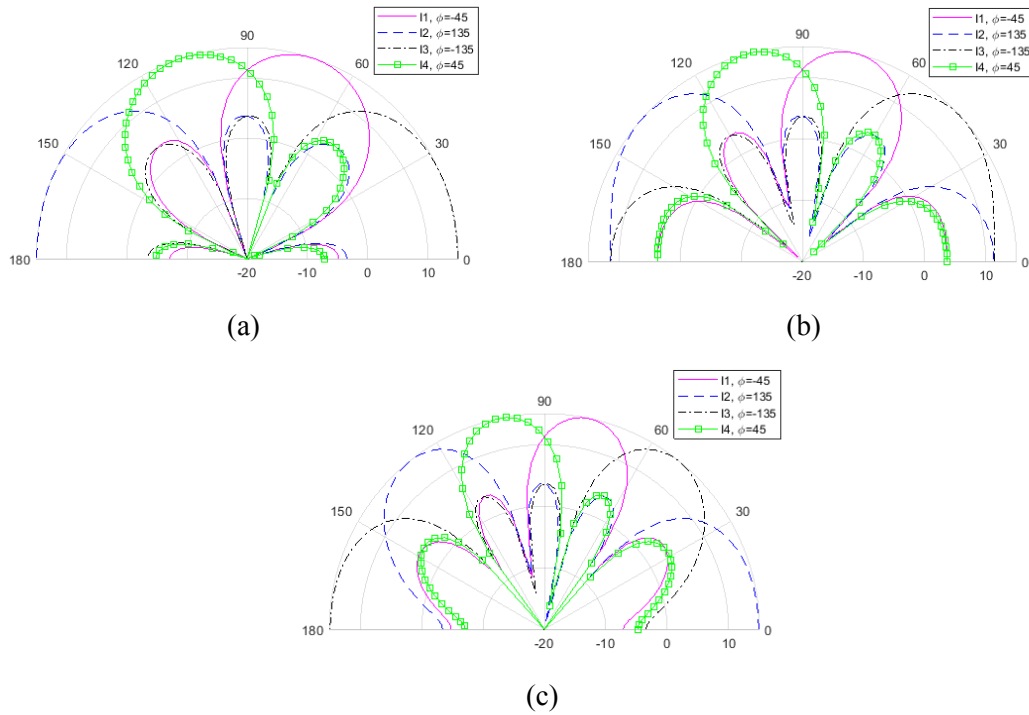


Fig. 7.18. Array factor of Butler matrix obtained using pattern 4 of Table 7.4 with different antenna spacing (maximum directivity 15 dB) (a)  $0.4 \lambda$  element spacing (b)  $0.5 \lambda$  element spacing (c)  $0.6 \lambda$  element spacing.

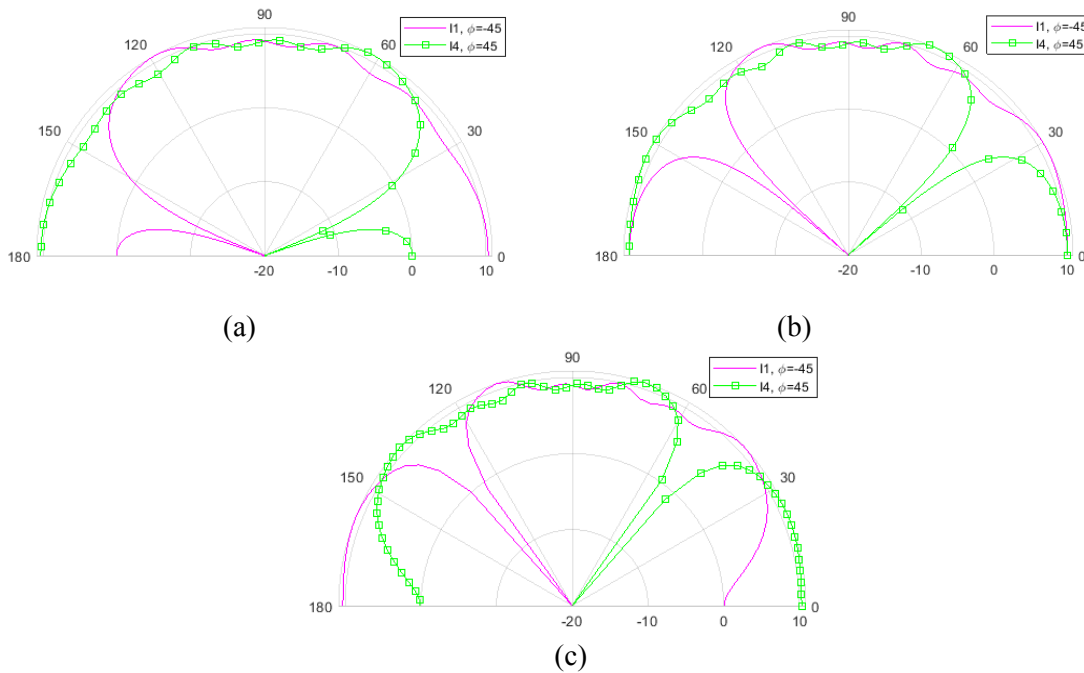


Fig. 7.19. Array factor of Butler matrix obtained using pattern 5 from Table 7.4 with different antenna spacing (maximum directivity 10 dB) (a)  $0.4 \lambda$  element spacing (b)  $0.5 \lambda$  element spacing (c)  $0.6 \lambda$  element spacing.

# Chapter 8

## Summary and Future Research Directions

In this thesis, several microwave components are designed in Ridge Gap waveguide technology to the end of designing a tunable Butler matrix, which can provide a variable beamwidth/gain, variable beam direction and a variable number of beams to cover a specific region in space. The variable number of beams may be used, in the mobile base station, to vary the provided capacity by the antenna system using the orthogonality of Butler matrix beams. The reconfigurable beamwidth can be used to reduce interference between orthogonal beams or provide soft handover between them. The tunability of this beamformer is essential in several fields like wireless communications, and radar applications, where either the motion of the whole system is required to achieve tunability or higher order Butler matrices, which are more complicated, are employed to increase the resolution. In what follows, we briefly summarize the contributions of this thesis.

### 8.1 Summary of Contributions

- ✓ In Chapter 3, two wideband inline and vertical coaxial to single ridge waveguide transitions are designed, fabricated and measured to feed ridge gap waveguide with 2.9:1 and 4:1 bandwidth ratios [72] and [73]. The ability to tune the bandwidth of the inline transition is shown to give the ability to cover different commercial bands (from Ku, K and part of Ka bands to part of Ku, K and Ka bands).
- ✓ In Chapter 4, a ridge waveguide power splitter of an arbitrary power split ratio is designed using asymmetric double ridge waveguide with a bandwidth ratio better than 3:1 [96]. The concept of asymmetric double ridge waveguide and the determination of its characteristic impedance and its zero field plane is introduced. This concept is useful in the design of single to double ridge waveguide transition. Three versions of the splitter are fabricated and measured with the help of the transition in [73], and a journal paper is submitted [138]. A novel ridge gap waveguide reconfigurable power splitter is designed to provide “arbitrary and real-time tunable” power splitting ratio on 40 % bandwidth representing the whole Ka-band [97]. The power handling capabilities, bandwidth, and sensitivity of this power splitter are discussed. A prototype is fabricated and measured using the transition in [73].

- ✓ In Chapter 5, an RGW quadrature hybrid working over a 40 % bandwidth with  $\pm 0.75$  dB amplitude error and better than 20 dB matching and isolation levels is designed, fabricated and measured with the help of the vertical transition in [73] and a calibration kit. This coupler may provide arbitrary coupling levels from 3 to 33 dB depending on the gap height, and number of slots. The coupler can also provide return loss and isolation better than 30 dB over 33% bandwidth by some parameter tuning. An analysis of this coupler has been introduced and the relevance between the analysis results and the simulation results have been shown. A journal paper has been submitted [139].
- ✓ In Chapter 6, a low error reconfigurable phase shifter is designed to work on 33% bandwidth in the Ka-band with phase shifting range up to  $200^\circ$  and phase error of  $\pm 15^\circ$ . An analysis of the phase shifter is presented.
- ✓ In Chapter 7, a  $135^\circ$  phase shifter is implemented in the RGW technology to work on 20 % bandwidth as a part of the basic Butler matrix and an assembly of the basic Butler matrix and the reconfigurable part is demonstrated. The results for several reconfigurability states are presented. The ability to obtain several reconfigurable beamwidth/gain radiation patterns is demonstrated within the constraints provided by equal-output basic Butler matrix.
- ✓ In Chapter 8, the full tunable Butler matrix is assembled to show its S-parameters. The control on the aperture of the reconfigurable part is shown by plotting several possible array factors of different beamwidth and maximum gains. The possibility of having variable crossbeam levels and maximum gain for the tunable Butler matrix is simulated. The possibility to have different number of beams covering the same region in space, which allows reconfigurable capacity, is presented.

## 8.2 Future Work

There are several research directions based on the work presented in this thesis:

- 1- Some efforts may be directed towards the miniaturization of the Butler matrix presented here without compromising the performance.
- 2- The same reconfigurable components introduced here may be organized in a different way to achieve a **reduced sidelobe level** for a  $4 \times 4$  Butler matrix. By feeding 2 signals at 2 inputs of  $4 \times 4$  Butler matrix (signals are identical except for a relative phase shift between them), a

cosine tapered beam of controllable side lobe level may be produced. In another arrangement, **an arbitrary progressive phase shift** for a  $4 \times 4$  Butler matrix is achievable.

- 3- Several components have been developed in this work. These components may be used towards better performance in different waveguide systems, other than the system presented here, like different types of beamforming networks or antenna arrays. The better performance could be measured by several factors including wider bandwidth and/or reconfigurable performance. Reconfigurable performance can be in terms of beamwidth, SLL and beam direction. It can also be used to switch between two different antenna systems or arrays for a reconfigurable performance. The reconfigurable power splitter may also be used towards graceful degradation of performance in case of component failure in antenna or microwave systems.
- 4- The possibilities of obtaining different array factors for antenna arrays may be exploited for desirable characteristics like interference cancellation by adaptive nulling and/or non-uniform sidelobe levels where we use both amplitude and phase distributions to obtain the desired radiation pattern.

## Appendix

### Characteristic Impedances of the ADR Waveguide

It is mentioned in [138] that any double ridge waveguide operating in the dominant mode has a zero tangential electric field horizontal plane (zero- $E_t$  plane). This plane's position can be determined using the fact that the cutoff frequency of the double ridge waveguide must equal the cutoff frequency of the corresponding single ridge waveguides. It is shown in Chapter 4, how to obtain the position of such a plane using exact and approximate methods for an asymmetric double ridge (ADR) waveguide, and it is shown that this plane exists in different ridge heights ratio. It is also shown in Chapter 4 how to design an arbitrary-ratio power splitter using this information. The splitting idea can be used in the determination of the characteristic impedance of the asymmetric double ridge waveguide using different definitions  $Z_{PV}$ ,  $Z_{PI}$ , and  $Z_{VI}$ . As mentioned in [11], the power voltage definition  $Z_{PV}$  for any waveguides originates from:

$$Z_{pv}(f) = \frac{\left(\int_0^d E \cdot dl\right) \left(\int_0^d E \cdot dl\right)^*}{2 P_{tot}}$$

where  $E$  is the vertical electric field along the vertical middle line of the guide,  $d$  is the height of the guide, where the field is non-zero, and  $P_{tot}$  is the total power carried by the guide. Now assume that the asymmetric double ridge waveguide in Fig. A.1 is divided into two single ridge guides using the dotted line representing the zero- $E_t$  plane. The impedance  $Z_{PV}$  of the asymmetric double ridge waveguide at infinite frequency may be calculated as:

$$Z_{PV}(\infty) = \frac{\left(\int_0^d E \cdot dl\right) \left(\int_0^d E \cdot dl\right)^*}{2 P_{tot}} = \frac{\left(\int_0^{d_A} E_A \cdot dl + \int_{d_A}^{d_B} E_B \cdot dl\right)^2}{2 (P_A + P_B)}$$

which may be reduced after algebraic manipulations into:

$$Z_{PV}(\infty) = Z_{PVA}(\infty) \frac{P_A}{P_{tot}} + Z_{PVB}(\infty) \frac{P_B}{P_{tot}} + \frac{2\sqrt{Z_{PVA}(\infty) Z_{PVB}(\infty)}}{\sqrt{\frac{P_A}{P_B}} + \sqrt{\frac{P_B}{P_A}}}$$

where the ratios  $\frac{P_A}{P_{tot}}$ , and  $\frac{P_B}{P_B}$  can be obtained if the guide dimensions, and the plane position are known using the equation:

$$P_{flow} = \frac{E^2 d_A \lambda_c}{2\pi\eta_o} \left\{ \left( \frac{4d_A}{\lambda_c} \right) \ln \left( \operatorname{cosec} \left( \frac{\pi d_A}{2b_A} \right) \right) (\cos \theta_2)^2 + 0.5 \theta_2 + 0.25 \sin(2\theta_2) + \left( \frac{d_A}{b_A} \right) \left( \frac{\cos \theta_2}{\sin \theta_1} \right)^2 [0.5 \theta_1 - 0.25 \sin(2\theta_1)] \right\}$$

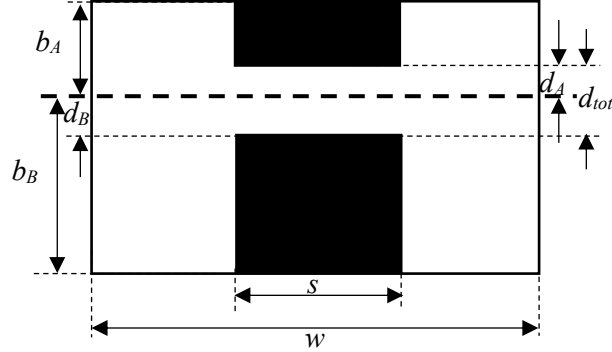


Fig. A.1. The asymmetric double ridge waveguide with all parameters shown.

Similarly, the other waveguide impedance definitions of the asymmetric double ridge waveguide ( $Z_{PI}$ , and  $Z_{VI}$ ) may be calculated using the corresponding single ridge impedances:

$$Z_{PI}(\infty) = \frac{2 P_{tot}}{(\oint H \cdot dl)(\oint H \cdot dl)^*}$$

where H is the tangential magnetic field to the top or the bottom wall. This field integral is the same for the single ridge guides A, and B, which make the impedance of the ADR guide equal to:

$$Z_{PI}(\infty) = Z_{PIA}(\infty) + Z_{PIB}(\infty).$$

A similar result is obtained in the Voltage-Current definition:

$$Z_{VI}(\infty) = Z_{VIA}(\infty) + Z_{VIB}(\infty)$$

An accuracy check on the obtained results is to design a 5<sup>th</sup> order Chebyshev transformer using ADR waveguide employing one of the definitions shown ( $Z_{PV}$  definition). The zero- $E_t$  plane position was obtained using the approximation:

$$\frac{P_A}{P_B} = \frac{d_A}{d_B} = \frac{b_A}{b_B}$$

The parameters of the Chebyshev transformer are shown in Table A.1, and the S-parameters of the Chebyshev transformer are shown in Fig. A.2. The transformer is designed for a maximum reflection of -30 dB. The return loss shown in Fig. A.2 is better than -23 dB. The difference between the two values is attributed to the field discontinuity, and the effect of approximation in obtaining the zero- $E_t$  plane position.

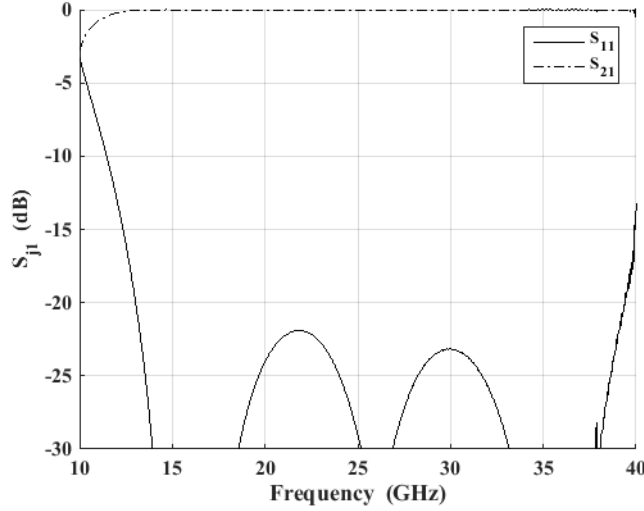


Fig. A.2. S-parameters for the 5-stage Chebyshev transformer designed using ADR waveguides based on the suggested formula. S-parameters are obtained using CST Microwave Studio.

Table A.1: Dimensions and impedances for different cross-sections of the ADR 5<sup>th</sup> order Chebyshev matching transformer.

Parameter	Start	1	2	3	4	5	End
$w$ (mm)	6.4	6.8	7.2	7.8	8.2	8.6	9
$b$ (mm)	3.5	3.65	3.65	3.75	4.05	4.05	4.2
$d$ (mm)	0.3	0.35	0.45	0.6	0.85	1.05	1.2
$s$ (mm)	3.5	3.5	3.7	3.4	3.6	3.6	3.5
$b_A/b$	0.53	0.55	0.625	0.6	0.66	0.73	0.75
$Z_{PV}$ ( $\Omega$ )	29.55	33.9	40.9	56.42	74	88.38	100
$Z_{PI}$ ( $\Omega$ )	27.94	31.9	37.8	51.17	65.32	76	84.7
$Z_{VI}$ ( $\Omega$ )	28.73	32.9	39.34	53.73	69.5	82	92.05

Another accuracy check is done using the formula that relates the different impedance definitions together [11] which is:

$$Z_{VI}^2 = Z_{PI} Z_{PV},$$

which is satisfied in all the Chebyshev transformer stages in Table A.1.

## **References:**

- [1] G. Siles, J. Riera and P. Garcia-de-Pino, "Atmospheric attenuation in wireless communication systems at millimeter and THz frequencies [Wireless corner]," *IEEE Antennas and Propagation Magazine*, vol. 57, no. 1, Feb. 2015.
- [2] W. Roh, J. Seol, J. Park, B. Lee, J. Lee, Y. Kim, J. Cho, K. Cheun and F. Aryanfar, "Millimeter-wave beamforming as an enabling technology for 5G cellular communications: theoretical feasibility and prototype results," *IEEE Communications Magazine*, vol. 52, no. 2, pp. 106-113, 2014.
- [3] M. Harris, "Tech giants race to build orbital internet," *IEEE Spectrum*, vol. 55, no. 6, pp. 10-11, 2018.
- [4] J. S. Blogh and L. Hanzo, "Intelligent Antenna Arrays and Beamforming," in *Third-Generation Systems and Intelligent Wireless Networking; Smart Antennas and Adaptive Beamforming*, Wiley-IEEE Press, 2002, p. 430.
- [5] M. Skolnik, *Radar Handbook*, 2nd edition, New York: McGraw-Hill, 1990.
- [6] D. Werner and R. Mittra, "Biological Beamforming," in *Frontier in Electromagnetics 1*, Wiley-IEEE Press, 2000, pp. 329-370.
- [7] R. Mailloux, *Phased Array Antenna Handbook*, London: Artech House, 2005.
- [8] A. Bhattacharyya, *Phased Array Antennas: Floquet Analysis, Synthesis, BFNs and Active Array Systems*, Hoboken, NJ: John Wiley & Sons, 2006.
- [9] K. Gupta, R. Garg, I. Bahl and P. Bhartia, *Microstrip Lines and Slotlines*, Norwood, MA: Artech House, Inc., 1996.
- [10] D. Pozar, *Microwave Engineering*, 4th edition, MA: John Wiley & Sons, Inc., 2012.
- [11] J. Helszajn, *Ridge Waveguides and Passive Microwave Components*, London, UK: IET Electromagnetic Waves Series 49, 2000.
- [12] P. Kildal, "Waveguides and transmission lines in gaps between parallel conducting surfaces". US Patent 2011/0181373 A1, 28 July 2011.
- [13] H. Raza, J. Yang, P. Kildal and E. Alos, "Resemblance between gap waveguides and hollow waveguides," *IET Microwaves, Antennas & Propagation*, vol. 7, no. 15, p. 1221 – 1227, 2013.
- [14] S. Shams and A. Kishk, "Printed texture with triangle flat pins for bandwidth enhancement of the ridge gap waveguide," *IEEE Transactions on Microwave Theory and Techniques*, vol. 65, no. 6, pp. 2093-2100, 2017.

- [15] P. Kildal and E. Rajo-Iglesias, "Numerical studies of bandwidth of parallel-plate cut-off realised by a bed of nails, corrugations and mushroom-type electromagnetic bandgap for use in gap waveguides," *IET Microwaves, Antennas & Propagation*, vol. 5, no. 3, pp. 282-289, 2011.
- [16] Q. Yang, J. Ban, J. Lian, L. Zhong and Y. Wu, "Compact SIW 3×3 Butler matrix for 5G mobile devices," in *International Applied Computational Electromagnetics Society Symposium (ACES)*, Suzhou, 2017.
- [17] M. Bialkowski, F. Tsai, Y. Su and K. Cheng, "Design of fully integrated 4x4 and 8x8 Butler matrices in microstrip/slot technology for ultra wideband smart antennas," in *2008 IEEE Antennas and Propagation Society International Symposium*, San Diego, 2008.
- [18] A. Alaqeel, S. Almorqi, O. Haraz, M. Ashraf, S. Alshebeili and A. Sebak, "Broadband 4 x 4 Butler matrix for K- and Ka- bands," in *IEEE International Symposium on Antennas and Propagation & USNC/URSI National Radio Science Meeting*, Vancouver, BC, 2015.
- [19] M. Nedil, T. Denidni and L. Talbi, "Novel Butler matrix using CPW multilayer technology," *IEEE Transactions on Microwave Theory and Techniques*, vol. 54, no. 1, pp. 499 - 507, Jan 2006.
- [20] H. Ren, J. Shao, B. Arigong, R. Zhou and H. Zhang, "A dual-band phased array antenna system based on Butler matrix network," in *2013 IEEE Antennas and Propagation Society International Symposium (APSURSI)*, Orlando, 2013.
- [21] Y. Zhang, W. Chio, W. Zhuang, W. Choi and K. Tam, "Size reduction of microstrip crossover using defected ground structure and its application in Butler matrix," in *2013 IEEE International Workshop on Electromagnetics, Applications and Student Innovation Competition*, Kowloon, China, 2013.
- [22] K. Wincza, S. Gruszczynski and K. Sachse, "Ultrabroadband 4 × 4 Butler matrix with the use of multisection coupled-line directional couplers and phase shifters," in *2011 Microwaves, Radar and Remote Sensing Symposium*, Kiev, Ukraine, 2011.
- [23] Y.-L. Li, Q. S. Liu, S. Sun and S. S. Gao, "A miniaturised Butler matrix based on patch hybrid couplers with cross slots," in *2013 IEEE Antennas and Propagation Society International Symposium (APSURSI)*, Orlando, 2013.
- [24] L. Baggen, M. Bottcher and M. Eube, "3D-Butler matrix topologies for phased arrays," in *2007 International Conference on Electromagnetics in Advanced Applications*, Torino, 2007.
- [25] J. Lian, Y. Ban, C. Xiao and Z. Yu, "Compact substrate-integrated 4 × 8 Butler matrix with sidelobe suppression for millimeter-wave multibeam application," *IEEE Antennas and Wireless Propagation Letters*, vol. 17, no. 5, pp. 928 - 932, 2018.
- [26] N. Ashraf, A. Kishk and A. Sebak, "AMC-Packaged Butler matrix for millimeter wave beamforming," in *2018 IEEE International Symposium on Antennas and Propagation & USNC/URSI National Radio Science Meeting*, Boston, 2018.

- [27] H. Chu and T. Ma, "An extended  $4 \times 4$  Butler matrix with enhanced beam controllability and widened spatial coverage," *IEEE Transactions on Microwave Theory and Techniques*, vol. 66, no. 3, pp. 1301-1311, 2018.
- [28] C. Chang, R. Li and T. Shih, "Design of a  $8 \times 8$  stripline Butler matrix with beam steering capability," in *2008 IEEE Antennas and Propagation Society International Symposium*, San Diego, CA, 2008.
- [29] F. Fakoukakis and F. Kyriacou, "On the design of a Butler matrix-based beamformer introducing low sidelobe level and enhanced beam-pointing accuracy," in *2011 IEEE-APS Topical Conference on Antennas and Propagation in Wireless Communications*, Torino, Italy, 2011.
- [30] T. Djerafi, J. Gauthier and K. Wu, "Variable coupler for Butler beam-forming matrix with low sidelobe level," *IET Microwaves, Antennas & Propagation*, vol. 6, no. 9, pp. 1034 - 1039, 2012.
- [31] K. Ding and A. Kishk, "Extension of Butler matrix number of beams based on reconfigurable couplers," *IEEE Transactions on Antennas and Propagation*, 2019.
- [32] C. Chang, R. Lee and T. Shih, "Design of a beam switching/steering Butler matrix for phased array system," *IEEE Transactions on Antennas and Propagation*, vol. 85, no. 2, pp. 367-374, 2010.
- [33] K. Tekkouk, J. Hirokawa, R. Sauleau, M. Ettorre, M. Sano and M. Ando, "Dual-layer ridged waveguide slot array fed by a Butler matrix with sidelobe control in the 60-GHz band," *IEEE Transactions on Antennas and Propagation*, vol. 63, no. 9, pp. 3857 - 3867, 2015.
- [34] B. Piovano, L. Accatino, F. Muoio, G. Caille and M. Mongiardo, "Cad and mechanical realization of planar, Ka-band,  $8 \times 8$  Butler matrices," in *32nd European Microwave Conference*, Milan, Italy, 2002.
- [35] A. Brazalez and E. Iglesias, "Design of a Butler matrix at 60GHz in inverted microstrip gap waveguide technology," in *2015 IEEE International Symposium on Antennas and Propagation & USNC/URSI National Radio Science Meeting*, Vancouver, BC, 2015.
- [36] F. Julian, G. Bernal and E. Rajo-Iglesias, "Design of a wide band Butler matrix in groove gap waveguide technology," in *2017 International Symposium on Antennas and Propagation (ISAP)*, Phuket, 2017.
- [37] S. Yamamoto, J. Hirokawa and M. Ando, "A single-layer hollow-waveguide 8-way Butler matrix," in *2005 IEEE Antennas and Propagation Society International Symposium*, Washington, 2005.
- [38] J. Hirokawa, M. Furukawa, K. Tsunekawa and N. Goto, "Double-layer structure of rectangular-waveguides for Butler matrix," in *2002 32nd European Microwave Conference*, Milan, 2002.
- [39] A. Dion and L. Ricardi, "A Variable-coverage satellite antenna system," *Proceedings of the IEEE*, vol. Vol. 59, no. 2, Feb. 1971.
- [40] R. Mizzoni, R. Ravanelli, P. Piovano, F. Alessandri and S. Badessi, "A Ku-band variable power divider for reconfigurable satellite antennas," in *8th international Conference on Antennas and Propagation*, Edinburgh, UK, March 1993.

- [41] M. Martin, M. Montesano, G. Crone and R. Garcia, "ASYRIO: Antenna SYstem Reconfiguration in Orbit," *IEEE Antennas and Propagation Magazine*, vol. 37, no. 3, pp. 7-14, 1995.
- [42] S. Peik, B. Jolley and R. Mansour, "High temperature superconductive Butler matrix beam former for satellite applications," in *1999 IEEE MTT-S International Microwave Symposium Digest (Cat. No. 99CH36282)*, Anaheim, 1999.
- [43] M. Alsharhawy and A. Kishk, "Design of waveguide to ridge gap waveguide transition using probe excitation," in *8th European Conference on Antennas and Propagation*, Hague, 2012.
- [44] A. Brazalez, A. Zaman and P. Kildal, "Investigation of a microstrip-to-ridge gap waveguide by EM coupling," in *Antennas and Propagation Society International Symposium*, Chicago, 2012.
- [45] A. Zaman, T. Vukusic, M. Alexanderson and P. Kildal, "Design of a simple transition from microstrip to ridge gap waveguide suited for MMIC and antenna integration," *IEEE Antennas and Wireless Propagation Letters*, vol. 12, pp. 1558-1561, 2013.
- [46] A. Brazalez, E. Iglesias and P. Kildal, "Investigations of transitions for use in inverted microstrip gap waveguide antenna arrays," in *European Conference on Antennas and Propagation*, Hague, 2014.
- [47] A. Brazalez, E. Iglesias, J. Roy, A. Vosoogh and P. Kildal, "Design and validation of microstrip gap waveguides and their transitions to rectangular waveguide for millimeter wave applications," *IEEE Transactions on Microwave Theory and Techniques*, vol. 63, no. 12, pp. 4035-4050, 2015.
- [48] H. Raza, J. Yang, P. Kildal and E. Alos, "Microstrip-ridge gap waveguide - study of losses, bends, and transition to WR-15," *IEEE Transactions on Microwave Theory and Techniques*, vol. 62, no. 9, pp. 1943-1952, 2014.
- [49] B. Molaei and A. Khalegi, "A novel wideband microstrip line to ridge gap waveguide transition using defected ground slot," *IEEE Microwave and Wireless Components Letters*, vol. 25, no. 2, pp. 91-93, 2015.
- [50] A. Brazalez, J. Flygare, J. Yang, V. Vassilev, M. Fscudero and P. Kildal, "Design of F-band transition from microstrip to ridge gap waveguide including MonteCarlo assembly tolerance analysis," *IEEE Transactions on Microwave Theory and Techniques*, vol. 64, no. 4, pp. 1245-1254, 2016.
- [51] A. Aljarosha, R. Maaskant, A. Zaman and P. Kildal, "MM-wave contactless connection for MMIC integration in Gap waveguides," in *IEEE International Symposium on Antennas and Propagation*, Puerto Rico, 2016.
- [52] S. Shams and A. Kishk, "Wideband coaxial to ridge gap waveguide transition," *IEEE Transactions on Microwave Theory and Techniques*, vol. 64, no. 12, pp. 4117 - 4125, 2016.
- [53] Y. Zhou, E. Li, G. Guo, T. Yang and L. Liu, "Design of millimeter wave wideband transition from double-ridge waveguide to coaxial line," *Journal of Infrared, Millimeter and THz waves*, vol. 32, no. 1, pp. 26-33, 2011.

- [54] S. Cohn, "Design of simple broad-band waveguide-to-coaxial-line junctions," *Proceedings of IRE*, vol. 35, no. 9, pp. 920-926, 1947.
- [55] A. Grimm and R. Schumacher, "Transition device". United States Patent 2982927, 2 May 1961.
- [56] J. Gaudio and T. Debski, "Broadband waveguide to coaxial line transition". United States Patent 3737812, 5 June 1973.
- [57] J. McCammon and G. Imokawa, "Coaxial line to double ridge waveguide transition". United States Patent 4144506, 13 March 1979.
- [58] R. Boni, F. Caspers, A. Gallo, G. Gemme and R. Parodi, "A broadband waveguide to coaxial transition for high order mode damping in particle accelerator RF cavities," *Particle Accelerators*, vol. 45, pp. 195-208, 1994.
- [59] T. Rizawa and R. Pendleton, "Broadband-coax waveguide transitions," *Proceeding of Particle Accelerator Conference*, vol. 3, pp. 1824-1826, 1995.
- [60] Y. Tikhov, Y. Kim and J. Kim, "An over octave compact transition from double-ridge waveguide to coaxial line for phased array feed," in *32nd European Microwave Conference*, Milan, 2002.
- [61] Z. Liu, J. Cruz, C. Wang and K. Zaki, "An extremely wideband ridge waveguide filter," in *IEEE MTT-S International Microwave Symposium*, 2004.
- [62] S. Martynyuk, P. Stepanenko and V. Kamaukh, "Wideband transition from coaxial to double ridged waveguide," in *5th International Conference on Antenna Theory and Techniques*, Kyiv, 2005.
- [63] Z. Hradecky, M. Mazanek and T. Korinek, "Double-ridged structures mode study for broadband antennas design," in *1st European Conference Antennas and Propagation*, Nice, 2006.
- [64] M. Kujalowicz, W. Zieniutycz and M. Mazur, "Double ridged horn antenna with sinusoidal ridge profile," in *International Conference on Microwave & Radar and Wireless Communication*, Krakow, 2006.
- [65] A. Mallahzadeh and A. Imani, "Double-ridged antenna for wideband applications," *Progress in Electromagnetic Research*, vol. 91, pp. 273-285, 2009.
- [66] N. Xing, L. En, G. Feng and W. Yi, "Simulation and design of 18-40 GHz ridge waveguide to coaxial transition," in *IEEE International Conference on Microwave Technology and Computational Electromagnetics (ICMTCE)*, 2011.
- [67] Q. Li, Q. Wang, G. Wu and Y. Tan, "A novel highpass filter using ridge waveguide," in *International Workshop on Microwave and Millimeter Wave Circuits and System Technology*, Chengdu, 2012.
- [68] Y. Du, K. Zhao and Z. Zeng, "Design and simulation of an UWB single-ridge waveguide band-pass filter," in *IEEE International Conference on Applied Superconductor and Electromagnetic Devices*, Beijing, 2013.

- [69] V. Rudakov, V. Sledkov, A. Mayorov and M. Manuilov, "Wideband ultra-compact coaxial-to-rectangular waveguide and coaxial-to-double ridged waveguide transitions," in *23rd International Crimean Conf. on Microwave & Telecommunication Technology*, Sevastopol, 2013.
- [70] M. Morgan and T. Boyd, "A 10-100 GHz double-ridged horn antenna and coax launcher," *IEEE Transactions on Antennas and Propagation*, vol. 63, no. 8, pp. 3417-3422, 2015.
- [71] A. Darvazehban, O. Manoochehri, M. Salari, P. Dekhoda and A. Tavakoli, "Ultra-wideband scanning antenna array with Rotman lens," *IEEE Transactions on Microwave Theory and Techniques*, vol. 65, no. 9, pp. 3435-3442, 2017.
- [72] M. Nasr and A. Kishk, "Wideband inline coaxial to ridge waveguide transition with tuning capability for ridge gap waveguide," *IEEE Transactions on Microwave Theory and Techniques*, vol. 66, no. 6, pp. 2757 - 2766, 2018.
- [73] M. Nasr and A. Kishk, "Vertical coaxial-to-ridge waveguide transitions for ridge and ridge gap waveguides with 4:1 bandwidth," *IEEE Transactions on Microwave Theory and Techniques*, vol. 67, no. 1, pp. 86-93, 15 October 2019.
- [74] R. Kazemi and A. Fathy, "Design of a wideband eight-way single ridge substrate integrated waveguide power divider," *IET Microwaves, Antennas and Propagation*, vol. 9, no. 7, pp. 648-656, 2015.
- [75] K. Song and Y. Fan, "Broadband traveling-wave power divider based on substrate integrated rectangular waveguide," *Electronics Letters*, vol. 45, no. 12, pp. 631-632, 2009.
- [76] Y. Ning, J. Sun, J. Liu and W. Jiang, "A new spatial power combiner based on 32-way ridged waveguides," in *XXXIth URSI General Assembly and Scientific Symposium*, Beijing, 2014.
- [77] M. Rocher, A. Nogueira and I. Heruzo, "New feeding network topologies for high-gain single-layer slot array antennas using gap waveguide concept," in *11th Eur. Conf. on Antennas and Propag. (EUCAP)*, Paris, 2017.
- [78] T. Sehm, A. Lebto and A. Raisanen, "A high-gain 58-GHz box-horn array antenna with suppressed grating lobes," *IEEE Transactions on Antennas and Propagation*, vol. 47, no. 7, pp. 1125-1130, 1999.
- [79] C. Buoli, S. Fusaroli, V. Gadaleta, F. Morgia and T. Turillo, "Microstrip to waveguide 3dB power splitter/combiner on FR4 PCB up to 50 GHz," in *2005 European Microwave Conference*, Paris, 2005.
- [80] G. Siso, J. Bonache and F. Martin, "Dual-band Y-junction power dividers implemented through artificial lines based on complementary resonators," in *2008 IEEE MTT-S International Microwave Symposium Digest*, Atlanta, 2008.
- [81] N. Drobotun, D. Yanchuk and E. Khoroshilov, "Compact planar ultra-wideband power dividers with frequency range up to 67 GHz for multichannel receivers," in *46th European Microwave Conference*, London, 2016.

- [82] K. Srisathit, P. Jadhav and W. Surakampontrorn, "Miniature wilkinson divider and hybrid, coupler with harmonic suppression, using T-shaped transmission line," in *2007 Asia-Pacific Microwave Conference*, Bangkok, 2007.
- [83] J. Zhou, K. Morris and M. Lancaster, "General design of multiway multisection power dividers by interconnecting two-way dividers," *IEEE Transactions on Microwave Theory and Techniques*, vol. 55, no. 10, pp. 2208-2215, 2007.
- [84] R. Beyers and D. De Villiers, "Compact conical-line power combiner design using circuit models," *IEEE Transactions on Microwave Theory and Techniques*, vol. 62, no. 11, pp. 2650-2658, 2014.
- [85] P. Chi, Y. Chi and T. Yang, "A reconfigurable in-phase/out-of-phase and power-dividing ratio power divider," in *2017 IEEE Asia Pacific Microwave Conference (APMC)*, Kuala Lumpur, 2017.
- [86] Y. Peng, H. Zhang and Y. Hu, "Design of an orthogonal power divider with reconfigurable power division ratio," in *2016 IEEE International Conference on Microwave and Millimeter Wave Technology (ICMMT)*, Beijing, 2016.
- [87] H. Fan, X. Liang, J. Geng, R. Jin and X. Zhou, "Reconfigurable unequal power divider with a high dividing ratio," *IEEE Microwave and Wireless Components Letters*, vol. 25, no. 8, pp. 514-516, 2015.
- [88] H. Tae, K. Oh, H. Lee, W. Son and J. Yu, "Reconfigurable 1x4 Power Divider With Switched Impedance Matching Circuits," *IEEE Wireless and Components Letter*, vol. 22, no. 2, pp. 64-66, 2012.
- [89] D. Jian, Y. Jun and D. Xidong, "A novel reconfigurable three-way power divider constructed on unitary plane," in *2015 12th IEEE International Conference on Electronic Measurement & Instruments (ICEMI)*, Qingdao, 2015.
- [90] H. Hammad and Y. Antar, "Microstrip quad mode reconfigurable power divider," in *2014 44th European Microwave Conference*, Rome, 2014.
- [91] H. Chen, W. Che, Y. Cao, W. Feng and K. Sarabandi, "Function-Reconfigurable Between SPDT Switch and Power Divider Based on Switchable HMSIW Unit," *IEEE Microwave and Wireless Components Letters*, vol. 27, no. 3, pp. 275-277, 2017.
- [92] C. Trammel and R. Kich, "Ferrite Variable Power Divider". US Patent 2004/6822533, 23 November 2004.
- [93] E. Matthews, "Variable Power Dividers in Satellite Systems," in *1976 IEEE-MTT-S International Microwave Symposium*, Cherry Hill, 1976.
- [94] U. Shah, "A 500–750 GHz RF MEMS Waveguide Switch," *IEEE Transactions on Terahertz Science and Technology*, vol. 7, no. 3, pp. 326-334, 2017.
- [95] J. Ruiz-Cruz, M. Fahmi and R. Mansour, "Generalized Multiport Waveguide Switches Based on Multiple Short-Circuit Loads in Power-Divider Junctions," *IEEE Transactions on Microwave Theory and Techniques*, vol. 59, no. 12, pp. 3347-3355, 2011.

- [96] M. Nasr and A. Kishk, "Design of an UWB power splitter of arbitrary split ratio using asymmetrical double ridge waveguide," in *32nd General Assembly and Scientific Symposium of the International Union of Radio Science (URSI GASS)*, Montreal, QC, 2017.
- [97] M. Nasr and A. Kishk, "Reconfigurable power splitter using Ridge Gap Waveguide Technology," in *2018 18th International Symposium on Antenna Technology and Applied Electromagnetics (ANTEM)*, Waterloo, 2018.
- [98] H. Bethe, "Theory of Diffraction by Small Holes," *Physics Review*, vol. 66, no. 7,8, 1944.
- [99] B. Eicher and C. Staeger, "High Performance Ridge Waveguide Directional Coupler," in *5th European Microwave Conference*, Hamburg, 1975.
- [100] O. Manoochehri, A. Darvazehban and D. Erricolo, "UWB double-ridge waveguide coupler with low loss," *Microwave and Optical Technology Letters*, vol. 59, pp. 1787-1791, 2017.
- [101] Y. Wqang and Y. Fu, "A broadband waveguide power splitter and combiner using in spatial power combining amplifier," in *2011 International Conference on Electronics, Communications and Control (ICECC)*, Ningbo, 2011.
- [102] C. Ma and J. Wang, "Design of wide band directional coupler by ridged rectangular waveguide for large power capability," in *2015 IEEE 6th International Symposium on Microwave, Antenna, Propagation, and EMC Technologies (MAPE)*, Shanghai, 2015.
- [103] M. Fahmi, J. Ruiz-Cruz and K. Zaki, "E and H-plane wide-band ridge waveguide couplers," *International Journal of RF and Microwave Computer-Aided Engineering*, vol. 18, pp. 348-358, 2008.
- [104] J. Ruiz-Cruz, Y. Zhang, K. Zaki, A. Piloto and J. Rebolgar, "Ridge waveguide branch-line directional couplers for wideband applications and LTCC technology," in *IEEE MTT-S International Microwave Symposium Digest*, Long Beach, CA, 2005.
- [105] B. Kou, E. Li and Z. Zhang, "A Ku Band High Power Rectangular Waveguide Directional Coupler's Design," in *2012 Spring Congress on Engineering and Technology*, Xian, 2012.
- [106] D. Sun and J. Xu, "Rectangular waveguide coupler with adjustable coupling coefficient using gap waveguide technology," *Electronics Letters*, vol. 53, no. 3, pp. 167-169, 2017.
- [107] S. Shams and A. Kishk, "Design of 3-dB Hybrid Coupler Based on RGW Technology," *IEEE Transactions on Microwave Theory and Techniques*, vol. 65, no. 10, pp. 3849-3855, 2017.
- [108] B. Ahmadi and A. Banai, "A power divider/combiner realized by ridge gap waveguide technology for millimeter wave applications," in *2016 Fourth International Conference on Millimeter-Wave and Terahertz Technologies (MMWaTT)*, Tehran, 2016.
- [109] D. Zarifi and A. Shater, "Design of a 3-dB directional coupler based on groove gap waveguide technology," *Microwave Optical Technology Letters*, vol. 59, p. 1597-1600, 2017.

- [110] H. Raza and J. Yang, "A low loss rat race balun in gap waveguide technology," in *5th European Conference on Antennas and Propagation (EUCAP)*, Rome, 2011.
- [111] M. Farahani, M. Akbari, M. Nedil, T. Denidni and A. Sebak, "A Novel Low-Loss Millimeter-Wave 3-dB 90° Ridge-Gap Coupler Using Large Aperture Progressive Phase Compensation," *IEEE Access*, vol. 5, pp. 9610-9618, 2017.
- [112] J. Riblet, "The Short-slot Junction," *Proceedings of the IRE*, vol. 40, no. 2, pp. 180-184, 1952.
- [113] U. Rosenberg and W. Speldrich, "A new waveguide directional coupler/hybrid type-favorably suited for millimeter wave application," *IEEE MTT-S International Microwave Symposium Digest (Cat. No. 00CH37017)*, vol. 3, pp. 1311-1314, 2000.
- [114] E. Hadge, "Compact Top-Wall Hybrid Junction," *Transactions of the iRE Professional Group on Microwave Theory and Techniques*, vol. 1, no. 1, pp. 29-30, 1953.
- [115] R. Beyer and R. U., "Compact top-wall hybrid coupler design for extreme broad bandwidth applications," in *IEEE MTT-S International Microwave Symposium Digest*, Long Beach, CA, 2005.
- [116] Q. Xiaoyun, W. Diancheng, Y. Naiheng and S. Jiangda, "A new design of waveguide broad-wall couplers," in *International Conference on Microwave and Millimeter Wave Technology*, Beijing, China, 2002.
- [117] Y. Li, Z. Zhang, Z. Feng and M. Iskander, "A Beam-Steerable CPW-CTS antenna array using Reconfigurable metamaterial-based Phase Shifters for Cognitive Radio Applications," in *XXXIth URSI General Assembly and Scientific Symposium*, Beijing, 2014.
- [118] S. Sheikh, "Analog/Digital Ferrite Phase Shifter For Phased Array Antennas," *IEEE Antennas and Wireless Propagation Letters*, vol. 9, pp. 319-321, 2010.
- [119] N. Somjit, G. Stemme and J. Oberhammer, "Novel Concept of Microwave MEMS Reconfigurable 7 x 45 Multi-Stage Dielectric Block Phase Shifter," in *IEEE 22nd International Conference on Micro-ElectroMechanical Systems*, Sorrento, 2009.
- [120] S. Mueller, F. Goelden, P. Scheele, M. Wittek, C. Hock and R. Jakoby, "Passive Phase Shifter for W-Band Applications using Liquid Crystals," in *2006 European Microwave Conference*, Manchester, 2006.
- [121] D. Chicherin, S. Dudorov, D. Lioubtchenko, V. Ovchinnikov and A. Raisanen, "Millimetre Wave Phase Shifters Based on a Metal Waveguide with a MEMS-Based High-Impedance Surface," in *2006 European Microwave Conference*, Manchester, 2006.
- [122] E. Sbarra, L. Marcaccioli, R. Gatti and R. Sorrentino, "Ku-band analogue phase shifter in SIW technology," in *2009 European Microwave Conference*, Rome, 2009.
- [123] M. Stoneback, C. Wolthausen and Y. Kuga, "A steerable 60 GHz array antenna using a reconfigurable dielectric phase shifter," in *2010 IEEE Antennas and Propagation Society International Symposium*, Toronto, 2010.

- [124] K. Yokokawa et al., "Study on reconfigurable corrugated waveguide using moveable shorting plate," in *2017 IEEE Conference on Antenna Measurements & Applications (CAMA)*, Tsukuba, 2017.
- [125] Q. Zhang, C. Yuan and L. Liu, "Studies on mechanical tunable waveguide phase shifters for phased-array antenna applications," in *2016 IEEE International Symposium on Phased Array Systems and Technology (PAST)*, Waltham, 2016.
- [126] L. Polo-López, J. Masa-Campos and J. Ruiz-Cruz, "Design of a reconfigurable rectangular waveguide phase shifter with metallic posts," in *2017 47th European Microwave Conference (EuMC)*, Nuremberg, 2017.
- [127] J. Gaudio and T. Debski, "Broadband Waveguide to Coaxial Line Transition". US Patent 3737812, 5 June 1973.
- [128] Y. Zhou, E. Li, T. Yang and L. Liu, "Design of Millimeter Wave Wideband Transition from Double-ridge Waveguide to Coaxial Line," *Journal of IR, Millimeter and THZ Waves*, vol. 32, no. 1, pp. 26-33, 2011.
- [129] J. Montgomery, "On the Complete Eigenvalue Solution of Ridged Waveguide," *IEEE Transactions on Microwave Theory and Techniques*, vol. 19, no. 6, pp. 547-555, 1971.
- [130] J. D. and T. Rao, "Design of double-ridged rectangular waveguide of arbitrary aspect ratio and ridge height," *IEE Proceedings - Microwaves, Antennas and Propagation*, vol. 147, no. 1, pp. 31-34, 2000.
- [131] S. Hopfer, "The Design of Ridged Waveguides," *IRE Transactions on Microwave Theory and Techniques*, vol. 3, no. 5, pp. 20-29, 1955.
- [132] P. J., "The Cutoff Wavelength of the TE<sub>10</sub> Mode in Ridged Rectangular Waveguide of Any Aspect Ratio," *IEEE Transactions on Microwave Theory and Techniques*, vol. 14, no. 4, pp. 175-183, 1966.
- [133] W. Hoefler and B. M., "Closed-Form Expressions for the Parameters of Finned and Ridged Waveguides," *IEEE Transactions on Microwave Theory and Techniques*, vol. 30, no. 12, pp. 2190-2194, 1982.
- [134] M. Nasr, "Design of Tunable Beamforming Networks using Ridge Gap Waveguide, PhD Research Proposal in Concordia University," Montreal, QC, 2018.
- [135] J. Gere, *Mechanics of Materials*, Thomson Learning Inc., 2004.
- [136] D. Marcuvitz, *Waveguide Handbook*, MA, USA: John Wiley & Sons Inc., 2012.
- [137] S. Gruszczynski and K. Wincza, "Reduced sidelobe four-beam N-element antenna arrays fed by NxN Butler matrices," *IEEE Antennas and Wireless Propagation Letters*, vol. 5, pp. 430-434, 2006.
- [138] M. Nasr and A. Kishk, "UWB E-plane Power splitter with Arbitrary Division Ratio in Ridge Waveguides," *IEEE Transactions on Microwave Theory and Techniques*, in review.
- [139] M. Nasr and A. Kishk, "Broadband Ridge Gap Waveguide Tight and Loose Hybrid Couplers," *IEEE Transactions on Microwave Theory and Techniques*, in review.

- [140] M. Bialkowski, F. Tsai, Y. C. Su and K. H. Cheng, "Design of fully integrated 4x4 and 8x8 Butler matrices in microstrip/slot technology for ultrawideband smart antennas," in *IEEE Antennas and Propagation International Symposium*, San Diego, CA, 2008.
- [141] J. Remez and R. Carmon, "Compact Designs of Waveguide Butler Matrices," *IEEE Antennas and Wireless Propagation Letters*, pp. 27-31, 6 March 2006.
- [142] C. Balanis, *Modern Antenna Handbook*, John Wiley & Sons Inc., 2008.
- [143] E. Alos, M. Baquero, P. Kildal, A. Nogueira, I. Iglesias and J. Herranz, "Design of microwave circuits using ridge gap waveguide technology," in *2010 IEEE MTT-S International Microwave Symposium*, Anaheim, CA, 2010.